Folding behavior of elastic origami metamaterials

Fernando Agustín Iñiguez Rábago

Ph.D. Thesis, Eindhoven University of Technology, September 2021

Folding behavior of elastic origami metamaterials
Fernando Agustín Iñiguez Rábago

Cover image: **Tessellated Stability** I arranged identifying data for a selection of stable states of all the different origami structures studied in this thesis and plotted them individually. Each plot was then tessellated to form the cover. The colored plots come from the initial states of the structures with zero energy. The tessellated plots show the symmetries that these states have and represent the metamaterial aspect of the origami structures.

ISBN: 978-90-386-5302-0
A catalogue record is available from the Eindhoven University of Technology Library.
A digital version of this thesis can be downloaded from
http://amolf.nl and https://research.tue.nl/

The work described in this thesis was performed at AMOLF, Science Park 104, 1098 XG Amsterdam, The Netherlands.

This work is part of the Dutch Research Council (NWO) and it was part of the research program Innovational Research Incentives Scheme Veni from NWO with project number 15868 (NWO).

Folding behavior of elastic origami metamaterials

PROEFSCHRIFT

ter verkrijging van de graad van doctor aan de Technische Universiteit Eindhoven, op gezag van de rector magnificus prof.dr.ir. F.P.T. Baaijens, voor een commissie aangewezen door het College voor Promoties, in het openbaar te verdedigen op dinsdag 28 september 2021 om 16:00 uur

door

Fernando Agustín Iñiguez Rábago

geboren te Mexico Staat, Mexico.

Dit proefschrift is goedgekeurd door de promotoren en de samenstelling van de promotiecommissie is als volgt:

voorzitter	prof.dr. L.P.H. de Goey
1^{e} promotor	dr.ir. J.T.B. Overvelde
2^{e} promotor	prof.dr. H. Nijmeijer
Promotiecommissieleden:	dr.ir. J.T.B. Overvelde
	prof.dr. H. Nijmeijer
	prof.dr. B. Speckmann
	prof.dr. M. van Hecke (Universiteit Leiden)
	prof.dr. G.H. Paulino (Georgia Institute of Technology)

Het onderzoek of ontwerp dat in dit thesis wordt beschreven is uitgevoerd in overeenstemming met de TU/e Gedragscode Wetenschapsbeoefening.

Science knows no country, because knowledge belongs to humanity,
and is the torch which illuminates the world.

Louis Pasteur

Contents

1

Introduction

The butterflies in Rosei's dream would be origami.

Ihara Saikaku, 1680

Based on: McClintock*, H.D., Doshi*, N., Iniguez-Rabago*, A., Weaver, J.C., Jayaram, K., Wood, R.J., Overvelde, J.T.B., *A fabrication strategy for re-configurable materials at the millimeter-scale.* Adv. Funct. Mater. (* contributed equally) (In Press)

1

1.1. From rigid to elastic origami

The word origami comes from the Japanese *ori* (folding) and *kami* (paper) and is a technique that is used to transform a flat sheet of paper into any shape by folding it repeatedly. In Japan, origami was originally used in religious ceremonies as decoration [1]. In Germany, the inventor of kindergartens used origami to develop consciousness of forms and figures in children [2]. Recently, it has gained popularity in many fields. For example, in architecture [3, 4], origami is used as a way to fold gigantic umbrellas [5] or in responsive facades to control the temperature of buildings [6]. In engineering [7–9], it is used as inspiration to create unfolding mechanism for robots [10] or even as a microsurgery system [11]. In biology [12, 13], origami is used to understand the folding mechanisms of wings [14, 15] or as a structure to sense DNA [16].

Traditionally, scientists have described origami using a rigid model. In this model, origami deforms only at the folds (hinges), whereas the flat areas of paper (faces) are completely rigid. Due to its simplicity this model has been widely used by scientists, for example, to understand how to fold a map [17] or a paper bag [18]. Nonetheless, this model has some limitations, for example, while it describes most origami at the centimeter-scale very well, it fails to describe accurately the behavior of smaller origami [19]. This is because the model assumes that deformations take place only at the hinges, which is not always met in real life.

Currently, scientists increasingly study origami using an elastic model [20–23]. Elastic origami allows for the deformation of not only the hinges but also the faces, as a result, it allows new behaviors that are not possible with the rigid model, including folding origami with different curvatures [24] and multistability [14, 25]. In fact, elastic origami can reach additional deformations through new folding pathways [26–29]. These new behaviors are important since they can be used in new generations of origami-inspired structures and devices.

Nevertheless, the flexibility of elastic origami comes at a cost. Since origami behavior cannot longer be described by just the hinges, but also by the deformation of the faces, it is nearly impossible to describe it analytically. This results in three problems that I will address in this thesis. First, the additional deformation of the faces adds many parameters to the origami model that complicates the full scan of the origami behavior. *Is it possible to simplify the model in order to study complex origami designs based on real life experiments?* Second, the folding behavior of elastic origami is highly nonlinear, making it difficult to map all the possible folding behaviors. *Can we find a way to systematically characterize the deformation space in the elastic origami model?* Third, any force gets dissipated by the elasticity preventing global uniform deformation. *How can we obtain well-defined folding behavior in the elastic origami model?* I use origami-inspired metamaterials as case studies to resolve these questions, nevertheless the same approach can be used for any other origami pattern. These solutions shed light on the complex behavior of origami and gives specific guidelines to control it.

1.2. Overview of origami studies

In this section, I introduce some basic concepts and the research that has been done on and around origami. First, I introduce concepts used to describe origami behavior from the mathematical point of view, such as the way the hinges are described, interact and move together. Then, I show specific origami designs which have some interesting behavior, and show how elastic origami opens the door to describe undiscovered folding behaviors of origami. This builds the foundation to the search of new folding behaviors in the elastic origami model. Last, I move away from traditional origami patterns to introduce origami-inspired metamaterials. I describe some properties of these origami-inspired metamaterials, and how they are affected by elasticity. This helps us to better understand the effect of forces on elastic origami and how it affects its global folding behavior.

1.2.1. Basic concepts of origami behavior

First I introduce the concept of a vertex which provides the basis for origami patterns. I invite the reader to undertake the following steps with me to understand this and other origami concepts. Let us start with a flat sheet of paper in which we create a hinge by folding it (Fig. 1.1a). We then unfold it and lay it flat again. The hinge can now be in two positions: folded towards the back (mountain) or the front (valley) as seen in Fig. 1.1b. Notice that by flipping the paper we can convert the mountain into a valley and vice versa. We then fold the paper along the first fold (Fig. 1.1a), and fold it again, in order to have two folds (Fig. 1.1c). We then unfold the paper. The point where the hinges cross is called a vertex and divides the hinges into two, so we are left with 4 hinges (Fig. 1.1d). This particular vertex is called a 4-vertex since four hinges converge to it. Any origami pattern is composed of multiple vertices which are the points where the interaction between faces and hinges takes place [30].

Next, I show some general properties of the vertex folding behavior. The 4-vertex that we just created is a flat-foldable origami pattern, meaning that the pattern can be folded to a flat configuration as seen in Fig. 1.1c where all the faces are flat. It is also rigid-foldable which means that it can be folded following the rigid origami model. Flat- and rigid-foldability are just some examples of origami pattern properties. Flat-foldability is easy to obtain since it follows a couple of theorems [31, 32], however determining the rigid-foldability of a general pattern is an NP-hard problem [33] that can be only solved for simple patterns [34, 35]. As a result, most origami studies are on specific origami patterns, nevertheless the methods used and developed for a particular pattern can be extended and used for many other patterns.

The last concept to introduce involves the action of origami folding. Let us again use this flat-foldable 4-vertex that we just folded. It has 4 hinges, each defined by the angle θ between the adjacent faces (Fig. 1.1e). Each of these angles is a variable that describes the deformation of the vertex. The four angles interact at the vertex. This interaction can be described by a set of equations, which specify the constraints on the movement of the hinges derived from their interconnection through the rigid faces. There are, however, more angles than constraints in this particular case, allowing this 4-vertex to de-

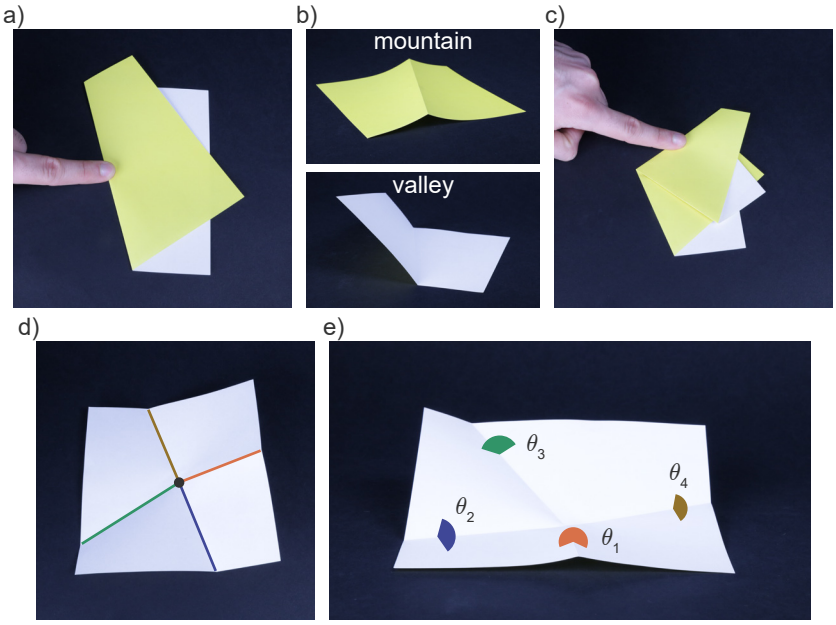

Figure 1.1 | a) Folding a sheet of paper to create one hinge. b) Hinges can be of two types, mountain or valley. c) Folding the sheet of paper again to create a vertex. d) The created vertex has 4 hinges, shown in different colors. e) The deformation of the vertex can be described with the 4 angles that represent each hinge.

form. This movement involves more than just one hinge and is called a branch. This flat-foldable 4-vertex has two branches with the assigned mountain-valley pattern. The first one folds two opposite hinges at the same time and describes the folding behavior of the first fold we made (Fig. 1.1a). The second branch also folds two hinges and describes the second fold we did (Fig. 1.1c). In this particular case, the branches are the folds we made to obtain the vertex, but in more complex origami patterns this does not have to be the case. Usually, branches involve hinges across multiple vertices [30] and describe the kinematics of origami patterns in the rigid origami model.

1.2.2. Folding behavior of origami patterns

Typically, origami is used to create 3D shapes from flat sheets of paper, but is it possible to create any 3D shape? In order to do this, we need to create curvature, like a dome or a saddle. This is impossible in the rigid origami model since the sheet of paper needs to stretch or bend [36], following Gauss's Theorema Egregium [37]. This theorem states that the Gaussian curvature of a surface is invariant under local isometry, and folding the surfaces is an isometric deformation. Nonetheless, this problem can be solved by approximating the curvature with flat triangles or squares. So, by applying a computational algorithm [38], we can obtain any shape from a flat sheet of paper [39, 40] such as a rabbit in Fig. 1.2a.

Currently, the origami models have been used as a tool to study mechanism behavior.

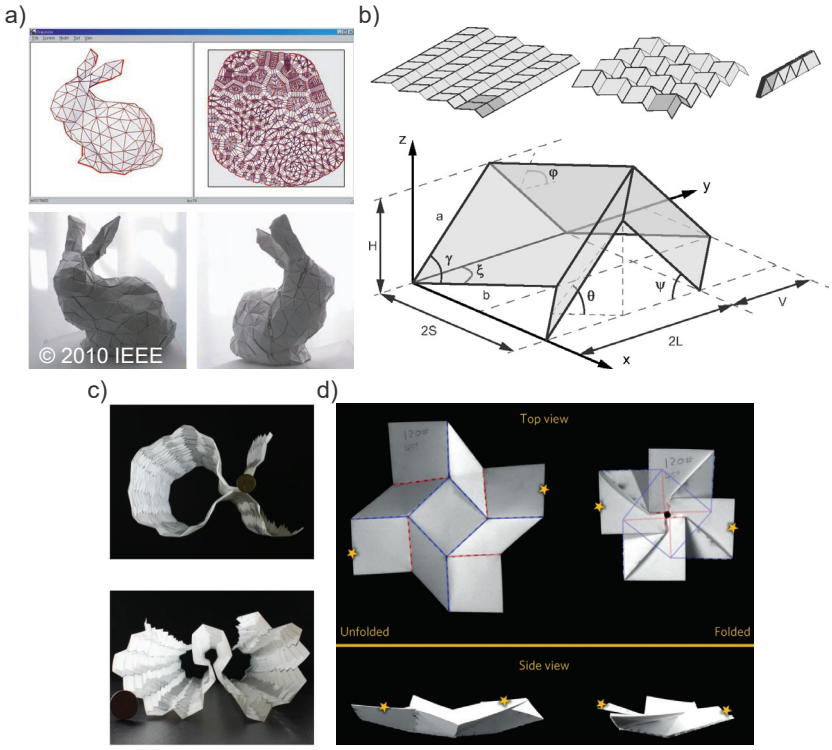

Figure 1.2 | a) Folding pattern and 3D shape of a origami structure that folds into a rabbit [40]. b) Folding behavior and geometry of Miura-ori pattern [41]. c) Pluripotent origami pattern folding into two shapes, α and ω. Reprinted by permission from Springer Nature Customer Service Centre GmbH: Springer Nature, Nature Physics [42], Copyright (2019). d) Stable states of a square twist pattern that are connected through face defromation in the elastic origami model. Reprinted by permission from Springer Nature Customer Service Centre GmbH: Springer Nature, Nature Materials [26], Copyright (2015).

For example, scientists have used origami concepts such as rigid- and flat-foldability to understand how to fold a map [17], a paper bag [18] or a strip of stamps [43]. Moreover, specific folding patterns have gained popularity due to their properties and applications. Some of the most well-known patterns are the Miura-ori pattern (Fig. 1.2b) [41, 44] first described as a deployable mechanism for solar panel in space [45], the waterbomb pattern [23] which snaps in one of two possible shapes [25], or the square twist [26], that depending on the mountain-valley allocation of the hinges can be rigid-foldable or not [35]. Importantly, the folding behavior of these patterns derives from their specific design.

By optimizing the design we can obtain complex behavior of origami. For example, most of the origami patterns have many branches crossing at the flat state [46]. Even, a generic 4-vertex has two branches. Since origami patterns are a collection of vertices in a sheet of paper, the branches of these vertices can accumulate, making it extremely difficult to fold patterns consisting of a large number of vertices [30]. However, by optimizing the designs of the origami pattern, the number of branches can be reduced to a

single one. This optimization is done by considering the interaction from vertices that form loops [47]. This type of origami is called self-folding origami [48, 49]. Another example of complex behavior comes from origami patterns that have not one, but many configurations after folding. This design has the potential to be folded in many ways and is therefore called pluripotent (Fig. 1.2c) [42].

The rigid origami model succeeds to describe the behavior of some origami patterns, however, the elastic origami model opens new behaviors where the rigid origami fails. The deformation of origami patterns in the elastic origami model cannot only be described by the fold angle of the hinges, but by additionally knowing the stretch and bend of the faces. This description adds many degrees of freedom that allow the structure to reach deformations previously not possible [27]. These new folding pathways open the possibility to reach also other stable states such as in Fig. 1.2d where the square twist can move between two stable states [26]. This multistability of origami has been studied particularly for origami patterns such as the hypar [29], the square twist [50], the 4-vertex [51] and the prismatic structures [52].

1.2.3. Origami-inspired metamaterials

Recently, origami patterns have moved away from flat sheets of paper [9, 53]. For example, we can create origami structures from 3D shapes [54]. These structures cannot be folded from a single sheet of paper, but they are still considered origami since their behavior remains the same, i.e., they fold along branches. Since the behavior is the same as traditional origami, some structures have the same properties such as flat- [55] or self-foldability [56, 57].

These origami-inspired structures can often be assembled into arrays since they have many symmetries. One structure is considered as a building block to create an array which is called a metamaterial. This assembly process allows the metamaterial to behave like a mechanism, e.g., by controlling only one hinge of a single building block we can obtain a global deformation where the entire array folds in the same way. Origami-inspired metamaterial are based on a variety of designs such as the Miura-ori pattern [27, 50, 58–60], the Sarrus linkage [61, 62] and prismatic structures [52, 54, 63] (Fig. 1.3a-c, respectively), among others [64–66].

Metamaterials exhibit behaviors that are rarely found in nature. They are not necessarily based on origami, but similar to origami, mechanical metamaterials are formed from assembling unit cells together in order to behave as a mechanism. Because of the mechanism-like behavior, they get their properties from their internal structure rather than from their chemistry [68, 69]. Some examples of their unusual properties are cloaking of stress by changing the arrangements of the unit cells [70], having a material respond differently depending on the place of deformation [67] or multistability [71] as with origami patterns.

Metamaterials base their unusual properties on the mechanism behavior. Following the behavior of the unit cell along the array, by applying a local force, the material deforms globally. This global deformation from local forces gives metamaterial a special characteristic that allows scientists to see them as mechanisms. This characteristic can also be seen in origami-inspired metamaterials since they move along branches. How-

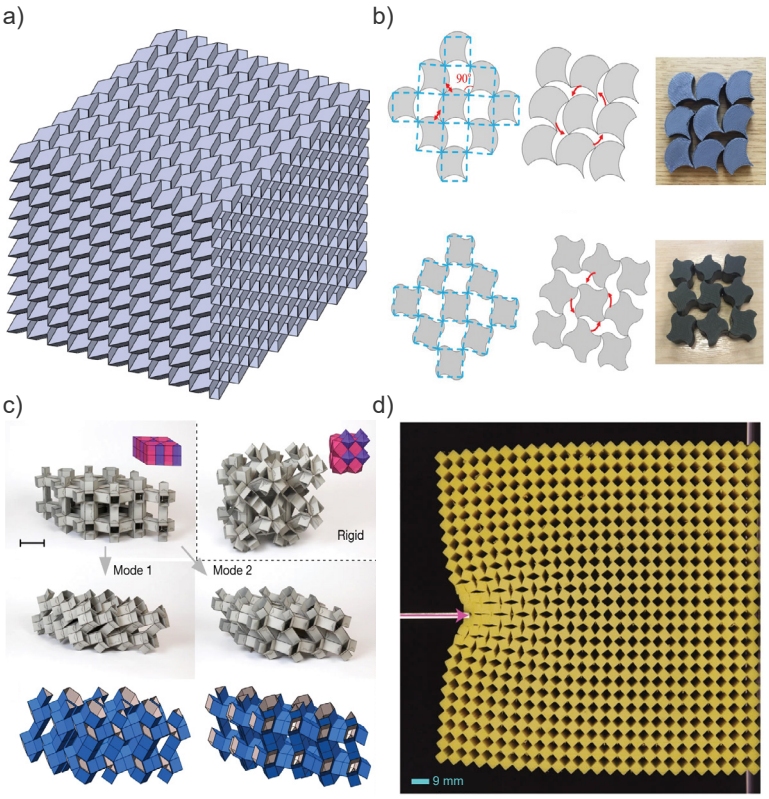

Figure 1.3 | Origami-inspired metamaterials based on a) the Miura-ori pattern (Reprinted from [59] Copyright (2019), with permission from Elsevier), b) a 2D Sarrus linkage (Reprinted from [61] Copyright (2018), with permission from ASME), and c) prismatic structures (Reprinted by permission from Springer Nature Customer Service Centre GmbH: Springer Nature, Nature [54], Copyright (2017)). d) Metamaterial based on rotating squares showing the area of influence of a local force (Reprinted by permission from Springer Nature Customer Service Centre GmbH: Springer Nature, Nature Physics [67], Copyright (2017)).

ever, this only applies when the behavior can be described by the rigid origami model. In the elastic origami model, as well as for any other metamaterial based on elastic components [72], the elasticity has a considerable influence on the global effect of a local force. The deformation triggered by a local force decreases the further it is from the location where the force is applied as seen in Fig. 1.3d. The consequence is that any local force will influence only a small area and not result in a global deformation.

1.3. Example: Sarrus linkage metamaterial

The problems arising from the elastic origami model can be exemplified with the folding behavior of a Sarrus linkage metamaterial. This example is based on a four-sided Sarrus linkage shown in Fig. 1.4a. According to the rigid origami model, this linkage follows one

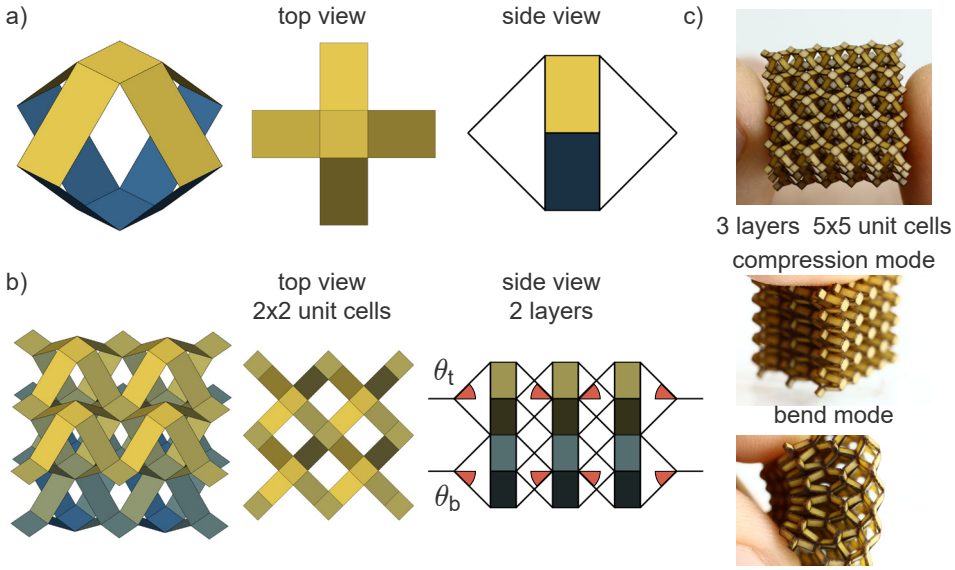

Figure 1.4 | Sarrus linkage metamaterial. a) Four-sided Sarrus linkage used as building block for a metamaterial. b) Array of building blocks connected diagonally forming a 2x2 metamaterial with 2 layers. The hinge angles from the top θ_t and the bottom θ_b layers can control the material. c) Fabricated metamaterial with a total size of ~ 4 cm. This prototype can move along two modes, the compression mode and the bend mode.

specific degree of freedom, a compression mode in which the linkage gets compressed on all the sides equally, acting like a mechanism. Any other deformation is constrained due to the spatial arrangements of hinges. By controlling one hinge, we can control the behavior of the rest of the structure. This mechanism characteristic is useful since it transforms local input (closing one hinge) into global behavior (folding the entire structure). Furthermore, we can assemble multiple Sarrus linkages by joining them diagonally (Fig. 1.4b), i.e., consider each linkage as a building block to build a metamaterial. This metamaterial still allows the structure to behave like a mechanism according to the rigid origami model. By controlling only one hinge of a single building block, we still observe a global deformation where the entire array folds together.

However, the rigid description of the behavior does not match the behavior seen in experiments. We performed these experiments on a prototype at the millimeter-scale that we produced using a laminate manufacturing technique [73]. This prototype not only moves along the compression mode, but it can also be relatively easily deformed in one additional mode, the bend mode (Fig. 1.4c and Movie 1.1 in Appendix D). This additional mode bends the material into a dome shape which is not predicted with the rigid origami model. The curved shape of the mode indicates that faces are bending or stretching [24], and points precisely to the weakness of the rigid origami model, namely that the constraints do not allow face deformations.

Therefore, we need to turn to an elastic origami model that does describe the observed behavior but adds many possible deformations. In the rigid origami model, a

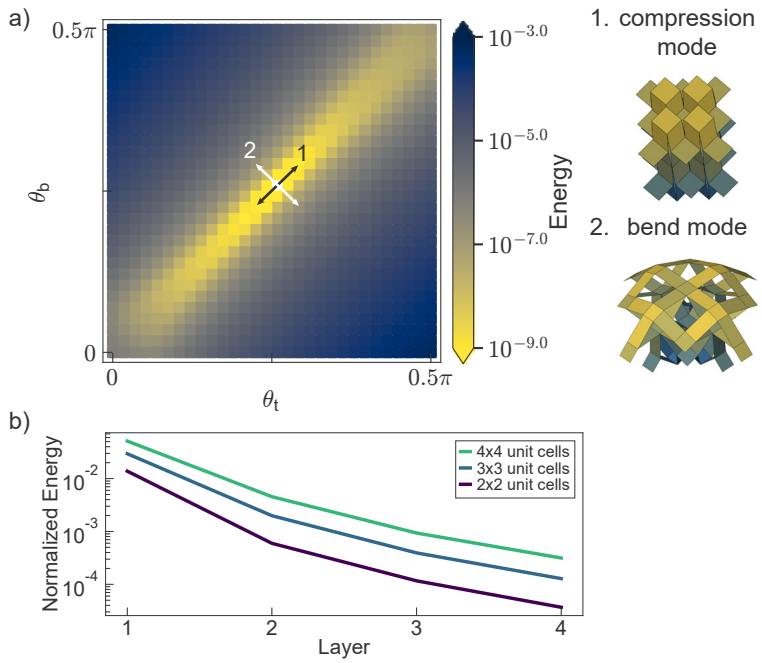

Figure 1.5 | Energy of the Sarrus metamaterial. a) Energy landscape of a metamaterial that shows how the energy changes along the two modes. b) Scaling of the energy when changing the number of layers for different material sizes.

single Sarrus linkage has 12 hinges and 10 faces, but its behavior can be described analytically with only one hinge. On the contrary, in the elastic origami model, the behavior includes all possible deformation of the faces such as bending and stretching. These deformations add many more possible modes that are nearly impossible to solve analytically. Therefore we use a numerical approach, further discussed in Chapter 2, in which we scan possible folding pathways by calculating the energy of deformations.

The elastic energy of the Sarrus linkage shows its non-linear behavior. We can control the behavior of the Sarrus metamaterial along the two deformation modes by controlling only two variables, the hinge angles from the top θ_t and the bottom θ_b layers (Movie 1.2 in Appendix D). Note that in general the selection of these variables in elastic origami is not trivial and in this case we were able to obtain them using a trail and error approach. Fig. 1.5 shows the dependency of the energy on these variables as a landscape, i.e., a projection of the full deformation space. We see two behaviors, related to the two deformation modes found in the prototypes: the energy does not increase along the compression mode ($\theta_t = \theta_b$), but it increases by several orders of magnitude along the bend mode ($\theta_t + \theta_b = \pi/2$). Despite that this energy landscape is just a projection of the complex energy landscape, it already demonstrates the existence of non-linear behavior. This non-linearity complicates to properly scan all possible deformations to obtain the most likely folding behavior.

Furthermore, the deformation is localized only where the forces are applied. This can be seen from the deformation produced by the bend mode of Sarrus metamaterials with different sizes. We apply a force to deform the hinges at the top and bottom layers of the materials. We then extract the energy and normalize it by the number of building blocks the material has. In Fig. 1.5 we see that this normalized energy depends on the number of layers. If the Sarrus metamaterial would act as a mechanism, the forces would deform the entire material and the energy would remain constant for each Sarrus linkage. Nonetheless, the energy decreases with the number of layers. This can be explained since the applied forces on the metamaterial remain equal but the number of building blocks increases, thus lowering the normalized energy. This shows that the applied forces cannot produce a global behavior, removing the mechanism characteristic of this metamaterial.

These problems are not particular to this specific example. Most of the metamaterial are fabricated at larger scales (>10 cm), nonetheless there is a tendency to produce them at smaller scales [74, 75] (<1 mm). At small scales, for example, the elasticity of the materials becomes more important [19, 76] as it becomes more difficult to build well articulated hinges, and therefore the rigid origami model cannot be used. It is necessary to have a better description of metamaterials that can predict their behavior accurately. In this thesis we address these problems with specific case studies, however the methods and descriptions can be applied to any origami pattern.

1.4. Objectives

As seen from the previous example, describing origami with a rigid model can result in interesting reconfigurable properties, however an elastic model is essential to describe new behaviors, such as the bending mode of the Sarrus metamaterial. Hence, in this thesis I focus on describing origami and origami metamaterials with an elastic model. However, applying this model comes at a cost. Elastic origami can be highly non-linear. This non-linearity derives not only from the interaction between the hinges defined by the pattern design, but also from the large number of degrees of freedom of the elastic model which allows interactions between folding hinges and deforming faces. This non-linearity makes it almost impossible to obtain an analytical description of the folding behavior, resulting in three main problems which I address in this thesis.

First, the additional deformation of the faces adds many parameters to the origami model that complicates the full scan of the origami behavior. In the rigid origami model, the deformation takes place only at the hinges which are modeled as rotational springs with a specific stiffness. However, in the elastic origami model, faces can deform. Each type of face deformation, i.e., bending or stretching, has an associated stiffness. These stiffnesses increase the parameter space of the model. Matching these stiffnesses to real life origami metamaterials is not straightforward. Consequently, the first objective of this thesis is:

> *Is it possible to simplify the model in order to study complex origami designs based on real life experiments?*

Second, it is almost impossible to search for new folding behaviors through all the

deformation space of origami structures with complex designs. The deformation space is defined as all possible deformations that a particular origami pattern has, which includes folding the hinges and deforming the faces. Characterizing the folding behavior in the deformation space can be compared to finding a needle in a haystack due to the large quantity of degrees of freedom. To do this, we need to create an algorithm that systematically deforms the origami structure in order to characterize its behavior. Therefore, the second objective of this thesis is:

Can we find a way to systematically characterize the deformation space in the elastic origami model?

Third, local deformation of origami patterns does not imply global deformation. Rigid origami behaves like a mechanism, meaning that a local deformation can trigger a global response. This mechanism-like behavior is also used in metamaterials that can reconfigure following the deformation of its unit cell. Nevertheless, elasticity adds not only many degrees of freedom along which the origami structure can deform, but also a characteristic length that defines how far a local force deforms the material [67]. This prevents global uniform deformation of the origami structure. This problem leads to the third objective of this thesis:

How can we obtain well-defined folding behavior in the elastic origami model?

Solving these main problems gives a deeper understanding of the folding behavior of elastic origami. Consequently the answers of these questions describe specific deformations that characterize the folding behavior of elastic origami as a result of external loading. This gives a guideline of possible actuation in real life origami-inspired metamaterials for a wide variety of applications.

1.5. In this thesis

In this section I describe briefly the different chapters of this thesis. In general, this thesis has the following structure. In Chapter 2 I present the elastic origami model that we use throughout the thesis. In Chapter 3 and 4 I propose two methods to scan systematically the deformation space to characterize the folding behavior of origami-inspired metamaterials using the elastic origami model. Last, in Chapter 5 I give a guideline for the arrangement of forces in an elastic origami metamaterial in order to obtain well-defined folding behavior depending on the material's stiffness.

In **Chapter 2**, I introduce the elastic origami model in detail. This model is based on a previous model, the bars-and-hinges model [20, 54]. It considers three basic types of origami deformations: hinge folding, face stretching and face bending. These deformations are defined as springs with certain stiffness. The energy of these springs can be calculated together with its derivative to obtain an energy landscape. Alongside, constraints are set to implement, for example, a maximum face strain, and adjacent self-contact, that ensures a behavior as close as possible to real life. We use this model in two different algorithms. In the first algorithm we solve the Euler Lagrange equations to obtain the normal modes of origami structures in an infinitesimal framework, and the

second algorithm helps to obtain the minimum energy deformation of the material in response of a stepwise increase of a force in a static framework.

In **Chapter 3**, I use the normal modes of elastic origami as a tool to classify the initial folding behaviors. For this, I, together with my collaborators, study the influence of elasticity on the origami behavior. Based on an eigenvalue problem [54, 56], we are able to obtain and separate the normal modes of the metamaterial in an infinitesimal deformation framework. Analysis of these modes allows us to define pseudo soft modes for materials that are rigid under the rigid origami model. These modes behave similar to the branches since their energy is mainly composed by folding hinges with minimal face deformation. Furthermore, we observe that this normal mode description depends highly on the stiffnesses of the different elastic origami deformations. Therefore, we obtain two reduced origami models that describe origami for any stiffness by constraining the face stretching and face bending. We observe that the first model relates to the rigid origami model and it is too restrictive to capture the pseudo soft modes of rigid structures, while the latter is comparable to the elastic model by deforming the structure through many normal modes, including the pseudo soft modes.

In **Chapter 4**, we systematically scan the highly non-linear energy landscape to find new origami behavior by closing hinges. We apply an energy minimization method to analyze origami metamaterials [54] in a fully non-linear framework. For this we use a static analysis for which we ignore any dynamic contribution. We exploit the symmetries of these origami metamaterials to obtain unique hinge combinations. We apply then a force to these hinge combinations as local actuation to deform the metamaterial. With this method we explore and visualize their complex energy landscape. This scanning method shows the existence of multiple stable states. Surprisingly, we find that some origami-inspired metamaterials have over 400 mechanically stable configurations.

Last, in **Chapter 5**, we use non-linear origami to observe the influence of elastic deformation in its folding behavior and propose an actuation pattern to obtain well-defined global behavior. Origami non-linearity usually is derived from the geometry of the pattern, but in this case we study non-linearity by embedding it to a simple 2D design [51, 77]. This design is used as a model in which we implement bistable hinges with non-linear behavior. These bistable hinges act as local forces that bend the hinges to specific angles. By performing energy minimization algorithms from a static framework with different metamaterial stiffness, we observe that the multistable behavior transitions from rigid origami to elastic origami. Whereas the rigid origami behavior is characterized by a deformation that spans throughout the material, the elastic origami behavior is separated by domain walls. Furthermore, by drawing a similitude to atomic crystals, we find an additional transition from elastic origami to amorphous material, in which the behavior changes between unit cells. This fundamentally changes the way in which the structure behaves and sheds light on a characteristic length that affects the area of influence of a given force. By knowing the stiffness of the material, we can obtain its folding behavior, and thus optimize the actuation pattern in order to obtain global deformations.

2

An energy description of elastic origami

Abstract

Typically, to study the folding behavior of origami, a rigid model is used, in which the only allowed deformation is the folding of the hinges while the faces remain rigid. However, interesting folding behavior can be achieved by allowing the deformation of the faces. This model is called the elastic origami model. Here, we describe a numerical model that represents the elastic origami. We base this numerical model on a bar-and-hinge model previously used to obtain the folding behavior of origami with imperfections and curvature. The numerical model consists of three elements: rotational springs that describe the folding of the hinges, and linear and rotational springs that describe the stretch and bend of the faces, respectively. Additionally, we describe linear and non-linear constraints to mimic the real-life behavior of the structures. This model is used throughout this thesis in two different algorithms: (i) we obtain the normal modes of the structure solving the Euler-Lagrange equation using the elastic and kinetic energy of the structure, and (ii) we obtain the elastic energy of the origami structure in order to search through the energy landscape for local minima, i.e., stable states. For these algorithms different sets of equations are used but the model can be applied to any origami pattern to obtain its folding behavior.

In the elastic origami model, origami patterns are allowed not only to fold the hinges, but also to deform the faces, i.e., faces can stretch and bend. To simulate the deformation behavior of origami-inspired metamaterials, we implement a numerical model based on previous models that describe an elastic origami behavior such as the bar-and-hinge model [20, 54, 78]. The bar-and-hinge model has been used to describe accurately origami deformation, such as curved origami patterns [22] or origami with imperfections [79], and was derived from an hyperelastic framework. Here we use an intuitive model based on springs that qualitatively describes the behavior of origami using fewer parameters than previous models.

The numerical model consist of three elements: rotational springs that model the folding of the hinges, linear springs that model the stretching of the faces, and rotational springs that model the bending of the faces. Each spring in the model has an associated elastic energy that contributes to the energy landscape of the origami structure. We use additional springs to model forces that we can apply to deform the origami.

We use this elastic origami model for two types of analysis. First, in Chapter 3, we solve the Euler-Lagrange equations in an infinitesimal deformation framework to obtain the normal modes of the structures by calculating also the kinetic energy in a dynamic framework. Second, in Chapter 4 and 5, by minimizing the elastic energy of the deformation, we traverse the landscape to find local minima, i.e., stable states. This is done in a static framework in which any dynamic contribution is ignored. We use the gradient of the elastic energy to provide a direction of search, reducing the calculation time. For both analysis we use constraints to prohibit deformations that are not allowed in real life prototypes such as face crossing and a maximum face strain.

While the model accounts for the three most probable deformations in origami, there are other deformations that are not considered. The bending and stretching of the faces is modeled uniformly throughout the face, nonetheless these deformations are not necessarily uniform for large faces, they can be localized at specific regions. Additionally, hinges can have deformations such as stretching and twisting that are not implemented in our numerical model.

In this chapter, we first define geometrically the origami structure. We then derive the elastic energy associated with hinge folding, face stretching and face bending, the work applied to deform the structure, and the kinetic energy of the metamaterial. Next, we derive the required face bending, angle, edge stretch, and face stretch constraints to obtain behaviors closer to real metamaterials and reduce the numerical complications, and the periodic boundary conditions to simulate infinite large materials. Finally, we describe the implementation of this energy in the elastic energy minimization algorithm in *Matlab* and the general usage of the model for each chapter.

2.1. Geometrical structure of origami

For this model, origami patterns are composed by F faces, each one surrounded by S_E edges and divided by S_D diagonals. Diagonals are defined only for faces with more than three edges. At the corner of the faces we define V vertices. Edges that connect two faces are defined as hinges (H). We describe the complete shape of the origami structure by the coordinates of its vertices $\boldsymbol{x} = [x_{1,1}, x_{2,1}, x_{3,1}, x_{1,2}, \ldots, x_{3,V}]$. The coordinate of the

initial position of the origami structure is define by $\boldsymbol{X}$.

2.2. Elastic energy

Three types of elastic energies are assigned to the origami pattern: the hinge folding energy E_{hinge} modeled as torsional springs placed at the hinges, the face stretch energy E_{stretch} modeled as linear springs placed at the edges and the diagonals of each face, and the face bending energy E_{bend} modeled as torsional spring along one of the diagonals of each face. The total elastic energy of the structure is given by

$$E_{\text{elastic}} = E_{\text{hinge}} + E_{\text{stretch}} + E_{\text{bend}}. \tag{2.1}$$

The gradient of E_{elastic} with respect to the displacement of the vertices $\boldsymbol{u} = \boldsymbol{x} - \boldsymbol{X}$ is then equal to

$$d\boldsymbol{E}_{\text{elastic}} = d\boldsymbol{E}_{\text{hinge}} + d\boldsymbol{E}_{\text{stretch}} + d\boldsymbol{E}_{\text{bend}} = \frac{\partial E_{\text{hinge}}}{\partial \boldsymbol{u}} d\boldsymbol{u} + \frac{\partial E_{\text{stretch}}}{\partial \boldsymbol{u}} d\boldsymbol{u} + \frac{\partial E_{\text{bend}}}{\partial \boldsymbol{u}} d\boldsymbol{u}. \tag{2.2}$$

2.2.1. Hinge folding energy

To model the hinges we consider two different types of behaviors, a linear hinge for Chapter 3 and 4, and a bistable hinge for Chapter 5. Linear hinges are modeled as torsional springs with an angle Ω in the initial state, θ in the deformed state and stiffness k_{h}. The linear hinge energy E_{hinge} is defined as

$$E_{\text{hinge}}(\boldsymbol{\theta}) = \sum_{i=1}^{H} \frac{1}{2} k_{\text{h}} (\theta_i - \Omega_i)^2 = \frac{1}{2} k_{\text{h}} (\boldsymbol{\theta} - \boldsymbol{\Omega}) \cdot (\boldsymbol{\theta} - \boldsymbol{\Omega}), \tag{2.3}$$

where $\boldsymbol{\theta} = [\theta_1, \theta_2, ..., \theta_H]$ and $\boldsymbol{\Omega} = [\Omega_1, \Omega_2, ..., \Omega_H]$. Each fold angle can be found from the coordinates of the vertices according to

$$\theta = \tan^{-1}\left(\frac{\mathbf{a}_{\text{h}} \cdot (\mathbf{n}_{\text{a}} \times \mathbf{n}_{\text{b}})}{\mathbf{n}_{\text{a}} \cdot \mathbf{n}_{\text{b}}} \right), \tag{2.4}$$

in which $\boldsymbol{n}_a$ and $\boldsymbol{n}_b$ are the normal vectors of the two faces connected by the hinge, and the vector $\boldsymbol{a}_h$ lies along the hinge axis (Fig. 2.1a). Note that we use the function $\tan^{-1}$ (instead of using $\theta = \cos^{-1}(\boldsymbol{n}_a \cdot \boldsymbol{n}_b)$) since its domain is defined for $(-\infty, \infty)$ and the angle ranges between $[-\pi, \pi]$ using a four-quadrant inverse tangent. Since we use this model for infinitesimal deformation or with face bending constraint, the normal vectors are always uniquely defined. Partial derivatives of the fold angles with respect to vertex displacement can then be found according to

$$\frac{\partial E_{\text{hinge}}}{\partial \boldsymbol{u}} = \frac{\partial E_{\text{hinge}}}{\partial (\boldsymbol{\theta} - \boldsymbol{\Omega})} \frac{\partial (\boldsymbol{\theta} - \boldsymbol{\Omega})}{\partial \boldsymbol{u}} = k_{\text{h}} (\boldsymbol{\theta} - \boldsymbol{\Omega}) \mathbf{J}_{\text{hinge}}, \tag{2.5}$$

in which $\mathbf{J}_{\text{hinge}}$ is a Jacobian matrix with entries

$$\mathbf{J}_{\text{hinge}[i,3(\nu-1)+j]} = \frac{\partial \theta_i}{\partial x_{j,\nu}}, \tag{2.6}$$

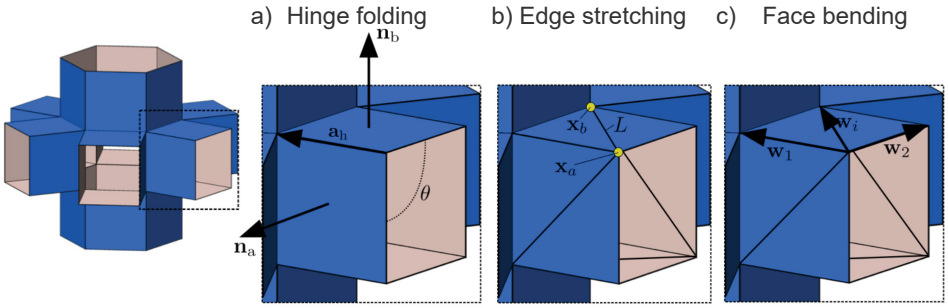

Figure 2.1 | Schematic of the extruded unit cell [54] showing the vectors used to calculate the respective energy.

for $i = 1,\dots,H$, $j = 1,2,3$ and $v = 1,\dots,V$. For a more detailed explanation and description of the Jacobian see ref. [54].

Bistable hinges are modeled as a symmetric double-well potential energy $E_{\text{bi-hinge}}$. Note that despite this hinge is defined as bistable, it does not define the stability of the origami metamaterial which is determined by the interaction of these hinges through the design pattern. We define the energy of the bistable hinge to be zero at the rest angles Θ and $-\Theta$, with an energy barrier of k_h thus following

$$E_{\text{bi-hinge}}(\boldsymbol{\theta}) = \sum_{i=1}^{H} k_\text{h} \frac{(\theta_i^2 - \Theta_i^2)^2}{\Theta_i^4} = k_\text{h} \frac{(\boldsymbol{\theta}\cdot\boldsymbol{\theta} - \boldsymbol{\Theta}\cdot\boldsymbol{\Theta})^2}{(\boldsymbol{\Theta}\cdot\boldsymbol{\Theta})^2}, \tag{2.7}$$

where $\boldsymbol{\Theta} = [\Theta_1,\dots,\Theta_H]$. Note that the hinge is at an energy maximum when placed in its flat state $\theta = 0$, and has equal probability to fold either way. The fold angle θ is defined by Eq. 2.4. Using this equation we can define the partial derivative as

$$\frac{\partial E_{\text{bi-hinge}}}{\partial \boldsymbol{u}} = \frac{\partial E_{\text{bi-hinge}}}{\partial \boldsymbol{\theta}} \frac{\partial \boldsymbol{\theta}}{\partial \boldsymbol{u}} = 4k_\text{h} \frac{(\boldsymbol{\theta}\cdot\boldsymbol{\theta} - \boldsymbol{\Theta}\cdot\boldsymbol{\Theta})\boldsymbol{\theta}}{(\boldsymbol{\Theta}\cdot\boldsymbol{\Theta})^2} \mathbf{J}_{\text{hinge}}, \tag{2.8}$$

where the Jacobian $\mathbf{J}_{\text{hinge}}$ is defined by Eq. 2.6.

2.2.2. Face stretching energy

Stretching of each face is modeled using linear springs placed along the edges and diagonals. While Filipov et al. [56] derived specific expressions for the stiffness of each spring, we simplify our model by assuming that all springs have stiffness k_s. The face stretching energy E_{stretch} can be found according to

$$E_{\text{stretch}} = \sum_{i=1}^{S_E+S_D} \frac{1}{2} k_\text{s} (l_i - L_i)^2 = \frac{1}{2} k_\text{s} (\boldsymbol{l} - \boldsymbol{L})\cdot(\boldsymbol{l} - \boldsymbol{L}), \tag{2.9}$$

in which L_i and l_i correspond to the initial and deformed length of the i-th edge, respectively, $\boldsymbol{L} = [L_1,\dots,L_{S_E+S_D}]$ and $\boldsymbol{l} = [l_1,\dots,l_{S_E+S_D}]$. Furthermore, the change in length of each edge can be found from the displacement of the two corresponding vertex displace-

ments (Fig. 2.1b)

$$l - L = \sqrt{\sum_{i=1}^{3} (u_{i,a} - u_{i,b})^2}. \tag{2.10}$$

The partial derivative of the face stretching energy then equals

$$\frac{\partial E_{\text{stretch}}}{\partial \boldsymbol{u}} = \frac{\partial E_{\text{stretch}}}{\partial (\boldsymbol{l} - \boldsymbol{L})} \frac{\partial (\boldsymbol{l} - \boldsymbol{L})}{\partial \boldsymbol{u}} = k_{\text{s}} (\boldsymbol{l} - \boldsymbol{L}) \mathbf{J}_{\text{stretch}}, \tag{2.11}$$

where $\mathbf{J}_{\text{stretch}}$ is a Jacobian with entries

$$\mathbf{J}_{\text{stretch}[i,3(v-1)+j]} = \frac{\partial l_i}{\partial x_{j,v}}, \tag{2.12}$$

for $i = 1, \ldots, S_E + S_D$, $j = 1,2,3$ and $v = 1, \ldots, V$.

2.2.3. Face bending energy

Bending of the faces is modeled as a torsional spring on the diagonal of each face. When faces have more than 4 sides, the number of diagonals increases. In order to minimize the calculation time of all these torsional springs, we consider only the out-of-plane displacement of each vertex on a face. This out-of-plane displacement can be related to the angle in which the face bends. A stiffness k_b is related to the face bending energy according to

$$E_{\text{bend}} = \sum_{i=1}^{V_{\text{F}}} \frac{1}{2} k_{\text{b}} (z_i)^2 = \frac{1}{2} k_{\text{b}} \boldsymbol{z} \cdot \boldsymbol{z}, \tag{2.13}$$

in which z_i is the out-of-plane displacement ($\boldsymbol{z} = [z_1, \ldots, z_{V_{\text{F}}}]$), $V_{\text{F}} = \sum^{F} (V_f - 3)$ are the nodes that can be misaligned to the rest of face, and V_f is the total number of vertices of the f-th face.

To determine the out-of-plane deformation we use two vectors $\boldsymbol{w}_2$ and $\boldsymbol{w}_3$ on a face to get its normal and project the remaining edge vectors ($\boldsymbol{w}_i$ for $i = 4, \ldots, V_f$) onto the face. For each face, we then have (Fig. 2.1c)

$$z_i = \boldsymbol{w}_i \cdot (\boldsymbol{w}_2 \times \boldsymbol{w}_3), \tag{2.14}$$

for $i = 4, \ldots, V_f$.

The partial derivative of the face bending energy is then given by

$$\frac{\partial E_{\text{bend}}}{\partial \boldsymbol{u}} = \frac{\partial E_{\text{stretch}}}{\partial \boldsymbol{z}} \frac{\partial \boldsymbol{z}}{\partial \boldsymbol{u}} = k_{\text{b}} \boldsymbol{z} \mathbf{J}_{\text{bend}}, \tag{2.15}$$

where $\mathbf{J}_{\text{bend}}$ is a Jacobian with entries

$$\mathbf{J}_{\text{bend}[i,3(v-1)+j]} = \frac{\partial z_i}{\partial x_{j,v}}, \tag{2.16}$$

for $i = 1, \ldots, V_{\text{F}}$, $j = 1,2,3$ and $v = 1, \ldots, V$.

2.3. Applied work

In order to deform the metamaterial, we specify a target angle for A hinges, and apply a penalty method to increase the energy by E_{load}, seen as work energy, in case the target angles are not satisfied. The total energy of the system E that includes both the elastic deformation and the loads is then equal to

$$E = E_{\text{elastic}} + E_{\text{load}}, \tag{2.17}$$

in which

$$E_{\text{load}} = \sum_{i=1}^{A} \frac{1}{2} k_{\text{p}} (\theta_i - \hat{\Omega}_i)^2, \tag{2.18}$$

k_{p} sets the stiffness of the applied penalty and $\hat{\Omega}_i$ is the target angle of the i-th hinge to which a load has been applied. Note that for $k_{\text{p}} \gg k_{\text{h}}$ we are practically constraining the angles to the target angles of the loaded hinges, while for smaller values of k_{p} the target angles might not be reached.

2.4. Kinetic energy

We calculate the kinetic energy in order to obtain the normal modes of the origami pattern in Chapter 3 only. To determine the kinetic energy of the metamaterial we need to know the mass of the metamaterial. For this we assume a planar density of 1 thus we give each face a mass depending on their area. This mass is then distributed equally among the vertices that form the face. Since we obtain the normal modes from an infinitesimal deformation framework, we assume that the mass distribution is constant. The kinetic energy follows

$$E_{\text{kinetic}} = \sum_{i=1}^{V} \frac{1}{2} M_i \left(\frac{dx_{1,i}}{dt} + \frac{dx_{2,i}}{dt} + \frac{dx_{3,i}}{dt} \right)^2 = \frac{1}{2} \dot{\boldsymbol{u}}^T \boldsymbol{M} \dot{\boldsymbol{u}}, \tag{2.19}$$

where $\dot{\boldsymbol{u}} = \partial \boldsymbol{u} / \partial t$, M_i is the mass assigned for each vertex, and $\boldsymbol{M}$ is the corresponding mass matrix of size $3V \times 3V$.

2.5. Constraints

While with the derivation of E_{elastic} we have specified the energy landscape of our origami metamaterials, certain deformations are not admissible or need to be constrained for the different chapters. In contrast with the bar-and-hinge model [20] where these deformations are prohibited from the constituent elements, here we need to specify them to prevent singularities. In this section, we present six different constraints that we implemented to limit the deformation. Specifically, we discuss how to fix vertices to remove rigid body translations and rotation, prevent face bending, limit the fold angle to implement contact, limit the edge stretching and face stretching to prevent numerical convergence problems, and simulate infinite periodic tilings of a building block using periodic boundary conditions.

2.5.1. Vertex displacement constraint

To prevent rigid body translations we select one vertex from a face of the origami metamaterial $\boldsymbol{X}_1$ and fix the displacement to $\boldsymbol{u}_1 = (0,0,0)$. Moreover, to avoid rigid body rotations we fix two other vertices on the same face $\boldsymbol{X}_2$ and $\boldsymbol{X}_3$ according to

$$\boldsymbol{u}_2 \cdot (\boldsymbol{X}_2 - \boldsymbol{X}_1) \times (\boldsymbol{X}_3 - \boldsymbol{X}_1) = 0, \tag{2.20}$$

$$\boldsymbol{u}_3 \cdot (\boldsymbol{X}_2 - \boldsymbol{X}_1) \times (\boldsymbol{X}_3 - \boldsymbol{X}_1) = 0, \tag{2.21}$$

$$\boldsymbol{u}_2 \cdot (\boldsymbol{X}_3 - \boldsymbol{X}_1) = 0. \tag{2.22}$$

2.5.2. Face bending constraint

To ensure that no face bending can occur, we impose that the out-of-plane displacement (Eq. 2.14) of each vertex on a face remains zero. For each face, we then have

$$z_i = 0. \tag{2.23}$$

Note that the gradient of this constraint is given by Eq. 2.16.

2.5.3. Fold angle constraint

We need to limit rotation of the hinge since each hinge connects two faces which come into contact when $\theta = -\pi$ or π, representing a fully closed hinge. Because we use a four-quadrant inverse tangent to determine the angles of the hinges between two adjacent faces (Eq. 2.4), the angle can vary between $-\pi \leq \theta \leq \pi$. However, when the two faces cross each other, the fold angle will have a real value that lies outside the range of the inverse tangent. To avoid this problem, we ensure that the faces never cross by applying a tighter constraint to the fold angles

$$-0.985\pi < \theta_i < 0.985\pi, \tag{2.24}$$

where the limits have been determined by visually analysing several simulations to determine the value for which the faces have crossed. Note that the gradient for this constraint is given by Eq. 2.6.

Additionally, we also implemented other precautionary measurements to avoid adjacent face crossing. We keep track of the angles of previous iteration step such that a sudden change in angle larger than π indicates the crossing of the two faces. If this occurs, depending on the sign of the step, we add or subtract 2π to have the real value outside the range $-\pi \leq \theta \leq \pi$. When using a minimization algorithm we limit the step-size of the function so that the difference in angles between steps cannot become greater than π if no adjacent face crossing occurs.

2.5.4. Edge stretch constraint

While stretching is permitted in both simulations and experiments, our simulations shows convergence problems when higher stretches occur. For example, when the edges of a flat face form a concave polygon, the normal of the initially rectangular face becomes

ill-defined. This could occur when the maximum strain of an edges of the faces become larger than 0.17. Nevertheless, we found this constraint too tight as it was prohibiting large deformations on the metamaterial and the search for stable states. Therefore, we loosen this constraint in our simulations to a maximum strain of edges according to

$$-0.30 \leq \frac{l_i - L_i}{L_i} \leq 0.30, \tag{2.25}$$

where l_i and L_i are the deformed and original length of an edge or diagonal, respectively. For all simulations, this value did not produce ill-defined normals. The gradient for this constraint is given by the normalized Jacobian of Eq. 2.12, and equals

$$\mathbf{C}_{\text{e-stretch}[i,3(v-1)+j]} = \frac{1}{L_i}\frac{\partial l_i}{\partial x_{j,v}}, \tag{2.26}$$

for $i = 1,\ldots,S_E + S_D$, $j = 1,2,3$ and $v = 1,\ldots,V$.

Additionally, we can also have a stricter constraint, for example for Chapter 3 we constraint any stretching of the edges following

$$l_i - L_i = 0. \tag{2.27}$$

2.5.5. Face area constraint

Furthermore, we notice that for some origami metamaterials the faces can become ill-defined when minimizing the energy. For example, when the face is a triangle, the edges can stretch within the edge stretching limit to become co-linear, reducing the face area to zero and turning the normal vector of the face ill-defined. This results in problems when calculating the fold angle. Therefore, we apply a constrain on the area of the faces (A_i for $i = 1,\ldots,F$) following

$$0.1 \leq A_i = \frac{1}{2}\sqrt{\boldsymbol{n}_i \cdot \boldsymbol{n}_i}. \tag{2.28}$$

where $\boldsymbol{n}_i$ is the normal vector of the face. This constraint ensures that all areas are well defined. The partial derivative of this constraint is given by

$$\mathbf{C}_{\text{f-stretch}[i,3(v-1)+j]} = \frac{1}{2}\frac{\boldsymbol{n}_i}{\sqrt{\boldsymbol{n}_i \cdot \boldsymbol{n}_i}}\frac{\partial \boldsymbol{n}_i}{\partial x_{j,v}}, \tag{2.29}$$

for $i = 1,\ldots,F$, $j = 1,2,3$ and $v = 1,\ldots,V$.

2.5.6. Periodic Boundary conditions

To create infinite large metamaterial of the origami building block, instead of copy the structure and tessellate it, we apply periodic boundary conditions. These boundary conditions are implemented along the lattice vectors $\boldsymbol{P}_i$ for $i = 1,...,n_{\text{dim}}$ which define the repetition pattern in the infinite metamaterial. Depending on the number of lattice vectors ($n_{\text{dim}} \in [1,2,3]$), they can span the material in one, two or three dimensions. For the undeformed building block, two vertices are periodically located when

$$\boldsymbol{X}_{\text{b}} - \boldsymbol{X}_{\text{a}} = \sum_{i=1}^{n_{\text{dim}}} \alpha_i \boldsymbol{P}_i, \tag{2.30}$$

where $\boldsymbol{X}_\mathrm{a}$ and $\boldsymbol{X}_\mathrm{b}$ are the initial positions of the vertices, and $\alpha_i \in [-1, 0, 1]$ represents the possible linear combination of the lattice vectors for tiling the unit cell in space. Then, periodic boundary conditions can be applied to these periodically located vertex pairs according to

$$u_\mathrm{b} - u_\mathrm{a} = \sum_{i=1}^{n_\mathrm{dim}} \alpha_i \boldsymbol{p}_i, \tag{2.31}$$

in which $\boldsymbol{p}_i$ represents the deformation of the lattice vector.

2.6. Implementation

This model description gives an overview of the equations used for the different chapters, however, not all equations were used at the same time. Depending on the studied structure and the analysis of each chapter, we use a different set of equations.

For Chapter 3 we obtain the normal modes by solving the Euler-Lagrange equation. This is done only around an initial state on an infinitesimal deformation framework. For this we employ the elastic energy (Eq. 2.1) and the kinetic energy (Eq. 2.19). We then constraint the face bending following Eq. 2.23 or the face stretching with Eq. 2.27 to obtain two reduced models.

For Chapter 4 the elastic energy will be composed only by the linear hinge folding energy (Eq. 2.3) and the face stretching energy (Eq. 2.9). We then minimize the total energy (Eq. 2.17) with linear and non-linear constraints in order to find stable states. This is done in a static analysis in which any dynamic contribution is ignored. The linear constraints prevent rigid body translations (Eqs. 2.20–22) and enforce boundary conditions (Eq. 2.31), while the non-linear constraints restrict the out-of-plane deformation (Eq. 2.23), avoid adjacent face crossing (Eq. 2.24), and set a maximum edge stretch (Eq. 2.25).

For Chapter 5 we use the bistable hinges (Eq. 2.7) together with the face stretching energy (Eq. 2.9) to define the total energy of the structure. In this chapter we also minimize the energy to find the stable configurations of large arrays of origami-inspired metamaterials in a static analysis. To minimize the energy after deformation, we use a set of linear constraints that avoids rigid body translations (Eqs. 2.20–22) and non-linear constraints that besides restricting the out-of-plane deformation (Eq. 2.23), and avoiding adjacent face crossing (Eq. 2.24), set a minimum area for the compressing of the faces (Eq. 2.28).

We implement the aforementioned set of equations in *Matlab*. For the normal mode algorithm of Chapter 3, we solve the Euler Lagrange equations through an eigenvalue problem. For the energy minimization analysis of Chapter 4 and 5, we use the build-in constrained non-linear multivariable function called *fmincon* that optimizes a function in steps. In each step the function, i.e., the energy, and its derivative, i.e., its Jacobian, is computed. From this function we use the optimization algorithm, *Sequential Quadratic Programming* (SQP). In this algorithm the step size is not limited and therefore converges faster than other algorithms to the energy minimum. Nevertheless, we fold the structures in optimization steps to ensure optimal deformation. For a more precise minimization of the energy, we use another optimization algorithm, *Active-set* in which a maximum step size can be defined making the deformation of all the fold angles more

reliable with the cost of simulation time. We choose the *Active-set* algorithm only for the simulations of the energy landscape (Figs. 4.3, B.3 and B.4) and the compression test simulation (Figs. 4.2 and B.1) in Chapter 4.

3

Elastic folding behavior of prismatic structures

Abstract

Origami is usually studied as rigid faces connected by hinges that can fold. This description localizes the deformation at the hinges, facilitating the description of the kinematics of origami patterns through branches. Nevertheless, this model ignores deformations that could occur at the faces which could significantly alter the pattern kinematics. To account for these deformations, we use an elastic origami model. This model adds many degrees of freedom, making the origami kinematics difficult to describe. Here, we obtain the kinematics of a type of origami patterns called prismatic structures by obtaining the normal modes of the structures in an infinitesimal deformation framework. We show the existence of soft modes that behave like the branches in the rigid origami model, and pseudo soft modes that are closely related since their deformation takes place mostly at the hinges with minimal face deformation but are not captured by the rigid origami model. Furthermore, we notice mode interactions that complicates the classification of the normal modes across different stiffness regimes. Therefore, we test two constrained models to obtain such classification, and we show that the model that allows for face stretching but constrains the face bending rises as a simpler model to describe elastic origami. We present this reduced model as a tool to search for new folding behaviors of origami-inspired metamaterials for a wide range of applications.

Based on: Iniguez-Rabago, A., and Overvelde, J.T.B., *Elastic folding behavior of prismatic structures.* (In preparation)

Origami has recently been used as inspiration to create mechanisms with multiple functionalities [80]. These mechanisms can be used to create metamaterials which derive their properties from their specifically designed mesoscopic architecture [69]. Origami-inspired metamaterials have been widely used across several fields for example in architecture [3, 4] as responsive facades [6], biology [12, 13] as a structure to sense DNA [16], and engineering [7–9] as crawling mechanisms [81]. To understand the folding behavior and to design metamaterials with new properties, origami metamaterials are often modeled as a set of rigid faces connected by hinges, i.e., a rigid origami model. In this model, origami structures can only deform by folding a set of hinges through a limited number of pathways, i.e., branches, that are defined by the arrangements of the faces and hinges. By carefully designing the origami structures scientist have obtained metamaterials with rare properties such as self-folding origami [46, 49, 82] that deform along only one branch, pluripotent metasheets [42] in which multiple 3D deformations can be designed from 2D sheets, or reconfigurable structures based on extruded polyhedra [54]. The rigid origami model describes the behavior of these structures under the assumption that all deformations are localized at the hinges, nevertheless, this assumption is not always met, for example in small-scale origami metamaterials [19], or in origami with imperfections [79, 83–85].

To account for additional deformation, scientist have extended the rigid origami model to an elastic origami model. This model considers deformations not only at the hinges, but also at the faces that are allowed to stretch or bend. As a result, the branches become soft modes, and deformations outside of these soft modes become possible due to the increased degrees of freedom of the structure. As such, the elastic origami model allows new origami behaviors, such as folding pathways [26, 27] that are impossible assuming the rigid origami model, and stable states that could not be reached before [21, 29, 50, 52, 71]. However, these new folding pathways are not well-defined, since it is almost impossible to solve the kinematics of these structures analytically due to the increased number of degrees of freedom. This is the case even for simple designs, such as single vertices [51]. Therefore, we are interested to determine if can we identify soft modes in elastic origami that are close to rigid origami, but are not captured by the rigid origami model. And if so, determine how these modes depend on geometry and material stiffnesses.

Here, we obtain the kinematics of a type of origami-inspired metamaterials based on extruded polyhedra [54] by solving an eigenvalue problem [56] in an infinitesimal deformation framework. The solution of this problem results in the normal modes of the structure, which describe the degrees of freedom of the structure as possible deformation pathways. First, we describe in detail the numerical model used to obtain the normal modes. We apply this model to two structures that behave differently according to the rigid origami model to understand the deformation of such modes. While we obtain the expected soft modes of origami structures that have branches in the rigid origami model, we also obtain pseudo soft modes for structures that are rigid under the rigid origami model. These pseudo soft modes behave similarly to the branches since most of the deformation is localized at the hinges with minimum face deformation. Then, we study the dependency of the normal modes on the stiffnesses of the model and encounter mode interactions. These interactions make a general description of the normal

modes across different stiffness relations impossible to have. Therefore, we simplify the elastic origami model into two different reduced models to obtain such general description. We show that the behavior described by these two models differs fundamentally, one being closer to the rigid origami model and the other to the elastic origami model. We propose to use the reduced model that resembles the elastic origami model to obtain the folding pathways of origami structures, as a general approach in the search for new origami behaviors.

3.1. Kinematic model

In order to exemplify the kinematics of origami structures, we focus on a library of origami-inspired metamaterials based on convex polyhedra, i.e., prismatic structures. Each polyhedra can be used as a template for a thin walled structure that is built by extruding its edges in the normal direction of each face (Fig. 3.1a). We assume that the deformation of these structures can be described only through the displacements of their vertices which are located at the corners of each face. We chose these structures because they illustrate a range of possible behaviors observed in the rigid origami model, e.g., some of them can deform along branches while others are completely rigid [54]. In fact, by analyzing them with the elastic origami model in a full geometrically non-linear framework, all of these structures can deform into multiple stable states [52]. Nevertheless, our method can be applied to a variety of origami structures.

Typically, in the elastic origami model, the folding of the hinges is modeled as rotational springs, and the stretching and bending of the faces is modeled as rotational and linear springs, respectively. The assumption that faces can deform adds many degrees of freedom when compared to the rigid origami model. For example, a structure based on a cube in the rigid origami model has 3 degrees of freedom, i.e., branches [55], while in the elastic origami model each vertex of the extrusions can move independently from its neighbours. Note that this displacement requires elastic energy, but it is not constrained, such that, each vertex has 3 translational degrees of freedom adding up to 96 degrees of freedom for this structure. These degrees of freedom define the kinematics of the structures, however, they do not give any information about the preferred deformation of the structure.

To better describe the elastic behavior of origami structures, we employ a dynamic eigenvalue problem that represent the deformation of the structure according to a set of normal modes. This numerical model, previously described for the rigid origami model [54], and in the elastic origami model for different structures [86], solves the Euler-Lagrange equation of motion by solving the eigenvalue problem $\boldsymbol{K}^{-1}\boldsymbol{M}\boldsymbol{v} = \lambda\boldsymbol{v}$ [56] (Appendix A). Here, $\boldsymbol{M}$ and $\boldsymbol{K}$ are defined as the mass and stiffness matrix, respectively, and $\boldsymbol{v}$ is the eigenmode with its corresponding eigenvalue λ. We determine the mass matrix $\boldsymbol{M}$ assuming a homogeneous mass density. Note that, since we are only consider normal modes at a specific deformation, i.e., the initial states, due to the infinitesimal deformation framework, the mass matrix is constant. Importantly, the stiffness matrix $\boldsymbol{K}$ is the result of the addition of three different matrices corresponding to the three different allowed deformations that can occur in the elastic origami model: hinge folding ($\boldsymbol{K}_{\text{hinge}}$), face stretching ($\boldsymbol{K}_{\text{stretch}}$), and face bending ($\boldsymbol{K}_{\text{bend}}$). At the same time, each of these ma-

trices is associated to the stiffness of the springs in the model, k_h, k_s and k_b, respectively.

Importantly, the eigenmode ($\boldsymbol{v}$) corresponds to the normal mode of the structure, and represents the deformation of the structure along this mode. This deformation is an infinitesimal approximation of the motion from the initial state, therefore, any small deformation from this state can be described as a linear composition of the normal modes. The corresponding eigenvalue λ relates to the excitation frequency of the normal mode and to the energy of the system with the corresponding normal mode deformation. The lower the eigenvalue is, the lower the elastic energy is required to deform the structure along the corresponding normal mode. Note that there are as many normal modes as degrees of freedom of the structure since we are not adding any additional constraint. These normal modes represent a new basis that gives more information about the preferred deformation of the structures than the translational degrees of freedom of the vertices. Note that there are 6 normal modes which represent the rigid body motion in 3D space, thus having zero frequency and zero energy. We omit these modes in this study.

In order to study the origin of the deformation of the normal modes, first we obtain the energy of these modes. Since we define the Lagrange equation in a closed system, i.e., no energy is explicitly dependent on time, the total energy E_{tot} of each mode is constant. From this constant energy we can obtain the elastic energy by considering the deformation at a specific time when the kinetic energy is zero (Appendix A). Note that we use a dynamic model only to obtain the normal modes, however we do not use the kinetic energy for this study. The elastic energy is then decomposed into its three components (hinge folding, face stretching and face bending energy). Then, each component is normalized with their respective stiffness obtaining $\tilde{E}_{hinge}$, $\tilde{E}_{stretch}$, and $\tilde{E}_{bend}$, respectively. All normalized components are added together to obtain a normalized total energy. Finally, we divide each normalized component by the total normalized energy to obtain the energy distribution for each normal mode.

3.2. Normal modes of prismatic structures

We obtain the normal modes and their corresponding energy distribution for two specific structures based on a cube and a truncated tetrahedron (Fig. 3.1a). We specifically select these structures since in the rigid origami model they have two distinct behaviors. The structure based on a cube can deform along 3 branches, while the structure based on a truncated tetrahedron cannot deform. Note that we approximate the elastic origami model to a thin wall origami behavior. For this we assume a stiffness regime, i.e., the relation of the spring stiffnesses in the model, that follows $k_h \ll k_b \ll k_s$.

In Fig. 3.1b we show a scatter plot of the normal modes on a ternary graph showing their energy distribution of the three types of allowed deformation for the selected structures. If a normal mode is localized at one of the corners of the plot, the energy of that mode has only one component. Note that some modes are degenerate, meaning they have the same energy distribution and value, and their deformation is symmetric. Importantly, the bottom left corner in Fig. 3.1b, i.e., the hinge corner, corresponds to normal modes that depend only on folding of the hinges. For example, the structure based on a cube has three modes at this corner (i in Fig. 3.1c and Movie 3.1). These normal modes are soft modes and have the same deformation as the branches in the rigid

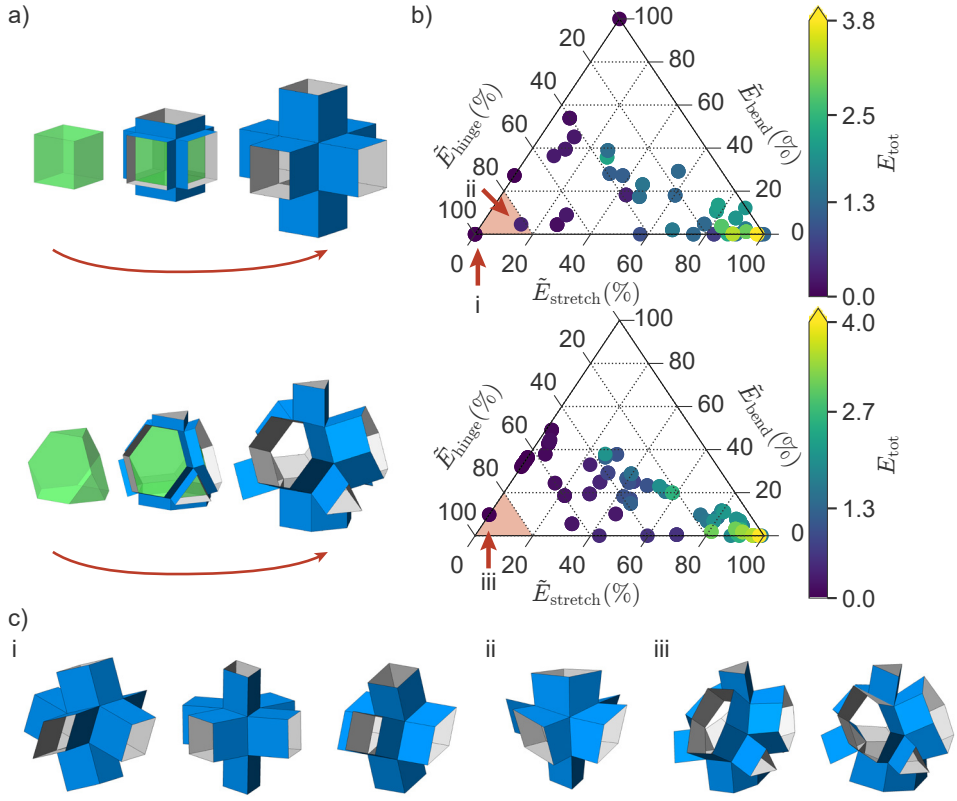

Figure 3.1 | a) Design of the prismatic structures based on polyhedra by extruding the faces (top: cube, bottom: truncated tetrahedron). b) Energy distribution of the normal modes these prismatic structures according to the elastic origami model in the stiffness regime where $k_h = 10^{-4}$, $k_b = 10^{-2}$, and $k_s = 10^{0}$. The colored area represents the hinge corner. c) Deformation of the soft (i) and pseudo soft (ii and iii) modes for the structures based on a cube and a truncated tetrahedron. The location of these modes is indicated in b) by an arrow.

origami model. Note that there is an additional normal mode close to this corner (ii in Fig. 3.1c and Movie 3.1), however this mode requires some face stretching and bending, thus is not considered a soft mode according to our definition.

Additionally, we observe modes that lie almost at the hinge corner of the plot. The energy of these modes is defined mostly (> 80%) by just folding of the hinges. Note that the use of 80% is arbitrary and can be adjusted to experiments. We call these modes, pseudo soft modes. The mode ii of the structure based on a cube is a pseudo soft mode, however the soft modes i have much lower energy since their deformation only has hinge folding. The structure based on a truncated tetrahedron has pseudo soft modes (iii in Fig. 3.1c and Movie 3.1). Moreover, we obtain the normal modes and their energy distribution for all other prismatic structures that are rigid under the rigid origami model (Fig. A.1). Interestingly, we notice that all of them have pseudo soft modes. Note that these pseudo soft modes are important since they describe the deformation of these rigid structures

with minimum face deformation, similar to branches in the rigid origami model. The soft and pseudo soft modes are likely to influence the folding behavior in experiments, since the hinge folding stiffness k_h has the lowest value for origami by definition, and therefore, they have always the lowest energy.

3.3. Stiffness dependency

The total energy of the modes depends highly on the selected stiffness regime. For the thin wall origami approximation, the closer a mode is to the lower right corner in Fig. 3.1b, the higher its total energy is since the edge stretching stiffness k_s is the highest. However, this approximation does not always hold and the stiffness regime might change depending on the experimental realization. For example, when producing origami at small scales [19], the thickness of the faces increases due to the fabrication limitations and thus the bending stiffness k_b might become similar or higher than the stretching stiffness k_s.

To illustrate how the stiffness regime can affect the total energy of the normal modes, we use a simpler structure based on a square (Fig. 3.2a). This structure is a building block of the prismatic structures, and has only 18 normal modes. Fig. 3.2b and c show the energy distribution of the normal modes with a stiffness regime $k_h \ll k_b \ll k_s$ and $k_h \ll k_s \ll k_b$, respectively. As expected, most of the normal modes change their total energy following the highest stiffness and without changing their energy distribution, i.e., their location in the graph. However, by comparing both plots, we observe that the energy distribution of two normal modes depends on the stiffness regime, thus changing their location between graphs. The two modes (i and ii) appear at a specific location in the first stiffness regime (Fig. 3.2b), while they appear in a different location (iii and iv) in the second regime (Fig. 3.2c). These modes behave differently between stiffness regimes since they show a different energy distribution and thus a different deformation (Fig. 3.2d and Movie 3.2). We also see these types of modes for other prismatic structures (Fig. A.2). This hints to a possible mode interaction that complicates the classification of the normal modes, e.g., pseudo soft modes might exist only for a specific stiffness regime.

3.4. Normal modes interactions

To understand what happens with these modes, we trace the normal modes between the two stiffness regimes. For this, we vary the face bending stiffness k_b in small steps while keeping the other stiffnesses constant ($k_h = 10^{-4}$ and $k_s = 10^{0}$). For each step we obtain the normal modes and compare their deformation to the previous step by determining their correlation coefficient [87]. This coefficient is a normalized covariance of the deformation, and measures the strength of the linear relationship between the two deformations. We use a build-in function in *NumPy* called *corrcoef* to calculate this coefficient. We identify the normal modes by matching each mode of a specific step with the mode with the highest correlation coefficient from the previous step. This matching allows us to keep track of the normal modes. Fig. 3.2e shows the dependency of the total

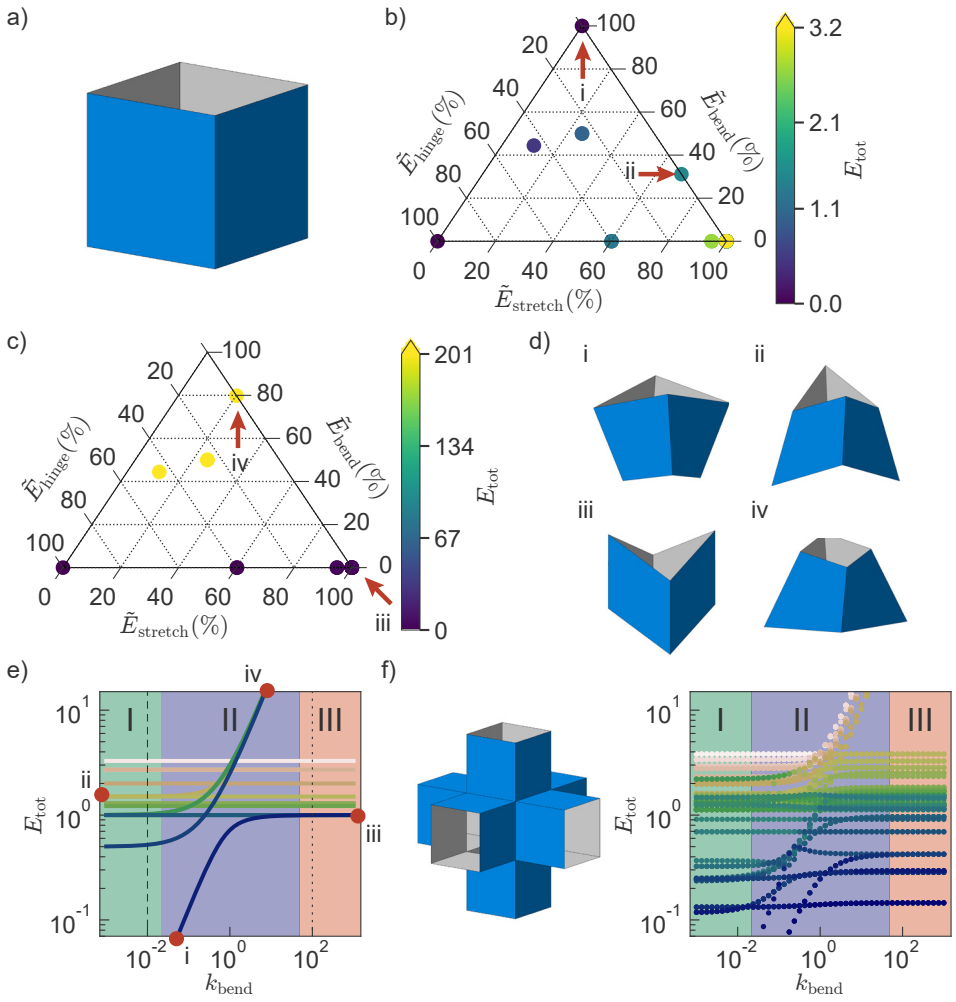

Figure 3.2 | a) Structure based on a square that is used as a building block for the prismatic structures. Energy distribution of the normal modes according to the elastic origami model in the stiffnesses regime $k_{\text{h}} = 10^{-4}$, $k_{\text{b}} = 10^{-2}$, $k_{\text{s}} = 10^{0}$ (b), and $k_{\text{h}} = 10^{-4}$, $k_{\text{s}} = 10^{-2}$, $k_{\text{b}} = 10^{0}$ (c). d) Deformation of special modes whose energy distribution depends on the stiffness regime (i and ii are indicated in b), iii and iv in c)). e) Total energy of the normal modes depending on the bend stiffness k_{bend}. Background colors represent three different stiffness regions. Dashed and dotted lines show the location of the normal modes of b) and c), respectively. Dots show the location of the corresponding mode. f) Total energy of the normal modes depending on the bend stiffness k_{bend} for a structure based on a cube.

energy of these normal modes on k_{b}. Note that we do not show the soft modes, since their energy is lower than 10^{-1} and they do not interact with any other mode. To explain the behavior of the normal modes, we define 3 regions in this graph, (I) $k_{\text{b}} \ll k_{\text{s}}$, (II) $k_{\text{b}} \approx k_{\text{s}}$, and (III) $k_{\text{b}} \gg k_{\text{s}}$.

To clarify the change of the normal modes deformation between stiffness regime, we

track the modes i and ii from region I to region III in Fig. 3.2e. We notice that these modes are the modes iii and iv, respectively, meaning that they lie on the same line in the graph. These two modes have different deformation and energy distribution from region I to III since they interact in region II. This interaction derives from the coupling of these modes [88, 89], due to the spatial configuration of the structure. This coupling induces a mixture of the modes, meaning that the deformation of mode iii and iv can be seen as a linear composition of the deformation of mode i and ii. This explains the change of their energy distribution between stiffness regimes since their deformation changes.

For this simple case, we only have one interaction of two modes, making it easy to track the normal modes between stiffness regimes. However, for complex structures with many modes, these interactions are more prominent. For example, for a structure based on a cube (Fig. 3.2f), we are not able to track the modes between regimes, since small changes on the stiffness regime in region II trigger larger changes on the deformation of the modes deriving in low correlation coefficients in this region. Note that this figure shows a scatter plot of the normal modes, where these are sorted in each step from lowest to highest energy. This means that the colors do not imply the same normal mode. Since the tracking of the modes is impossible, the description of the normal modes depends on the stiffness regime, and therefore we are obliged to adapt this description for each stiffness regime. This is especially difficult in region II, where the deformation of the modes highly depends on the stiffnesses. However, we want to have a general description of the normal modes that can be applied across different stiffness regimes, i.e, a description that is independent of the stiffness regime.

3.5. Deformation constraints

To have a description of the normal modes spanning through different stiffness regimes, we need to remove the mode interactions. To do this we constrain certain deformations, so the modes cannot interact. Typically, scientist constrain the face stretching since the face bending can be modeled as additional hinges on the diagonal of the faces [47]. With this constraint, some structures have enough degrees of freedom to find new folding pathways, such as the waterbomb and square twist origami pattern [25, 35]. Nevertheless, scientist have also constrained the face bending and only allowed face stretching, finding also new stable states [14, 52]. In this study, we constrain both deformations separately to see the effect they have on the behavior of the prismatic structures and compare them to the normal modes of the rigid and elastic models.

To constrain these deformations separately, we define two reduced models, the bend constraint model and the stretch constraint model. We use a set of equations that defines these constraints, and are incorporated in the Lagrangian by changing to generalized coordinates (Appendix A). These generalized coordinates transforms the eigenvalue problem to $\boldsymbol{K'}^{-1}\boldsymbol{M'}\boldsymbol{w} = \lambda\boldsymbol{w}$, where the eigenmode $\boldsymbol{w}$, the stiffness matrix $\boldsymbol{K'}$ and the mass matrix $\boldsymbol{M'}$ are defined in the generalized coordinates. We can transform them back to Cartesian coordinates with a transformation matrix T, e.g., $\boldsymbol{v} = \boldsymbol{T}^{-1}\boldsymbol{w}$, $\boldsymbol{K} = \boldsymbol{T}^{-1}\boldsymbol{K'}$, and $\boldsymbol{M} = \boldsymbol{T}^{-1}\boldsymbol{M'}$. This is useful since the transformed eigenmode $\boldsymbol{v}$ defines the mode deformation of the structure. Importantly, the components of the stiffness matrix $\boldsymbol{K}$ change. By constraining the stretching or bending of the structure, we remove the stiffness contri-

bution of such deformation, thus $\boldsymbol{K}$ will only depend on (k_h, k_b) or (k_h, k_s), respectively. This is particularly advantageous since we can reduce the parameters of our models to a single one, the ratio of the stiffnesses. So the bend constraint model depends only on $\kappa_s = k_h/k_s$, and the stretch constraint model on $\kappa_b = k_h/k_b$. Note that, this parameter becomes a tool for tuning the behavior of origami structures, but the total energy still depends on the absolute value of the stiffnesses.

3.6. Normal modes with constrained models

To see the effect of the constraints on the folding behavior of origami, we use the same structures as before, that are based on a cube and a truncated tetrahedron. For each structure we obtain the normal modes and their energy distribution with the two different reduced models. For each model we define $\kappa_b = 10^{-3}$ and $\kappa_s = 10^{-3}$, respectively with $k_h = 10^{-3}$, keeping a thin wall origami approximation. Note that the absolute value of the stiffnesses does not affect the energy distribution of the normal modes.

Fig. 3.3a and b shows a histogram of the energy distributions for the structures based on a cube and a truncated tetrahedron, respectively. Two aspects come forth in these graphs. First, the number of normal modes changes significantly depending on the reduced model. In the stretch constraint model, the number of normal modes, and therefore the number of degrees of freedom gets largely reduced. Note that, for other structures, like one based on a tetrahedron or a octahedron (Fig. A.3), the reduction of normal modes is such that they become rigid. For these structures, face bending does not add any degrees of freedom that allow the structure to deform.

On the contrary, in the bend constraint model, the number of degrees of freedom does not get largely reduced having still many possible deformations. For example, the structure based on a truncated tetrahedron has 138 normal modes in the elastic origami model, and 102 in the bend constraint model. This hints that the bend constraint model is closer to the elastic origami model, allowing deformation of the structures along many degrees of freedom, while the stretch constraint model is closer to the rigid origami model by having just a few degrees of freedom.

Second, while for a structure based on a cube the soft modes are not affected by the constraints of both reduced models (Fig. 3.3c and Movie 3.3), as expected, these constraints do affect the pseudo soft modes. With the stretch constraint model the structure based on a truncated tetrahedron has no pseudo soft modes. This also happens with the other structures which are also rigid under the rigid origami model (Fig. A.3). Nevertheless, with the bend constraint model for these structures, not only the pseudo soft modes exist, but the number of pseudo soft modes increases compared to elastic origami model (Fig. 3.3d, Movie 3.3, and Fig. A.3). To explain this we need to look at the modes that disappear from the elastic origami model to the bend constraint model. Some of these modes have hinge folding deformation that is still allowed in the reduced model. To integrate this deformation in the reduced model, some normal modes allow more hinge folding, becoming pseudo soft modes. Therefore, to maintain the pseudo soft modes with no mode interactions, it is sufficient to have the bend constraint model. The stretch constrain model becomes too restrictive for the structures that are rigid under the rigid origami model since it cannot capture the possible deformation of the pseudo

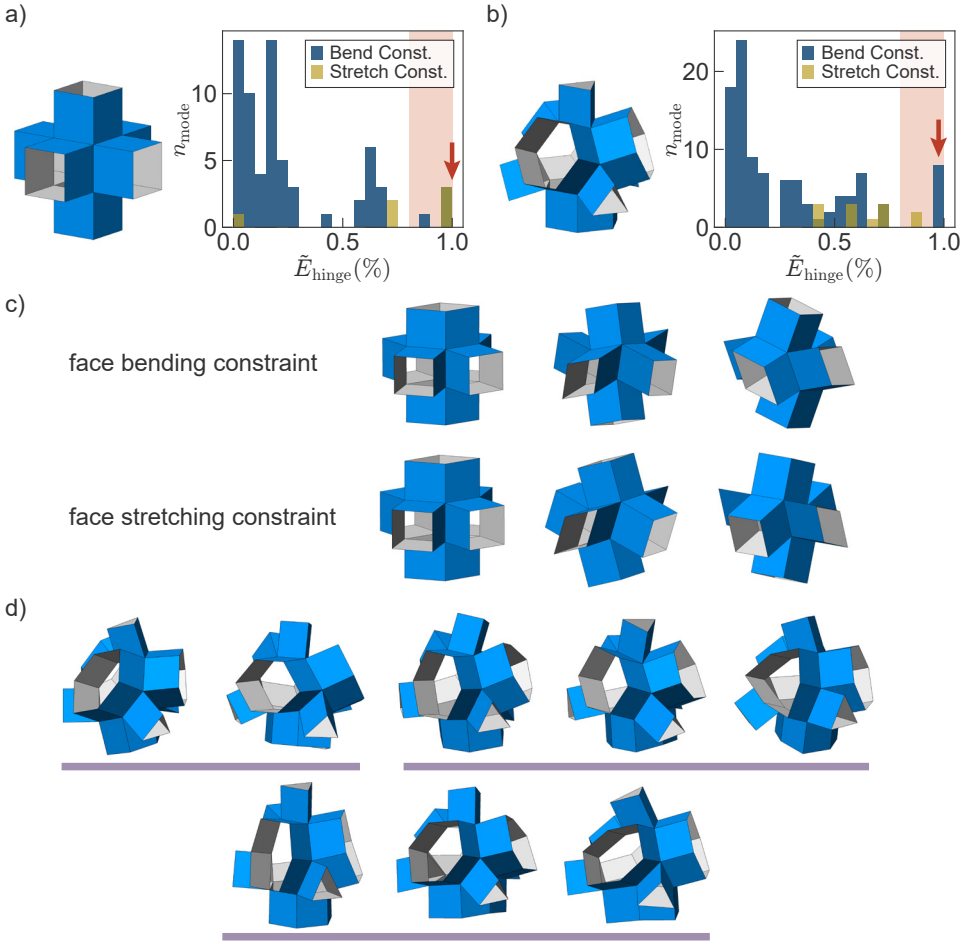

Figure 3.3 | Energy distribution of the normal modes assuming the reduced models, bend constraint model and stretch constraint model, for structures based on a) a cube and b) a truncated tetrahedron. The colored area shows where the pseud-hinge modes are located. c) Deformation of the soft modes of a structure based on a cube for the two different reduced models. d) Deformation of the pseudo soft modes of a structure based on a truncated tetrahedron in the bend constraint model. Modes that have the same energy are underlined.

soft modes.

3.7. Normal modes with imperfections

Until now, we have been studying perfect structures. However, when creating origami structures in real life, imperfections are impossible to avoid due to the fabrication procedures. For the rigid origami model small imperfections have large effects on these structures, such as hindering their foldability [79], increasing the structure's stiffness [83] or

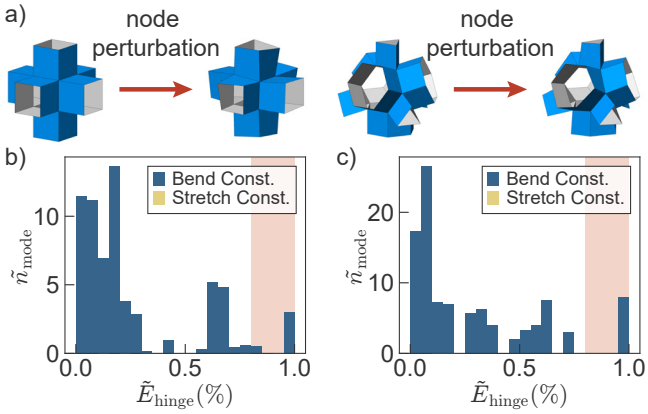

Figure 3.4 | a) Perturbation of the nodes in structures based on a cube and a truncated tetrahedron. Note that this perturbation is 5× magnified to be able to see it. b) and c) Energy distribution according to the reduced models of structures with imperfections based on a cube and a truncated tetrahedron, respectively. Note that the energy distributions of the modes without imperfections are shown in Fig. 3.3

modifying its folding pattern [84, 85]. On the contrary, in the elastic origami model the structure can typically compensate such imperfections with small deformation. To study the effect of small imperfections in the reduced origami models, i.e., bend constraint model and stretch constraint model, we apply random perturbations to the nodes of the structure. The perturbation is taken from a normal distribution with standard deviation of $0.01L$, where L is the length of an edge of the structure. This perturbation cannot be seen by the naked eye, but in Fig. 3.4a we show an example with a 5x magnified perturbation, i.e., normal distribution with standard deviation of $0.05L$. We then calculate the normal modes of the perturbed structure and their energy distribution. We repeat this simulation 100 times in order to obtain an average energy distribution of the normal modes.

Fig. 3.4b and c show the normalized histogram of the average energy distribution for a structure based on a cube and a truncated tetrahedron, respectively. Note that, the stretch constraint model does not result in any normal modes for these or any other structure (Fig. A.4), even if they have branches in the rigid origami model. In this reduced model, small imperfections of the structure lead to the complete loss of folding behavior, turning the structure rigid, despite that we allow for face deformation. On the contrary, in the bend constraint model, small imperfections do not affect considerably the folding behavior of the structures. The number of normal modes remains equal compared to a structure without imperfections, and the energy distribution qualitatively does not change. Moreover, the pseudo soft modes are not affected, since they already entail a small proportion of face deformation that can accommodate the imperfections. Note that the soft modes become pseudo soft modes since they rely on extreme symmetry of the structures that disappears with imperfections. Therefore, the bend constraint model describes the normal modes of a origami structure from a general perspective, without any effects from the imperfections, while the stretch constraint model fails to describe any deformation in structures with imperfections.

3.8. Discussion

In this work we obtain the kinematics of prismatic building blocks under the elastic origami model through the calculation of the normal modes. By decomposing the energy of these modes into its components, we show the appearance of soft and pseudo soft modes that resemble branches of the rigid origami model. We then test two constrained models to obtain a classification of normal modes across different stiffness regimes. We show that the model that constrains the face bending rises as a simpler model to describe elastic origami since it holds the many degrees of freedom from the elastic origami model, and imperfections do not affect the folding behavior characterized by this model.

We used a set of prismatic structures to illustrate the folding behavior with the reduced model, however we are confident that this model can be used with other origami-inspired metamaterials showing the same folding behavior along normal modes. We present this reduced model as a broad applicable tool to search for new folding behaviors. For example, since the soft and pseudo soft modes describe the most possible deformation of the structures, they give specific directions to scan the multi dimensional energy landscape in order to find new stable states. Furthermore, by obtaining the normal modes not only from an initial position, but from different states along these directions, we can obtain deformation pathways that require minimum energy. This can be used to create the new generation of reconfigurable metamaterials for a wide variety of applications such as reconfigurable acoustic wave guides [90], microelectronic mechanical systems [8] and energy storage devices [91].

4

Exploring multistability in prismatic metamaterials through local actuation

Abstract

Metamaterials are artificial materials that derive their unusual properties from their periodic architecture. Some metamaterials can deform their internal structure to switch between different properties. However, the precise actuation of these deformations remains a challenge, as these structures often exhibit non-linear mechanical behavior. We introduce a computational and experimental strategy to explore the folding energy of a range of 3D prismatic building blocks that exhibit adjustable multifunctionality. By applying local actuation patterns, we are able to explore and visualize their complex mechanical behavior. We find a vast and discrete set of mechanically stable configurations, that arise from local minima in their elastic energy. Additionally these building blocks can be assembled into metamaterials that exhibit similar multistability. The mechanical principles on which the multistable energy is based are scale-independent, making our designs candidates for, e.g., reconfigurable acoustic wave guides, microelectronic mechanical systems and energy storage systems.

Based on: Iniguez-Rabago, A., Li, Y. and Overvelde, J.T.B., *Exploring multistability in prismatic metamaterials through local actuation.* Nat. Commun. 10, 5577 (2019) under the following license:

In the search for materials with exotic properties, researchers have recently started to explore the design of their mesoscopic architecture [69]. These so-called metamaterials have properties that arise not only from their chemical composition, but rather from the interplay between stimuli and the material's periodic structure. Examples include auxetic behavior [92, 93], mechanical cloaking [70] and non-reciprocal response [67]. A challenging problem has been to design multifunctional materials, i.e., materials that can vary their properties. So far, this has been achieved by, e.g., taking inspiration from origami to create internal structures that can be reconfigured along a few degrees of freedom [50, 54, 94]. Finding the structure of such reconfigurable materials is not trivial since the number of degrees of freedom for a general origami design grows exponentially [30], and typically a general design approach [47] is needed to satisfy required conditions [48]. Once created, these materials exhibit highly anisotropic behavior, enabling the change of their properties by applying locally a range of stimuli including air pressure [55, 95], pre-stresses [94] and swelling [96]. However, the deformed state of these materials becomes dependent on these stimuli, and once they are removed the material will relax to the initial configuration.

A way to overcome this dependency is to use multistability [14, 25, 26, 28, 51, 97], i.e., two or more stable states that differ in configuration and are separated by significant energy barriers. Multistability has already been used to create auxetic [92, 98] and energy trapping metamaterials [99–101] as well as deployable [14, 102], morphing [103] or crawling [81] structures, however, most of these materials are assembled from 2D building blocks that can switch between only two stable states. A natural question to ask is whether 3D building blocks with more than two stable configurations exist and if they can be used to form multifunctional metamaterials.

As such, here we study a class of prismatic multistable 3D building blocks, that are based on polyhedra templates. These building blocks have previously been studied from an infinitesimal deformation and rigid origami model [54], however here we assume that these structures can undergo large rotations and deformations of the faces, making the energy of these structures highly non-linear and thus significantly more difficult to explore. To do so, we use the numerical method introduced in Chapter 2 to search for minima in the elastic energy that correspond to the stable states of the prismatic structures. In this model, we ignore any dynamic contribution since we stay in a static framework. While a complete description of all possible deformations and stable states is not possible due to the large number of degrees of freedom arising from the elastic description, our method was designed to closely mimic possible experimental implementations of locally actuated metamaterials previously studied for only one prismatic structure [55]. As a result, we are able to shine light on the highly multistable behavior that most of these building blocks exhibit. We start by introducing the design of the 3D building blocks and the details of our numerical model to simulate the structure's energy. We next validate our numerical approach with centimeter-scale prototypes. In order to gain insight in the problem, we then visualize the non-linear energy landscape of multiple prismatic building blocks by applying local actuation to two hinges. Based on these results, we develop a method to extract all possible unique actuation patterns, allowing us to efficiently scan through the energy landscape and find additional stable configurations. Finally, we show for a few multistable building blocks that they can be assembled to create multistable

metamaterials.

4.1. Design

The structures investigated here are constructed based on templates of space-filling arrays of polyhedra [104]. Each polyhedron in the array is used as a basis for a thin-walled building block, that is constructed by extruding the edges of the polyhedron in the direction normal to the corresponding face (Fig. 4.1). In the rigid origami model [105], i.e., the structure can only fold along predefined hinges, some of the building blocks cannot change shape (Fig. 4.1a-b), while others can be reconfigured along specific degrees of freedom (Fig. 4.1c). Interestingly, for all of these examples we found additional stable configurations that are spatially admissible, but that cannot be reached without temporarily deforming the rigid faces (Fig. 4.1). Under the assumption of rigid origami, these states correspond to minima in elastic energy that are separated by infinite high barriers, i.e., they are topologically isolated [27]. By allowing the faces to stretch and/or bend, i.e., elastic origami [26], we lower the energy barrier such that moving between local minima becomes kinetically admissible. Note that in the elastic origami model the structure has many degrees of freedom, however, some deformations require significantly less energy than others corresponding to the degrees of freedom obtained in the rigid origami model. We refer to these deformations as soft modes instead of degrees of freedom. While for some simple origami patterns the energy of the system can be computed analytically [23, 25, 97], already a generic 4-vertex pattern becomes nearly impossible to decipher [51]. The 3D prismatic structures considered in this study are constructed from non-flat 6-vertex, 8-vertex, and 10-vertex, and therefore an efficient numerical technique is needed to explore the energy landscape and discover new stable states.

To model the thin-walled prismatic structures as shown in Fig. 4.1, we define the elastic energy of the prismatic structures using linear springs similar to previous work [25, 26, 56] (Section 2.2). This energy has zero value at the extruded position. Each hinge is modeled as a torsional spring with stiffness k_h, in which contact is taken into account by constraining the fold angle between $-\pi \leq \theta \leq \pi$. We account for in-plane stretching of the faces by applying springs with stiffness k_s along the edges and the diagonals [56]. Bending of the faces is prevented using a set of constraints (Section 2.5). As such, the relation between face deformation and hinge bending is specified by the ratio $\kappa = k_h / k_s$. Note that typically, when simulating origami, deformation of the faces is modeled using bending instead of stretching [25]. However, to reduce the computational requirement, the observed deformation in our prototypes can be approximated using only in-plane stretching that is the result of the stretchability and flexibility of the hinges as observed in experiments [14]. Additionally, this simplifies the problem by reducing the number of parameters in the simulations, i.e., bending stiffness of the faces is not considered.

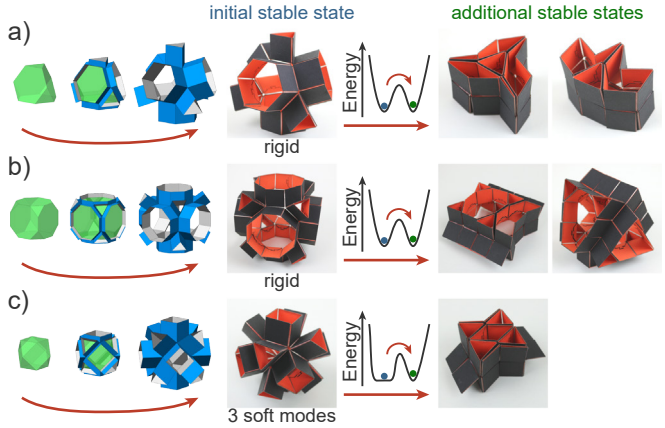

Figure 4.1 | The prismatic structures can be designed by extruding the edges of a convex polyhedron perpendicular to the faces. The multistable examples shown here are based on a) a truncated tetrahedron, b) a truncated cube and c) a cuboctahedron. The additional stable states can only be reached by going over a finite energy barrier resulting from deformation of the faces of the structure. The prototypes have square faces of 24 mm made from cardboard (0.4 mm thick) and connected through hinges made from double-sided tape [54].

4.2. Compression experiments

We first verify the numerical model with compression experiments. We performed experiments on a prismatic structure based on a cuboctahedron, as the shape of two of the stable states (Fig. 4.1b) is compatible with the compression applied along a specific axis (Movie 4.1 in Appendix D). Note that this compression does not undergo any deformation along the three soft modes that this structure exhibits, therefore implying deformation of the faces. To fabricate the prototype, we built each face from two 3D-printed (Ultimaker 3) lego-like building blocks (0.5 mm thick polylactide, PLA), between which a thin lasercut sheet (50 ţm thick Mylar) was manually clamped to connect the faces and form the flexible hinges. To compress the structure between two stable states we used a material test machine (Instron 5965L9510), in which we applied a cyclic displacement with a magnitude of $u_{\max} = \sqrt{2}L$. Fig. 4.2a shows the average force-displacement response of the last five compression cycles, in which the line thickness indicates the standard deviation.

The results show an initial increase in force (F) due to the elastic deformation of the structure. At $u/u_{\max} \approx 0.6$ the response reaches a plateau, after which instabilities of the structure start to appear indicated by sudden drops in the reaction force. Importantly, the force reaches negative values after the instability at $u/u_{\max} \approx 0.75$, implying that the structure has passed an energy barrier reaching a different stable state. When slowly releasing the compression, the structure follows a different path as can be seen from the hysteresis. Simulations of the same loading conditions using our numerical model are shown in Fig. 4.2b (Section B.2). While some differences exist between simulations and experiments, the similarity is striking. Both the experimental and numerical response are characterized by the same instabilities and deformation sequences (see

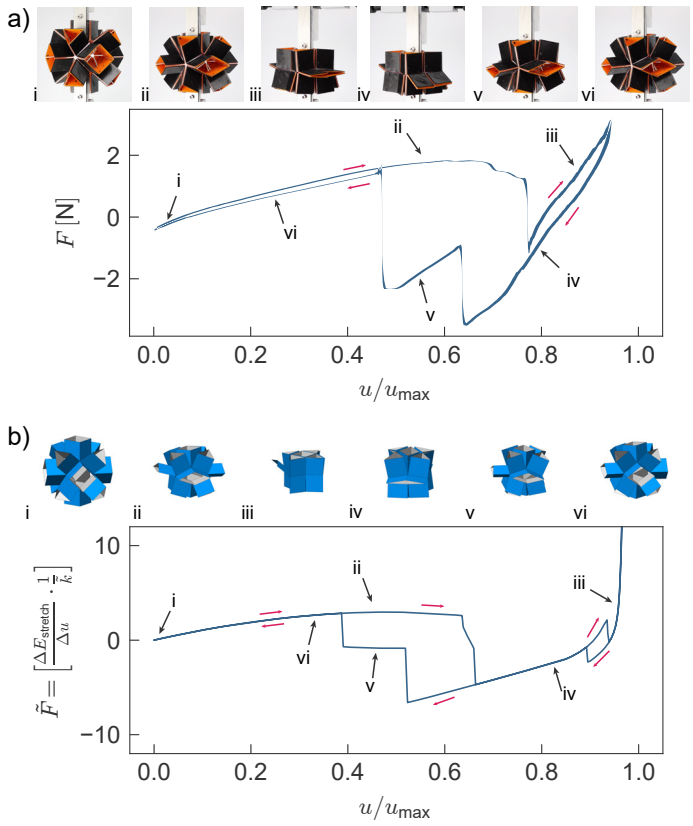

Figure 4.2 | a) Average force-displacement response obtained by cyclic loading (five times) of an experimental prototype of a prismatic structure based on a cuboctahedron made from 3D printed faces (2×0.5 mm thick PLA) connected by flexible Mylar hinges (50 ţm thick). The standard deviation is indicated by the thickness of the line. The force changes sign when an energy barrier is crossed, indicating that the structure deforms from one stable state to another. b) Normalized force-displacement response obtained with our numerical method for the same structure. The behavior of both the experiments and the simulations are strikingly similar, both showing one instability when compressing the structure and two when returning to the initial configuration. Note that a small hysteresis loop observed in simulations at the end of the compression is not captured in experiments possibly due to a small misalignment when clamping the structure or small fabrication errors of the prototype.

insets in Fig. 4.2). Moreover, additional simulations (Fig. B.1) reveal that the observed response is mainly due to stretching of the faces and not bending of the hinges, since the stiffness ratio κ can be increased by at least one order of magnitude (from $\kappa = 10^{-4}$ to $\kappa = 10^{-3}$) without seeing any major effect on the response. These experiments show that the simulations can qualitatively predict the behavior of the structure. Therefore, our numerical models can be used to find stable states for the prismatic geometries.

4.3. Applying local actuation

To gain insight into the non-linear stability of these structures when applying local actuation, we next visualize a 2D projection of the energy landscape that can be obtained by actuating hinge-pairs. The actuation is achieved in our simulations by applying torques to the specific hinges, forcing them towards a target angle. Fig. 4.3a shows the energy of a prismatic structure based on a triangular prism, where we first deform the structure by actuating hinge b to θ_b, after which we actuate hinge a to θ_a. The energy is normalized by the maximum folding of the hinges and stretching of the faces (Section B.1). Interestingly, for $\theta_a + \theta_b < \pi$ deformation is dominated by folding of the hinges, indicating that the structure is rigidly foldable, i.e., deforms along one of the two soft modes. However, for $\theta_a + \theta_b > \pi$ the faces of the structure start to deform, leading to a dramatic increase in the elastic energy. For larger deformations the projection of the elastic energy becomes discontinuous, indicated by sudden drops, such that the structure undergoes instabilities during loading.

After deforming the structure, we release both torques and let the structure relax to a local energy minimum (Movie 4.2 in Appendix D). If the configuration after relaxation is different than the initial state, we have found a new stable state. The state diagram in Fig. 4.3b shows that for the structure based on a triangular prism, all initially deformed states converge to two stable states with $(\theta_a, \theta_b) = (2/3\pi, 2/3\pi)$ and $(\pi, 0)$ indicated by the star symbols in Fig 4.3b. Repeating this analysis for all other hinge-pairs reveals the existence of at least three stable configurations (Fig. B.3).

Similarly, we can apply this analysis to different prismatic structures, for example one based on a truncated tetrahedron (Fig. 4.3c-d). This structure does not exhibit any soft modes in its initial configuration, as expected from the initial experiments (Fig. 4.1) and previous numerical studies [54]. Nevertheless, we find several stable states. Already when actuating one hinge-pair, the simulations reveal a highly complex energy landscape with pathways that lead to 16 stable states. Some of these are related by rotational or mirror symmetries. In order to consider these symmetries we create a clustering method based on the values of the fold angles of all the hinges in the stable state to find the unique stable states (Section B.4). Following this method, we only obtain eight unique stable states. It is interesting to note that $(\theta_a, \theta_b) = (0, \pi)$ (Fig. 4.3d) describes three different stable configurations. This is a clear indication that we are looking at a 2D projection of a higher dimensional energy landscape, meaning that by changing the order of loading (Fig. B.4), the final deformed shape of the structures varies. It is important to emphasize that the possible stables states that we can reach with the local actuation depend on the initial state indicating a path-dependency behavior. Finally, by analyzing all other hinge-pairs (Fig. B.4), we found a total of 12 unique stable states.

4.4. Reducing the search space

Selecting hinge-pairs to scan through the energy landscape is a successful method to find energy minima, however precise local actuation applied to multiple hinges is difficult to achieve in experiments [55]. Therefore, we need a more realistic approach to search for additional states that can be achieved in experiments. To do so, we limit the

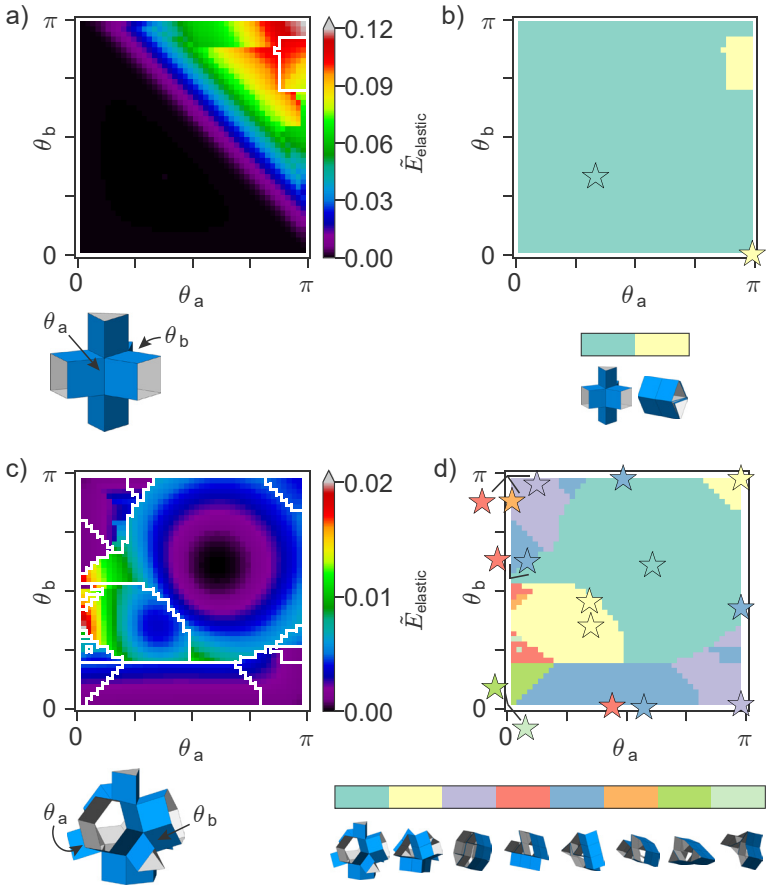

Figure 4.3 | These landscapes and states diagrams were obtained by running multiple simulations with different loads applied to two hinges. The studied prismatic structures are based on a) a triangular prism and c) a truncated tetrahedron. Here, we fold the structures in two steps: first we fold hinge θ_b, after which we fold hinge θ_a while keeping θ_b fixed. We record the elastic energy of the final state, and repeat this process for all possible combination of angles. The results are then presented as a 2D projection of the energy landscape. The corresponding state diagrams that are shown in b) and d), which are obtained by relaxing the prismatic structure from the folded configurations. The star symbols indicate the values of the fold angles θ_a and θ_b in the final configuration.

actuation to either off ($\theta = 0$) or on ($\theta = \pi$). This enables us to explore a larger range of hinge combinations to which local actuation is applied, and broadens our search for other stable configurations. However, before doing so, we first describe a method to reduce the search space in order to significantly reduce the computational needs.

We start by deriving the number of hinge combinations that can be actuated. For these combinations we consider all hinges of the structure, because by definition deformation of the structure requires energy, e.g., actuation, regardless whether the structure exhibits soft modes or not. Each prismatic structure is composed of two hinge types: internal and external. The internal hinges correspond to the edges of the polyhedron that

are used as a template, while the external hinges arise from the extrusion process. For example, a prismatic structure based on a tetrahedron has $n_{\text{int}} = 6$ internal hinges and $n_{\text{ext}} = 2n_{\text{int}} = 12$ external hinges. If we select one of these hinges for actuation, there are a total of $\eta_1 = n_{\text{int}} + n_{\text{ext}} = n_{\text{tot}} = 18$ different possibilities. When selecting two hinges, there are a total of $\eta_2 = n_{\text{tot}}!/(2!(n_{\text{tot}}-2)!) = 153$ combinations that we can make. In general, we can write for a selection of s actuated hinges $\eta_s = (n_{\text{tot}})!/(s!(n_{\text{tot}} - s)!)$, leading to a total number of actuation combinations equal to $\eta_{\text{tot}} = 2^{n_{\text{tot}}}$. These combinations grow exponentially with the number of edges of the prismatic structure (Fig. B.5). This makes it nearly impossible to run all different actuations for prismatic structures based on larger polyhedra, such as a cuboctahedron ($n_{\text{int}} = 24$) that has more than 10^{21} combinations.

By focusing only on the internal hinges of the prismatic structures (n_{int}), we reduce the number of combinations η_{int} to $2^{2n_{\text{int}}}$. Note that, e.g., for a cuboctahedron template this is approximately a reduction of 14 orders of magnitude (Fig. B.5). However, we still need to reduce η further to be able to efficiently scan the energy landscape. We therefore exploit the symmetries of the prismatic structures to remove the combinations of hinges that can be rotated or mirrored leading to exactly the same actuation patterns. To find symmetric actuation patterns, we first convert the polyhedron into a directed graph, mapping all the internal hinges to nodes on the graph. Depending on the two faces of the original polyhedron that are connected by the hinge, we give each corresponding node in the graph a specific type. For example, a hexagonal prism has the types triangle-square and square-square, while a tetrahedron only has the type triangle-triangle. We then construct the graph by connecting a directed line between two nodes if both hinges share one vertex and the internal polyhedron can rotate clockwise to the normal of the face that both hinges share. Next, we determine the minimum distance matrix between nodes [106], in which we keep track of the node type encountered when traveling along the shortest path. We extract all principal sub-matrices from the distance matrix and compare their eigenvalues and vectors to identify and remove symmetric loading cases (Section B.5). Using this method we can further reduce the number of hinge combinations (η_{sym}) by approximately two orders of magnitude (Fig. B.5).

4.5. Applying actuation patterns to find stable states

We next use these unique hinge combinations to apply discrete, i.e., on/off, actuation to the prismatic structures in order to find their stable states. As before, for each load case we first apply a torque to the corresponding hinges, after which we release the torque and let the structure relax to equilibrium. We then follow a clustering method to find the unique stable states (Section B.4). Additionally, we characterize the stability of these unique stable states by stepwise increasing the stiffness of the hinges by changing κ in our numerical model, pushing the structure back to its original undeformed state. We record the last value (κ_{max}) for which the prismatic structure remains in the stable configuration.

In Fig. 4.4a we show the results for the prismatic geometry based on a truncated tetrahedron, in which we plot the maximum value of the hinge stiffness, κ_{max}, against the

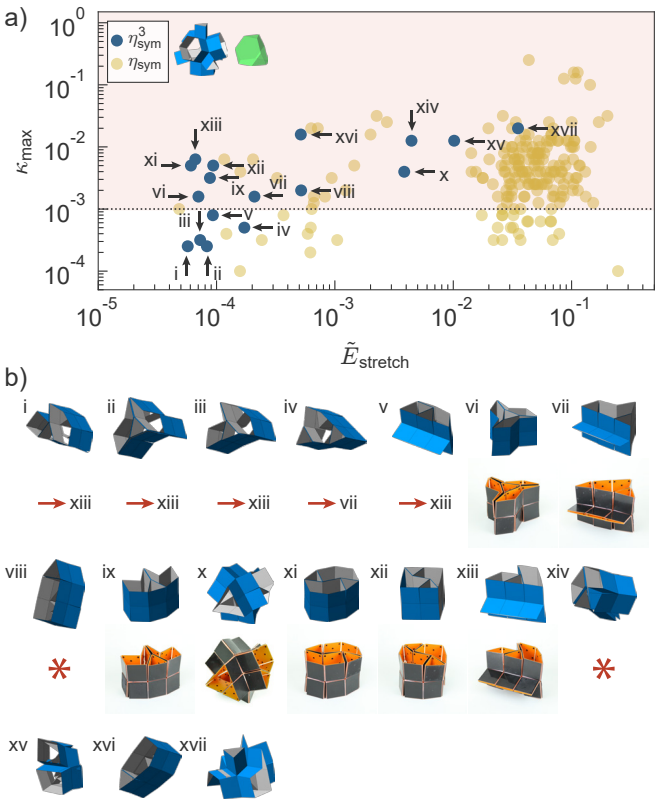

Figure 4.4 | The normalized stretch energy ($\tilde{E}_{stretch}$) and maximum stiffness ratio (κ_{max}) were obtained with simulations for the unique stable states of a prismatic structure based on a) a truncated tetrahedron and c) a cube. Blue dots indicate stable states found by actuation of up to 3 hinges simultaneously, while the yellow dots indicate all other stable states found by actuating more than 3 hinges. The pink and purple colors indicate regions with stable states that were achieved in experiments. b) A selection of the stable states of the structures based on a truncated tetrahedron is compared to experiments using a prototype with 3D printed faces and Mylar hinges. d) The stable states of the structures based on a cube cannot be obtained with prototypes made with Mylar hinges. Instead, more stretchable silicon hinges are used to obtain the stable states. The arrows indicate that the state is not stable in experiments, but relaxes to a different stable state. The single asterisk (*) indicates that the stable state could not be achieved in experiments due to a limited maximum stretch, while the double asterisk (**) indicates that the state cannot be achieved due to non-adjacent face crossing.

normalized stretch energy, $\tilde{E}_{stretch}$, for all the stable states that we found. While we previously found 12 stable states for this structure when actuating only hinge-pairs (Fig. 4.3c-d), by running all the unique hinge combinations (η_{sym}) we find a total of 213 stable states (where we already removed the duplicate and symmetric stable states). To verify these results, we performed experiments on a prototype made with the same fabrication method discussed previously (Fig. 4.4b). We tried to obtain the 17 states that can be reached by actuating up to 3 hinges simultaneously (η^3_{sym}). While seven states can be found directly, we observe two important differences between simulations and experiments. First, the stable states (i-v) characterized by $\kappa_{max} < 10^{-3}$ cannot maintain

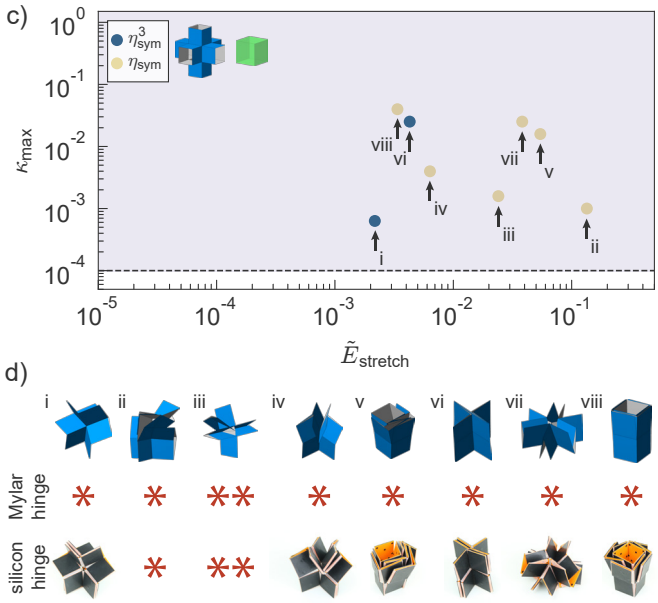

Figure 4.4 | (continued) The normalized stretch energy ($\tilde{E}_{stretch}$) and maximum stiffness ratio (κ_{max}) were obtained with simulations for the unique stable states of a prismatic structure based on a) a truncated tetrahedron and c) a cube. Blue dots indicate stable states found by actuation of up to 3 hinges simultaneously, while the yellow dots indicate all other stable states found by actuating more than 3 hinges. The pink and purple colors indicate regions with stable states that were achieved in experiments. b) A selection of the stable states of the structures based on a truncated tetrahedron is compared to experiments using a prototype with 3D printed faces and Mylar hinges. d) The stable states of the structures based on a cube cannot be obtained with prototypes made with Mylar hinges. Instead, more stretchable silicon hinges are used to obtain the stable states. The arrows indicate that the state is not stable in experiments, but relaxes to a different stable state. The single asterisk (*) indicates that the stable state could not be achieved in experiments due to a limited maximum stretch, while the double asterisk (**) indicates that the state cannot be achieved due to non-adjacent face crossing.

their stable configuration after releasing the actuation, and instead relax to states vii and xi (Movie 4.3 in Appendix D). We deduce from this observation that the value of κ in our experiments is equal to $\kappa \approx 10^{-3}$ (dotted line in Fig. 4.4a). Second, the stable states viii and xiv-xvii cannot be reached in experiments due to a limitation of the maximum stretch that the hinges of the prototypes can undergo. This difference is expected, as these constraints have not been taken into account in the simulations to maximize the search space.

To highlight the influence of the maximum stretch that we observe in experiments, we also performed experiments on a prismatic geometry based on a cube. While we find a total of eight stable states in our simulations (Fig. 4.4c), we were not able to reach any of these configurations with the current fabrication method. However, replacing the Mylar hinges with stretchable elastomeric hinges (0.5 mm silicon rubber) enabled us to overcome higher stretch energy barriers, such that we were able to find six of the stable states in experiments. Note that we were still not able to reach two of the stable

states. The stretch to obtain state ii is still larger than the capabilities of our prototype, while state iii has non-adjacent faces crossing that are not accounted for in our numerical model. Furthermore, we find that the elastomeric hinges result in a lower κ in the prototype, such that we were able to achieve stable states with $\kappa_{\max} < 10^{-3}$.

Finally, we applied the same analysis to the other 16 prismatic structures based on regular polyhedra that either have up to $n_{\text{int}} = 30$, or that can be used to construct uniform space-filling arrays [54]. Note that for polyhedra with $n_{\text{int}} > 18$ we were still not able to run all possible unique hinge combinations, and have limited ourselves to combinations of up to three hinges, i.e., η^3_{sym} (Fig. B.5). The number of stable states for the studied structures ranges from 2 to 418, as reported in Fig. B.6. Furthermore, we show some of the possible stable states that we can get from two different structures based on a truncated cube and a rhombicuboctahedron in Fig. B.7.

4.6. Multistable metamaterials

We have shown that by local actuation we are able to effectively explore the non-linear energy landscape of prismatic structures and find additional minima. We next show that our method can also be applied to find stable states in prismatic metamaterials assembled from these building blocks, by using periodic boundary conditions (Section 2.5). Note that periodic boundary conditions introduce additional constraints that considerable limit the stable states that can be achieved, and has a huge effect on the non-linear response of the material. In fact, many of the asymmetric stable states that we found for the unit cells can no longer be achieved in the materials. Therefore, the challenge here is to design materials that are capable of being mechanically stable in additional states. To perform a first exploration, we focus on cubic arrays that can be constructed from a single prismatic structure. We only consider 11 of the polyhedra that were previously found to be multistable, which results in a total of 15 materials (Fig. B.8). In order to search for stable states and to limit the number of actuation patterns that have to be applied, we apply the same actuation patterns to the material that previously resulted in stable configuration for the prismatic structure used as a unit cell.

We find that most (11) of the materials show additional stable states (Fig. B.8). In Fig. 4.5a-c and Movie 4.4 in Appendix D we show three of these multistable materials and some of their stable states with unit cells based on a cuboctahedron, a rhombicuboctahedron and a truncated cuboctahedron. Note that the energy of the metamaterial's stable states do not have to be equal to the prismatic building blocks. This can be seen for example from the stretch energy of the stable state of the unit cell of a cuboctahedron in Fig. 4.5d, which have shifted for the periodic arrangements.

To validate these findings, we fabricated a material assembly based on a cuboctahedron, that contains $2 \times 2 \times 2$ building blocks. As expected, we are only able to achieve one of the stable states (Fig. 4.5e), since states *ii* and *iii* lie below the $\kappa_{\max} \approx 10^{-3}$ threshold as previously predicted. To verify this, we also fabricated a second sample with thicker Mylar sheets of 125 μm, and we found that this metamaterial does not exhibit any stable states (Movie 4.5 in Appendix D).

While here we have limited our analysis to periodic boundary conditions applied to the unit cells, similar as in rigid origami [54], stable states can appear on the edges and

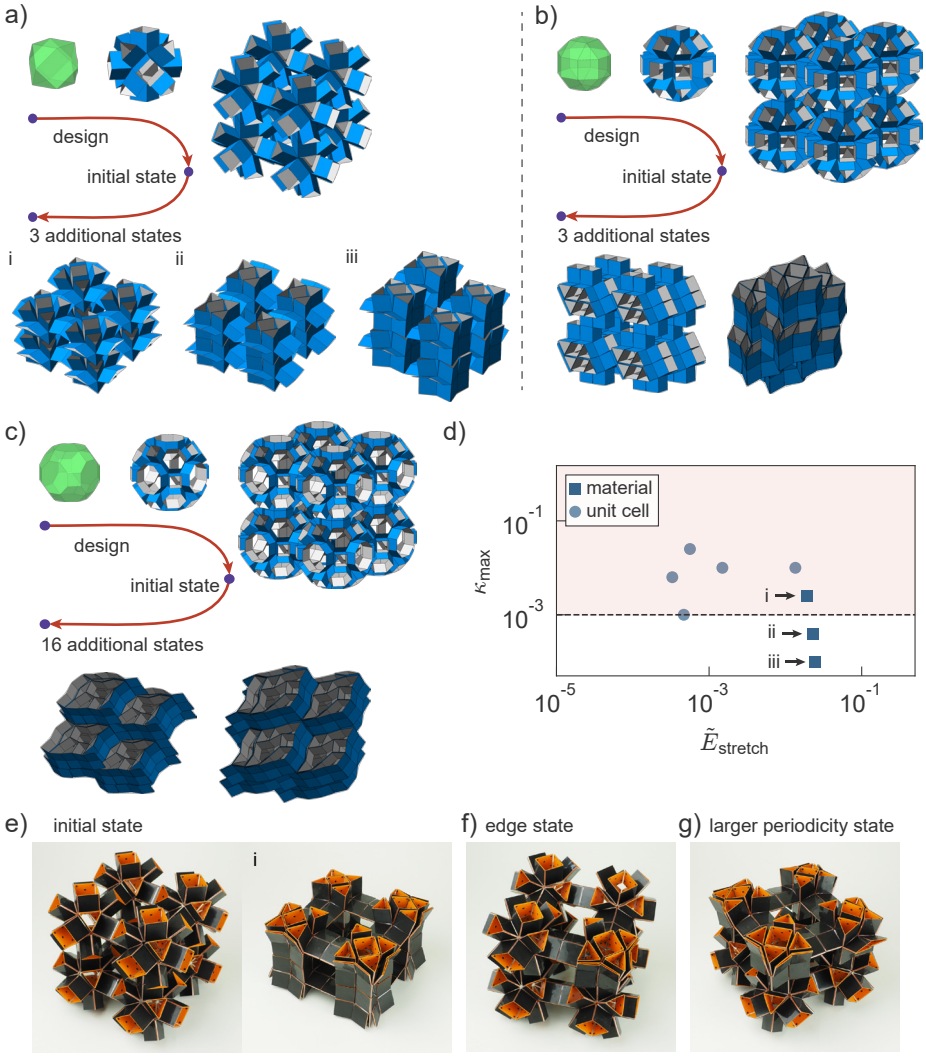

Figure 4.5 | The simulated metamaterials are based on cubic arrays of prismatic structures based on a) a cuboctahedron, b) a rhombicuboctahedron and c) a truncated cuboctahedron. d) Normalized stretch energy ($\tilde{E}_{stretch}$) and maximum stiffness ratio (κ_{max}) for the unit cell and the metamaterial based on a cuboctahedron. e) One of the stable states of the prismatic structure based on a cuboctahedron found in simulations can also be achieved in a prototype of the metamaterial made with 50 µm thick Mylar hinges. Additionally, we find f) edge and corner states and g) stable states with periodicity larger than a single unit cell not covered by our simulations.

corners of the materials. This is clearly demonstrated in Fig. 4.5f showing an edge state. We are also able to observe additional stable states with wavelength longer than the unit cells (Fig. 4.5g). In order to capture these in our model, larger unit cells would have to be considered. Therefore, additional studies have to be performed to continue exploration

of the rich energy landscape, including many other arrays that can be constructed.

4.7. Discussion

In summary, we have introduced a computational strategy to visualize and efficiently explore the complex energy landscape of 3D prismatic structures. We revealed the vast multistability of these structures, and despite that our numerical approach only explores part of the configuration space, by basing our method on local actuation we were able to find stable states that can be achieved experimentally. Additionally, by assembling these prismatic structures, we find multistable metamaterials that can reconfigure their architecture and therefore tune their properties. Importantly, these materials do not require energy to maintain their stable configurations, and will be robust to external variations as significant energy barriers have to be overcome to alter their structure. Moreover, by varying the relation between hinge and face stiffness, the stability of states can be tuned [14, 99, 107]. We believe that our local actuation strategy can also be applied to other origami-inspired metamaterials.

While we have only validated our experiments at the centimeter-scale using relatively simple fabrication techniques, the mechanical stability of our systems is theoretically scale-independent. However, fabricating such intricate structures at the micro/nano-scale is not trivial. More advanced 3D fabrication techniques such as two-photon lithography [108] or stereolithography [109] could lead this innovation. Additionally, scaling of these structures will introduce environmental influences such as capillary effects. It is not known how such forces influence the multistability of our structures, and additional research is required to explore this direction. Moreover, instead of manually deforming the structure, they can be made responsive by applying local actuation to the hinges. For our prototypes, this can be achieved by applying pneumatic pouches to some of the hinges [55]. As an example, already by discrete actuation of two pouches applied to the prismatic structure based on a truncated tetrahedron, we were able to achieve four of the stable states (Movie 4.6 in Appendix D). Similar strategies could be applied to actuate our designs at smaller length-scales, using, e.g., localized swelling of hydrogels for actuation. However, individually addressable local actuation patterns become difficult to apply at small scales and therefore a particular interesting future direction is the application of global stimuli to trigger the multistable behavior, e.g., heat or pH variations. Global stimuli can potentially lead to different folding behavior for a single structure by incorporating multiple materials into the design that each respond differently to changes in their environment or to different loading rates. Therefore, we believe that these prismatic multistable materials could lead to the next generation of multifunctional metamaterials that can be applied as, for example, reconfigurable acoustic wave guides [90], microelectronic mechanical systems [8] and energy storage devices [91].

5

From rigid to amorphous folding behavior in origami with bistable hinges

Abstract

The folding behavior of origami-inspired metamaterials is often described by linear rotational springs and rigid faces. However, other folding modes appear when assuming elastic faces, specially in combination with more complex geometries, leading to the emergence of multiple stable states. Here, we explore the use of non-linear material behavior implemented by assuming bistable hinges instead. By drawing a similitude to atomic crystals, we are able to classify the complex folding behavior that non-linear origami metamaterials undergo, where we identify transitions from rigid to elastic to amorphous behavior upon increasing strength of the bistability. As a result, our study gives a better understanding and provides a tool to adapt the multistability to metamaterials for future applications.

Based on: Iniguez-Rabago, A., Overvelde, J.T.B., *From rigid to amorphous folding behavior in origami-inspired metamaterials with bistable hinges.* PRL. (In review)

The ancient art of origami is often used as inspiration for mechanisms that allow a sheet to transform into complex 3D shapes [110]. These mechanisms are interesting for the design of morphing structures with a wide range of applications [111, 112] spanning from heart stents [113] and intraocular implants [114] to airbags [115] and solar panel arrays for satellites [45]. The underlying foldable origami patterns are typically described by a set of rigid faces connected by linear or zero-stiffness rotational springs, i.e., rigid origami model, and their folding behavior originates from the arrangement of the hinges. In this model, deformations are only allowed by folding a group of hinges through a limited number of pathways, i.e., branches. Following such approach, origami structures can be designed to become flat foldable [116, 117], self-folding [46, 49, 82], pluripotent [42] or reconfigurable [54]. Nonetheless, if the hinges are not assigned with a mountain-valley configuration, folding an origami pattern from a flat state to a specific 3D shape is not straightforward as multiple branches meet at this state [17, 30].

When no longer assuming perfect rigidity of the faces, i.e., faces can stretch or bend, additional degrees of freedom appear that could guide the folding behavior of the flat structures. Such description, referred to as elastic origami model, creates soft modes along the branches [52], while also supporting deformations outside of the soft modes. Moreover, reducing the constraints on the deformations opens up more folding pathways, allowing the sheets to reach multiple energy minima, i.e., multistability, that were hidden in the fully rigid origami model [26, 27]. Interestingly, these complex energy landscapes originate from geometrical features and have been studied for various origami structures based on prismatic building blocks [52], the square twist pattern [26], the Miura-ori pattern [50], and the hypar [71], among others [27–29]. Furthermore, springs have been added to already known origami patterns to add non-linear behavior such as bistability [118].

Here we introduce multistability in elastic origami by using bistable hinges. To study the interactions between these non-linear hinges and their effect on the folding behavior of initially flat sheets, we consider relatively simple double-symmetric 4-vertex origami. This design has previously been described in the rigid origami model [51, 77] and can be used as a first exploration to study how non-linearity can select certain stable pathways and states over others. In particular, by varying the strength of the bistability we probe the potential behavior of the sheets in a static framework, where we employ analysis methods used for 2D atomic crystal lattices to identify several regimes in their behavior, and the corresponding limitations.

5

5.1. Bistable origami hinges

Each origami array can be represented by a set of hinges. To achieve non-linear behavior, each hinge is represented as a rotational spring characterized by a symmetric double-well potential energy E_h following

$$E_\mathrm{h} = k_\mathrm{h} \frac{(\theta^2 - \Theta^2)^2}{(\Theta)^4}, \tag{5.1}$$

in which θ is the fold angle. We define the energy to be zero at the rest angles Θ and $-\Theta$, with an energy barrier of k_h (Fig. 5.1a), making the hinge bistable. Note that the hinge

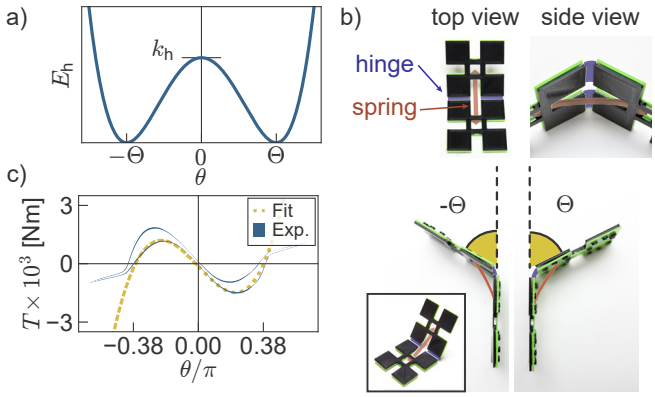

Figure 5.1 | a) Energy of the bistable hinge modeled as a symmetric double-well potential. b) Experimental realization of a bistable hinge made by connecting two rigid faces (37 × 37 × 2.5 mm PLA) with an elastic hinge (0.5 mm thick and 4 mm wide silicon) and a pre-stretched spring (t_{spr} thick and l_{spr} long silicon) showing the stable states. c) Relation between the measured average torque T and hinge angle θ obtained by cyclic loading (five times) of a hinge with $t_{spr} = 0.5$ mm and $l_{spr}/l_{flat} = 0.82$, fitted by our model. The standard deviation in experiments is indicated by the thickness of the line.

is at the top of the energy barrier when placed in its flat state, and has equal probability of folding either way. Here the bistability is embedded in the hinge, thus even a single hinge presents it, in contrast to previous research where the bistability derives from the interaction between hinges [71].

Experimentally, we achieved such bistability by connecting two rigid faces with an elastic hinge [52] and a pre-stretched spring (Fig. 5.1b and Appendix C.1). We varied the rest length l_{spr} and thickness t_{spr} of this spring to change the bistable behavior of the hinge, and measured the relation between torque and fold angle using a rotational test machine (Appendix C.1). Fig. 5.1c shows the average response of a hinge with $t_{spr} = 0.5$ mm and $l_{spr}/l_{flat} = 0.82$, where $l_{flat} = 34$ mm is the spring length when the fold angle $\theta = 0$. By fitting this response with our bistable model using $T = dE_h/d\theta$ (Appendix C.1), we obtain the rest angle $\Theta = 0.38\pi$ and the height of the energy barrier $k_h = 1.03 \times 10^{-3}$. We also apply this fit to a range of parameters (Fig. C.6).

5.2. Combining hinges into a single vertex

To start exploring interactions between multiple hinges, and the possible face deformations that might occur in elastic origami, we combine four of these non-linear hinges into a double-symmetric 4-vertex [51] (Fig. 5.2a). Note that we assume that the faces can only stretch and not bend [52], since bending can be modeled as an additional hinge [47], which changes the design of our vertex. The stretching of the faces is modeled by placing linear springs with stiffness k_s along the edges (Fig. 5.2a), introducing stretch energy E_s. As a result, the vertex' elastic energy ($E = E_h + E_s$) depends on two stiffness parameters k_s and k_h, and the rest angle Θ. Importantly, the stiffness parameters can be reduced to a single parameter $\kappa = k_h/k_s$, which defines the strength of the bistable behavior, and can

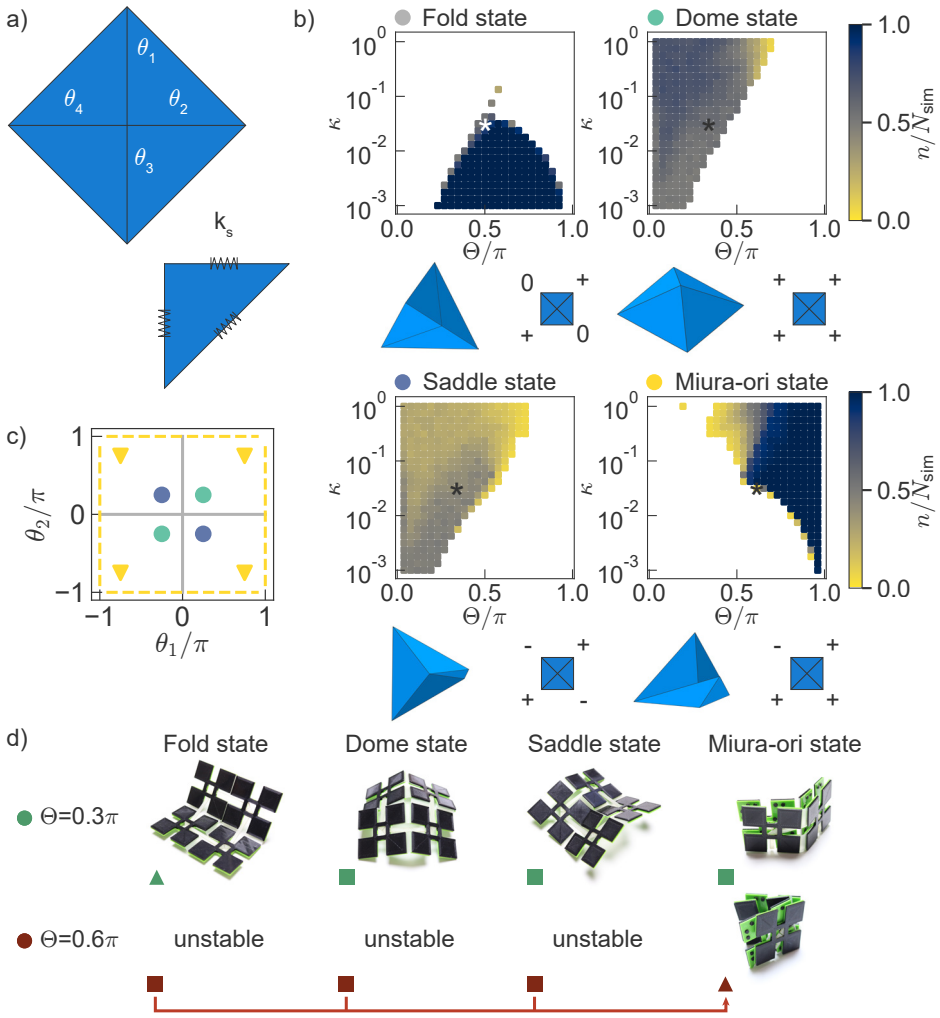

Figure 5.2 | a) Schematic of a double-symmetric 4-vertex with hinge angles θ_{1-4} and edges with linear spring stiffness k_s. b) Relative appearance of the four different stable states against the two parameters Θ and κ. Examples of the deformed stable states and the corresponding hinge orientation (0, + or -) are shown for the parameters indicated by the asterisk symbol. c) Branches (solid lines) and sub-branches (dashed lines) that exists for the 4-vertex, obtained by assuming a rigid origami model. When assuming an elastic origami model, the hinge angles tend to the circles ($\Theta = 0.25\pi$) or inverted triangles ($\Theta = 0.75\pi$). d) Experiments of two different prototypes of the vertices characterized by rest angles $\Theta = 0.3\pi$ and $\Theta = 0.6\pi$. Triangles show results from experiments in which the vertex was flattened and released, while squares show experiments in which the vertex was manually deformed towards the potential stable state prior to release.

be used to vary the behavior of the vertex between rigid and elastic.

To determine the folding behavior of the 4-vertex and the probability to find it in a certain state, we use Monte Carlo simulations. Assuming an initial hinge length equal to l_{flat}, we randomly perturb the nodal positions around the flat state using a normal

distribution with a standard deviation of $0.2l_{\text{flat}}$, which is approximately similar to an imperfect flattening of the vertex in experiments. Note that we use the flat state, an unstable position for the hinges, to start the simulations since typically origami starts from a flat configuration. Next, we release the hinges and let the vertex relax to its local energy minimum using a Sequential Quadratic Programming algorithm (Section 2.6). We only use the elastic energy derived from the possible deformation of the hinges and faces and ignore any dynamic contribution. We repeat this method $N_{\text{sim}} = 1000$ times for a range of combinations of κ and Θ, and use a two-step clustering algorithm to identify the stable states (Appendix C.2). We find that the vertex deforms into 16 different stable states when starting from a nearly flat state. However, by considering symmetries we can reduce them to four unique stable states (Fig. 5.2b and Fig. C.7), which we refer to as the *Fold* (F), the *Dome* (D), the *Saddle* (S) and the *Miura-ori* (M) state. Note that the names of the stable states represent the 3D configuration and does not imply neither typical origami patterns, i.e., the Miura-ori pattern, nor local shapes of the energy landscape, i.e. a saddle points.

5.3. Rigid and elastic vertex behavior

We can divide these four stable states into two categories, depending on the origin of the stability. In the first category, the stable states originate from a rigid origami model. In this model, the double-symmetric 4-vertex has two main branches, and four sub-branches that emerge when the angles are folded to their extremes (Fig. 5.2c) [51]. Therefore, this category comprehends the Fold and the Miura-ori state corresponding to the main branches (solid) and the sub-branches (dashed), respectively (Fig. 5.2c). One characteristic of these states is that the elastic energy increases with an increase in κ (Fig. C.7), since the faces do not deform and as such the stretch energy $E_{\text{s}} \approx 0$.

The second category comprises states that require face stretching. These states are the result of the elastic origami model combined with the torque resulting from the bistability. The elasticity transforms the branches and sub-branches of the vertex into soft modes, such that deformation outside of the branches is allowed. Since the bistability forces all the fold angles θ_{1-4} towards $\pm\Theta$ ($E_{\text{h}} \approx 0$), face stretching occurs. For example, when $\Theta = 0.25\pi$ (or 0.75π) the fold angles of the vertex try to move to the circular (or inverted triangular) markers in Fig. 5.2c, which lie outside of the branches originating from a rigid origami model. The stable states corresponding to this category are the Dome, the Saddle and the Miura-ori states. They correspond to all possible sign combinations of the rest angles that do not require face crossing [21]. The energy of these states is characterized by a dependency on Θ (and not on κ) since their elastic energy is dominated by the stretch energy $E \approx E_{\text{s}}$ (Fig. C.7). Note that the Miura-ori state belongs to both categories making it dependent on both Θ and κ.

5.4. Experimental validation of vertex states

To demonstrate these results experimentally, we built two prototypes of the double-symmetric 4-vertex (Fig. 5.2d), and used $l_{\text{spr}} = 30\,\text{mm}$ and $l_{\text{spr}} = 18\,\text{mm}$ to obtain $\Theta \approx$

0.3π and $\Theta \approx 0.6\pi$, respectively. As a first experiment, we flattened both vertices on a surface, and quickly released them (Movie 5.1 in Appendix D), reproducing the way the simulations are performed. The results are presented in Fig. 5.2d and marked with a triangle. We observed that the vertex with $\Theta \approx 0.3\pi$ always relaxes to the Fold state, while the vertex with $\Theta \approx 0.6\pi$ deforms into the Miura-ori state. Additionally, we performed a second experiment to try to obtain all possible stable states of the vertices. For this, we manually deformed the vertices into the remaining three states marked with a square in Fig. 5.2d. We found that for $\Theta \approx 0.3\pi$ the vertex is stable in all configurations. In contrast, for $\Theta \approx 0.6\pi$ the vertex always snaps to the Miura-ori state, indicating that other states are unstable and the Miura-ori state is the only stable state for this particular design. Based on these results, we can qualitatively match our prototypes with a vertex for which $\kappa \approx 10^{-1.5}$ in our simulations, although some difference exist due to additional deformation that can occur at the hinges (Fig. C.1).

5.5. Analysis of vertex metamaterials

Having characterized the stable states and their origin for a 4-vertex, the next step is to assemble this vertex in a square lattice, effectively creating a mechanical metamaterial [69]. By doing so, we can determine how the vertices interact with each other in such a material and how this affects the overall folding behavior. We first focus on a square lattice that consists of 4×4 vertices (Fig. 5.3a), where we set $\Theta = 0.25\pi$ and $\kappa = 10^{-1.5}$ according to approximated values based on the experiments of a single vertex. Starting from the flat configuration, we perform the same Monte Carlo simulation as for the single vertex.

To characterize the stable states of the material and to determine whether the folding behavior originates from a rigid or elastic framework, we first analyze the state of each vertex in the deformed material. We use the second step of the clustering algorithm previously employed (Appendix C.1), from which we get a 4×4 state matrix. Each entry of this matrix represents one of the four potential stable states of the vertex (Fig. 5.2b). Moreover, for each entry we also consider the orientation of the stable state. Here, the Fold state has two directions ($|$ and $-$), the Dome and Saddle state are symmetric in all directions, and the Miura-ori state has four directions ($>$, $<$, $\wedge$ and $\vee$) as illustrated in Fig. 5.3b. Interestingly, we find that the stable states of the material follow two different behaviors. Most of the simulations result in a stable state whose state matrix has a periodicity smaller than the total size of the metamaterial, while the other simulations present folding patterns with similar periodicities separated by boundaries (Fig. 5.3c).

To analyze and understand these results, we draw a similitude of our multistable origami metamaterials to 2D atomic crystal lattices. We let each vertex of our metamaterial correspond to an atom position and each stable vertex state to a different type of atom (Fig. 5.3b). The combination of these stable states in the specific vertex position can form periodic origami crystals with defined unit cells, just as a combination of atoms can form periodic crystals. Furthermore, as with atoms [119], these origami crystals can have defects. Specifically, only two kinds of defects can occur: crystal boundaries between the same type of crystals, and boundaries between dissimilar crystals. Other possible atomic defects involve the addition or subtraction of atoms, which for our metamaterials implies the addition or subtraction of vertices and thus the change of the material.

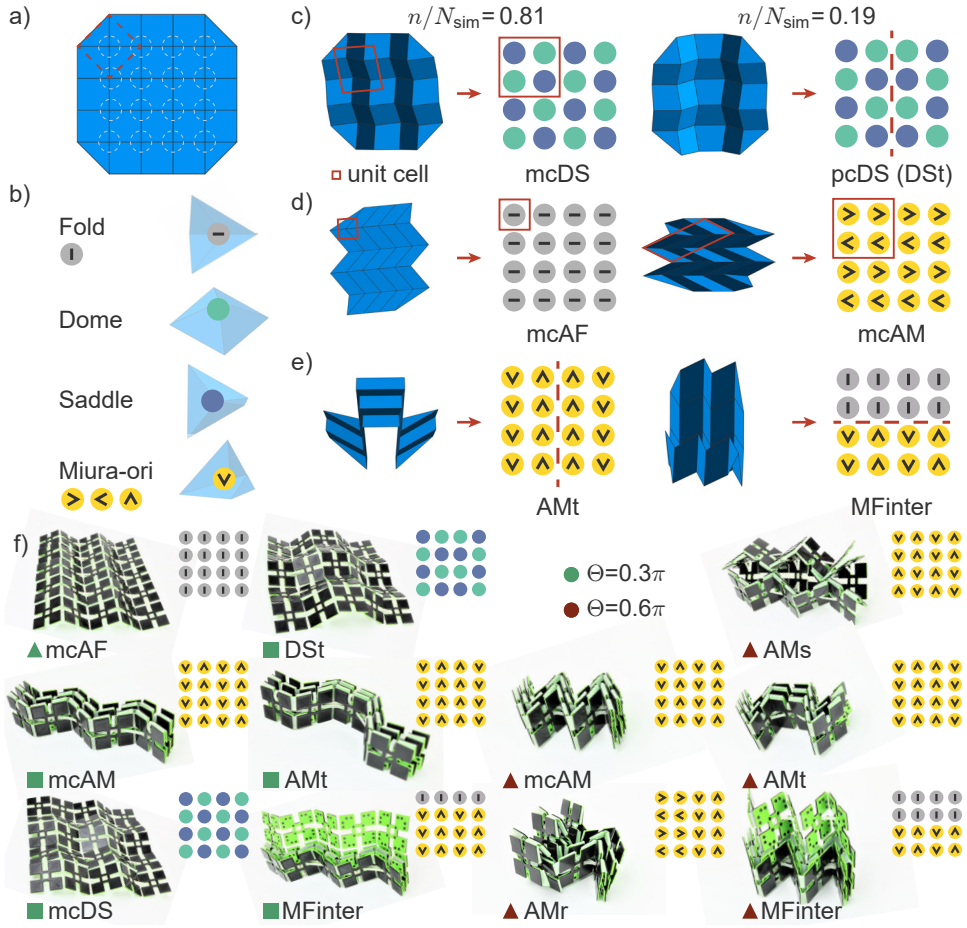

Figure 5.3 | a) Array of a vertex (dashed red square) in a 4 × 4 lattice. Circles represent atom positions. b) Possible stable states (atom types) and orientations of a single vertex. c) Results of $N_{\text{sim}} = 1000$ simulations of a metamaterial with $\kappa = 10^{-1.5}$ and $\Theta = 0.25\pi$. d) Other observed monocrystalline materials found by varying κ for two rest angles $\Theta = 0.25\pi$ and $\Theta = 0.75\pi$. e) Example of a twin boundary (AMt) and an interface between different crystal types (MFinter) observed in pcAM crystals. f) Experimental validation of two metamaterials characterized by rest angles $\Theta = 0.3\pi$ and $\Theta = 0.6\pi$. Triangles show results from experiments in which the vertex was flattened and released, while squares show experiments in which the vertex was manually deformed towards the stable state prior to release.

Following the terminology used in 2D atomic crystal lattices, if the metamaterial has only one type of crystal with all unit cells oriented in the same direction we call it monocrystalline (mc), whereas if there is any type of defect we call the material polycrystalline (pc) (Fig. 5.3c).

5.6. Potential stable states in the metamaterial

When applying this classification to our simulated metamaterial, we obtain one type of crystal with a unit cell of 2×2 vertices (Fig. 5.3c), characterized by a checkerboard pattern of Dome and Saddle states that we call the *Dome-Saddle* (DS) crystal. In $n/N_{\text{sim}} = 0.81$ of the simulations (with $N_{\text{sim}} = 1000$ the number of performed simulations), we obtain a monocrystalline DS (mcDS) material, while in the remaining simulations we obtain polycrystalline materials with only one type of boundary. This boundary is characterized by two neighboring crystals that appear as mirrored images, thus we call it a twin boundary (DSt).

We then perform more simulations using a range of parameters in the search for other types of crystals. We select two rest angles $\Theta = 0.25\pi$ and $\Theta = 0.75\pi$ that correspond approximately to the rest angles of the prototypes, while we vary κ. From these simulations, we identify two additional types of crystals, which we refer to as the *All-Fold* (AF), and the *All-Miura-ori* (AM) (Fig. 5.3d). These crystals have unit cell size equal to 1×1 and 2×2, respectively. Note that for the AM crystal we observe three types of crystal boundaries: rotational (AMr) with rotated crystals at the boundary, twin (AMt) with mirrored crystals, and slip (AMs) with shifted crystals (Fig. 5.3e and Fig. C.8). These correspond to the three different arrangements that neighboring unit cells can have. Interestingly, the AF crystal does not show any defects in our simulations, which we correlate to the fact that the fold state comes from the rigid origami model. Furthermore, we find interfaces between AM and DS crystal (MDinter), and AM and AF crystals (MFinter), but not between DS and AF crystals (Fig. 5.3e and Fig. C.8). These interfaces seem to only occur between crystals originating from the same model, MDinter from the elastic origami, and MFinter from the rigid origami model.

5.7. Experimental validation of metamaterial states

To demonstrate the existence of these crystals and crystal defects, we built a 4×4 material with vertices having low $\Theta \approx 0.3\pi$ and high $\Theta \approx 0.6\pi$. We first flattened the material and quickly released it (Movie 5.1 in Appendix D), as done for the single vertex. We find that the metamaterial with low Θ always relaxes to an mcAF material, while the metamaterial with high Θ relaxed to either a mcAM or a pcAM with all possible defects (AMr, AMt, AMs, and MFinter) as marked with a triangle in Fig. 5.3f. We next performed the second experiment where we deformed the material to specific states to obtain all possible stable states. For the low Θ metamaterial, we additionally obtained DS and AM crystals, both monocrystalline and polycrystalline with some defects (DSt, and AMt and MFinter, respectively) as marked with a square in Fig. 5.3f. On the contrary, for the high Θ material we did not obtain any other crystal or crystal defects. These results match qualitatively our simulations.

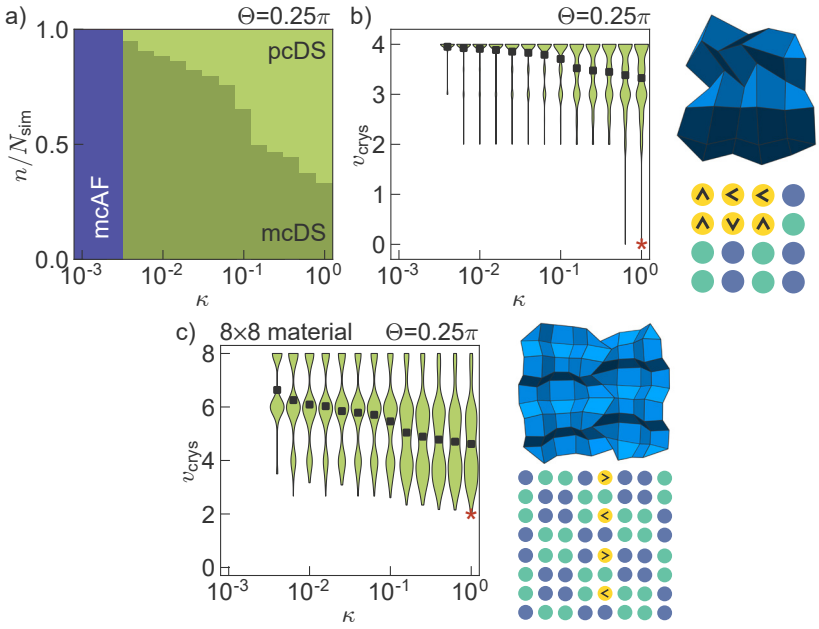

Figure 5.4 | a) Percentage of simulations (n/N_{sim}) for which the stable state is either monocrystaline or polycrystaline, indicated for each crystal type. Distribution of crystal size (v_{crys}) against κ for b) a 4×4 and c) a 8×8 material. The black dots represent the mean of the distribution. Examples (asterisk) of stable state with the lowest v_{crys}.

5.8. Rigid to elastic transition

Next, to determine how the strength of the bistable hinges affects the behavior of the metamaterial, we identify all crystals and their defects of the previous parameter study (Appendix C.3). In Fig. 5.4a we show the percentage of simulations of the material with $\Theta = 0.25\pi$ (n/N_{sim}) that are either monocrystalline or polycrystalline, indicated for each crystal type. For low values of κ we only observe mcAF crystals. However, when increasing κ, a sudden transition occurs to a different crystalline metamaterial. We find that the mcAF state transitions to a mcDS state at $\kappa \approx 10^{-2.5}$. Interestingly, the transition happens at the same κ as in Fig. 5.2b when the single vertex goes from the Fold state to the Dome or Saddle state (for $\Theta = 0.25\pi$). Note that we observe the same behavior for a material with $\Theta = 0.75\pi$ (Fig. C.9). This is a clear indication of a transition from the rigid origami behavior represented by the AF crystal to an elastic origami behavior represented by the DS crystal.

5.9. Elastic to amorphous transition

Additionally, when increasing κ further, we notice that polycrystalline metamaterials start to appear, and the amount of monocrystalline metamaterials decreases (Fig. 5.4a).

We determine the average size of the crystal domains present in a single metamaterial v_{crys} (Appendix C.3). This crystal size represents a characteristic length-scale for the influence that a vertex has on its neighbours [72]. In Fig. 5.4b we plot the distribution of the average crystal size in a metamaterial against κ for all the DS crystals with $\Theta = 0.25\pi$. We see that the average crystal size decreases when κ increases, even reaching zero for some cases at $\kappa > 10^{-0.4}$. This means that the stable state of this metamaterial characterized by $v_{crys} = 0$ has no clearly defined crystal domains, and is only composed of defects (Fig. 5.4b). Following the analogy of 2D atomic crystal lattices, we find that the deformed state of the metamaterial is amorphous.

When repeating the same simulations for a larger metamaterial consisting of 8×8 vertices (Fig. 5.4c), we still observe this decrease in the crystal size with κ. However, we do not yet observe a metamaterial with $v_{crys} = 0$. The smallest crystal size we obtain is $v_{crys} = 2$, where the metamaterial consists only of unit cells that are separated by defects (Fig. 5.4c). Here it should be noted that the observed stable state in this example does not appear to be completely random, and is characterized by 2 regions of the same 4×4 periodicity, separated by a line of defects. We thus observe the importance of the material size, and more specifically, the effect that edges have on the stability and folding behavior of the crystal domains. On the one hand, for smaller sizes of the metamaterial, the edges dominate the behavior since they relax the face deformation of defects, and thus allow for more possible stable states. On the other hand, for a larger metamaterial the bulk behavior dominates and the face deformation is restricted by the neighbor vertices. Note that the same observations can be made for metamaterials with higher $\Theta = 0.75\pi$ (Fig. C.9).

Importantly, these results indicate a change in behavior upon an increase of κ, from elastic origami with well defined crystals to an amorphous material with non-defined deformations. In contrast to the sudden transition from rigid origami to elastic origami observed for lower κ, the transition to an amorphous material appears to be continuous, and depends on the material size (Fig. C.10).

5.10. Discussion

In this work we show the rich behavior that appears in origami-inspired metamaterials when using bistable hinges. By applying methods that are often used to analyze defects in atomic crystal lattices, we are able to determine the most important parameters that affect the metamaterial's behavior, and identify three main regimes. *(i)* For weak bistability, hinge folding dominates over face stretching and the metamaterial behaves according to a rigid model. *(ii)* Upon strengthening the bistability, a sudden transition occurs to periodic stable states that depend on face deformations, and that are the result of the elastic model. *(iii)* Strengthening the bistability further introduces defects, creating domain boundaries between several stable regions with decreasing crystal size, and leading to the point where the metamaterial's behavior becomes completely amorphous.

We expect these transitions to occur in most origami materials, thus the identification of these three regions is important to determine how to obtain the desired folding behavior. While in case of rigid origami, a global stimulus could guide the folding behavior of the sheets, in case of elastic origami the stimulus needs to be distributed according

to a length-scale governed by the characteristic crystal size. With these considerations one can place constraints on multistable metamaterial designs and their engineering realization at various length-scales.

6

Discussion

6.1. Conclusion

This thesis describes origami patterns and origami-inspired metamaterials with an elastic origami model. This model incorporates deformations that the rigid origami model fails to describe, opening the possibility of new folding behaviors. Nevertheless, applying this model comes at a cost. The elastic origami model introduces many additional degrees of freedom. These degrees of freedom create non-linearities from the interaction between hinges and deformation of the faces. This non-linearity causes three main problems that this thesis addresses.

6.1.1. Simplification of the elastic origami model

The first problem of the elastic origami is apparent in Chapter 3 where the degrees of freedom are presented as normal modes. The number of degrees of freedom due to the addition of face deformation in the modeling of origami complicates the characterization of the folding behavior. Furthermore, these modes depend on a set of parameters that define the stiffnesses of the different deformations in the structure. Therefore, in order to simulate real life origami, we need to know all the stiffness parameters. To obtain a simpler description of the origami behavior we need to answer the following question: *is it possible to simplify the model in order to study complex origami designs based on real life experiments?*

In Chapter 3, we present a simplification of the elastic origami model that helps us describe complex origami-inspired metamaterials in the other chapters. In contrast to typical simplifications of the elastic model, here we constrain face bending but allow face stretching. This can be seen unrealistic since for thin faces bending requires less energy than stretching. However, our simplification still represents real origami behavior since the stretching of the faces are seen as stretching or twisting of the hinges. In fact, our simplifications has shown an accurate prediction of the deformation of origami in real life.

Simplifying the model is important when simulating complex structures. First, because the computational time increases with the number of components, especially when simulating more than just the building block, what usually is done [54, 55]. It is known that there can be deformation patterns that span over several unit cells in metamaterials [120]. Second, this simplification has helped us define a single parameter, which we use to tune the elastic stiffnesses. Therefore, with a simpler model we can simulate larger metamaterials with many unit cells to understand behaviors that span through the entire material for different material stiffnesses.

6.1.2. Exploring the folding behavior

The second problem derives from the many degrees of freedom which make the characterization of the folding behaviors of complex origami almost impossible. Characterizing the folding behavior in the highly non-linear energy landscape of origami can be compared to finding a needle in a haystack. For this we develop two different algorithms. These algorithms help to answer the question: *can we find a way to systematically char-*

acterize the deformation space in the elastic origami model?.

The description of the deformation through normal modes used in Chapter 3 can be used as a way to systematically navigate the folding behavior. Origami metamaterials have many degrees of freedom according to the elastic origami model, however these can be modeled as normal modes. These modes give a good description of the deformation, especially the soft and pseudo soft modes since they have a low elastic energy with minimum face deformation, and therefore are the most probable to appear in real life origami.

This description of the normal modes gives a folding direction of the structure despite being only valid around a specific configuration due to the infinitesimal framework. If we deform slightly the structure along a normal mode and then run a minimization algorithm, such as the one described in Chapter 4, we can obtain a new deformation state of the origami structure. From this state we can obtain again the normal modes in an infinitesimal framework and start again the cycle. By following this cycle of the two algorithms we can obtain accurately possible deformations of origami structures in order to characterize the folding behavior.

In addition to the normal modes description, the energy landscape scan used in Chapter 4 has proven to be a straightforward method to systematic search for new stable states. Note that our method only shows an initial exploration of the energy landscape and does not give all stable states. In this chapter, we used specific deformation patterns to reach multiple stable states. These patterns resemble the closing or opening of hinges in the origami metamaterial. By applying forces on these hinges in real life prototypes we obtain the same deformation and stable states.

This local actuation description is useful when producing metamaterials. The actuation pattern describes the possible hinges needed to be folded in order to obtain a specific stable state. By considering this actuation pattern when fabricating the metamaterial, we can embed it in the hinges of the origami structure. This can be done using, for example, pneumatic pouches [55, 121] or responsive materials such as hydrogels [122, 123].

6.1.3. Finding actuation patterns

The third problem of the elastic origami model comes from the elasticity of the faces that cannot transform a local deformation into global behavior. In the rigid origami model, the entire metamaterial can be deformed using local actuation due to a mechanism-like behavior. On the contrary, in the elastic origami model, the mechanism-like behavior is damped due to the many degrees of freedom of the system. This damping prevents the global deformation and dictates how far local actuation can deform the structure, defining a characteristic length [67]. So, *how can we obtain well-defined folding behavior in the elastic origami model?*

To answer this question, in Chapter 5 we describe the folding behavior of non-linear origami with bistable hinges. The bistability of the hinges acts like an actuation that deforms the origami. This deformation is localized in areas whose size depends on the stiffness regime of the metamaterial. This has been previously seen in other metamaterials [72] and we expect other origami patterns [42, 54] to have a similar behavior. These

areas can be then actuated in order to have a well-defined behavior.

From Chapter 5 we obtain a guideline of the actuation pattern in a large metamaterial. By knowing the stiffness regime of the origami metamaterial in real life we can deduce how far an actuation influences its folding behavior. This gives a guideline on the number of actuation locations we need to set on the material to obtain a well-defined global behavior. This is specially useful when creating large metamaterials with many unit cells.

6.1.4. Small scale origami metamaterials

Overall, this thesis helps to understand the behavior of origami for real life fabrication. The elastic origami model has an advantage over the rigid model since it takes into consideration real life deformations that sometimes are difficult to constrain. Therefore, by knowing how elastic origami metamaterials deform we can have a clear guideline to fabricate these materials and control them. Additionally, with the elastic origami model described in Chapter 2, we can compare the real life behavior of origami patterns with simulations. Since the algorithm is purely based on the elastic energy, we can apply it to any origami patterns. By adjusting the stiffnesses of the springs, we can describe the folding behavior of prototypes in a static framework. This numerical algorithm helps to understand the behavior of not only the origami-inspired metamaterials in this thesis, but origami in general, and thus allows to have a better description for future applications.

This elastic origami model is scale-independent, however small scaled origami metamaterial have yet not been studied in depth. Our model is specially useful when producing origami at small scales [19, 123–125] since the stiffness of the springs can vary [19, 76] forming origami metamaterial with very elastic faces. I envision a future in which metamaterials have unit cells so small that we would not be able to differentiate them from common materials.

6.2. Future perspective for origami metamaterials

This thesis describes the behavior of elastic origami and proposes new methods to control its behavior, however it raises further questions. Here, I lay down some of these questions and propose a way to answer them as future perspective on elastic origami.

6.2.1. Fabrication of small scale metamaterials

Origami metamaterials are typically studied at scales larger than 10 cm. While these structures can be useful for applications in architecture or space engineering, their implementation at small scales is not simple. *How does the geometry need to change in order to scale it down?*

Origami metamaterials are formed from soft hinges and stiffer faces. At large scales this is done by either weakening the material at the hinge (folding a piece of paper) or using a softer material for the hinges. To scale down the origami metamaterial, we need to do the same. By choosing, for example, a polymer to fabricate these structures at small

scale, we can control the cross-linking of the polymer chains. If the polymer is highly cross-linked, it will become harder, but by reducing the cross-linking, the polymer will be softer. This can be used to produce faces and hinges, respectively.

In order to control the geometry of the metamaterials, we need to choose an appropriate fabrication method. *How can we fabricate origami-inspired metamaterials at small scale?*

To answer this question we need to look for new fabrication methods. Most of the small scale fabrication methods produce 2D shapes on top of a rigid substrate. Moreover, these methods have a restricted material availability complicating the control of the metamaterial stiffness. To create 3D origami patterns, we can use newer methods like two-photon lithography [76] which has a broader availability of materials and can create larger metamaterials. This method allows the fabrication of small scale unit cells (less than 1 mm).

The forces that govern the behavior of origami structures at large scales differ much from the ones that govern small scale structures. At the small scales, forces such as surface tension, electrostatics and diffusion can control the folding behavior of origami. In order to obtain a specific behavior for an application, we need to use these forces in our favor. *How can we control these metamaterials?*

This thesis gives a guideline using local actuation to deform origami metamaterials which can be use to control them at smaller scales. Our actuation approach could be embedded during the fabrication process using active materials such as liquid crystals [126]. These material can be controlled by adjusting their environment such as heat or light exposure. Metamaterials at small scales can lead future technologies since its behavior can be designed for any application.

6.2.2. Navigating the deformation space

Our actuation guideline from Chapter 4 is based on folding a specific set of hinges. We obtain these sets by analyzing the symmetries of the structure. However, obtaining these sets of hinges is complex and difficult to apply to other structures. To be able to generalize, *is there an approach to define the actuation hinges for any origami-inspired metamaterials?*

In Chapter 3 we use a dynamic model to obtain the kinematics of the building blocks of a metamaterial in an infinitesimal deformation framework that could help answer this question. By applying the same approach to arrays of building blocks we can decompose the kinematics of the normal modes around a specific state into set of hinges. The set with the most deformations could be the actuation set. This method can be used as a general approach to define the actuation hinges for any origami-inspired metamaterial.

Furthermore, we use local actuation by assigning angles to a set of hinges in Chapter 4. We see that actuating this set of hinges in a different sequence can lead to different stable state. This means that the actuation defines the folding pathway of the metamaterial, *but how can we obtain the best pathway for a specific application?*

A way to obtain the best pathway to a specific behavior can be by introducing a dynamic term in our algorithm since this thesis focuses on static algorithms. In Chapter 5 we see that the dynamics of the experiment affects the stable state of the metamaterial.

So, by introducing the kinetic energy that depends on the initial state and the previous deformations, we can navigate the energy landscape in a more realistic way that would mimic real life behavior. Moreover, this dynamic term can help us overcome energy barriers with less actuation.

For Chapter 4 we use local actuation at the hinges to deform the structure. In our experiments this means that we manually actuate the hinges. While this is possible in large scale origami metamaterials, at smaller scales this is impossible. *Are there other actuation mechanisms that we can use to navigate the deformation space?*

The actuation described in this thesis was generally defined as the closing of hinges, however simpler actuation for metamaterials, specially at small scales, such as uni-axial compression or swelling, can be easier to fabricate. A problem can be that these simpler deformations can make the structure follow a different folding pathway in the energy landscape which in turn leads to a different behavior due to the multi-dimension of the energy landscape. It is important to investigate simpler actuation patterns and how to control the navigation through the deformation space.

6.2.3. Local or global behavior

Origami-inspired metamaterials are typically studied to obtain the deformation of the structure as a whole since this can be easily extrapolated from the behavior of the unit cell. This thesis follows the same line by focusing on a global folding behavior of origami metamaterials. Nevertheless, local deformations in a large metamaterial can be used for different applications. *Can a metamaterial switch between local and global behavior?*

The switching between these two behavior can be achieved with a clever design. For example, we can design a metamaterial in which specific local forces deform only individual building blocks but by applying a force in a different way the metamaterial as a whole can be deformed back to its initial state. This type of metamaterial can be used as a energy storage device or reversible damping materials.

Finally, local deformation, specially at the edges of the material can be interesting. As seen in Chapter 5, the building blocks at the edges of the bistable metamaterial relax the stress induced by the elastic behavior. These building blocks at the edges require less energy to be deformed than the building blocks at the bulk of the metamaterial. *Can we exploit the edge relaxation to create new folding behaviors?*

Topological metamaterials constrain certain deformation to specific areas of the metamaterial [27], specially on the edges. In this way, building blocks at the edges can be designed to deform while the building blocks in the bulk remain undeformed. This will create topological metamaterials whose behavior can be controlled by adjusting the stiffness of the material.

A

Appendix: Elastic folding behavior of prismatic structures

Based on: Iniguez-Rabago, A., and Overvelde, J.T.B., *Elastic folding behavior of prismatic structures.* (In preparation)

A

A.1. Euler-Lagrange equation of motion

The Euler-Lagrange equation is defined as

$$\frac{d}{dt}\left(\frac{\partial L}{\partial \dot{\boldsymbol{u}}}\right) - \frac{\partial L}{\partial \boldsymbol{u}} = 0, \tag{A.1}$$

where $\boldsymbol{u}$ and $\dot{\boldsymbol{u}}$ are the displacement and velocity of the vertices, respectively. The Lagrangian $L = E_{\text{kinetic}} - E_{\text{elastic}}$ depends on the kinetic and elastic energy described by Eqs. 2.1 and 2.19, respectively. Importantly, in our model we assume that the elastic energy is only dependent on the displacement and the kinetic energy on the velocity. This simplifies the equation

$$\frac{d}{dt}\left(\frac{\partial E_{\text{kinetic}}}{\partial \dot{\boldsymbol{u}}}\right) - \frac{\partial E_{\text{elastic}}}{\partial \boldsymbol{u}} = 0. \tag{A.2}$$

We can obtain the derivatives of the kinetic energy following

$$\frac{d}{dt}\left(\frac{\partial E_{\text{kinetic}}}{\partial \dot{\boldsymbol{u}}}\right) = \frac{1}{2}\boldsymbol{M}\ddot{\boldsymbol{u}}, \tag{A.3}$$

where $\ddot{\boldsymbol{u}} = \partial \dot{\boldsymbol{u}}/\partial t$ and $\boldsymbol{M}$ is the mass matrix. The derivative of the elastic energy is defined by Eq. 2.2 and can be written as

$$\frac{\partial E_{\text{elastic}}}{\partial \boldsymbol{u}} = \frac{1}{2}\boldsymbol{J}_{\text{hinge}} k_{\text{h}} \boldsymbol{J}_{\text{hinge}} \boldsymbol{u} + \frac{1}{2}\boldsymbol{J}_{\text{stretch}} k_{\text{s}} \boldsymbol{J}_{\text{stretch}} \boldsymbol{u} + \frac{1}{2}\boldsymbol{J}_{\text{bend}} k_{\text{b}} \boldsymbol{J}_{\text{bend}} \boldsymbol{u}, \tag{A.4}$$

where $\boldsymbol{J}_{\text{hinge}}$, $\boldsymbol{J}_{\text{stretch}}$ and $\boldsymbol{J}_{\text{bend}}$ are defined by Eqs. 2.6, 2.12 and 2.16, respectively. k_{h}, k_{s} and k_{b} are the stiffness of the springs in the model corresponding to the hinge folding (Eq. 2.3), face stretching (Eq. 2.9) and face bending of the structure (Eq. 2.13), respectively. This leaves the equation as

$$\frac{1}{2}\boldsymbol{M}\ddot{\boldsymbol{u}} - \frac{1}{2}\boldsymbol{K}\boldsymbol{u} = 0, \tag{A.5}$$

where $\boldsymbol{K} = \boldsymbol{J}_{\text{hinge}} k_{\text{h}} \boldsymbol{J}_{\text{hinge}} + \boldsymbol{J}_{\text{stretch}} k_{\text{s}} \boldsymbol{J}_{\text{stretch}} + \boldsymbol{J}_{\text{bend}} k_{\text{b}} \boldsymbol{J}_{\text{bend}}$ is the stiffness matrix and can be rewritten as $\boldsymbol{K} = \boldsymbol{K}_{\text{hinge}} + \boldsymbol{K}_{\text{stretch}} + \boldsymbol{K}_{\text{bend}}$.

A.2. Solution of the Euler-Lagrange equation

To solve the Euler Lagrange equation we assume a general solution in the form of

$$\boldsymbol{u} = \boldsymbol{v}\sin(\omega t + \beta). \tag{A.6}$$

We then substitute this solution in Eq. A.5 and after rearranging the terms we obtain

$$\boldsymbol{K}^{-1}\boldsymbol{M}\boldsymbol{v} = \lambda \boldsymbol{v}, \tag{A.7}$$

where $\lambda = \omega^2$. This equation defines now an eigenvalue problem, where $\boldsymbol{v}$ is the eigenvector and λ the corresponding eigenvalue. These eigenvectors represent the normal modes of the structure with the corresponding frequency ω.

A.3. Deformation and energy of the normal modes

By assuming an initial condition of $\boldsymbol{u}(t=0)=0$, the solution (Eq. A.6) can be rewritten as

$$\boldsymbol{u} = \boldsymbol{v}\sin(\omega t). \tag{A.8}$$

Moreover, at $t_{\max} = \pi/(2\omega)$ we obtain the largest deformation $\boldsymbol{u}_{\max} = \boldsymbol{v}$. Since $\boldsymbol{v}$ is an eigenvector, it can be rescaled by any factor. Therefore, we normalize $\boldsymbol{v}$ with its magnitude to have a unitary eigenvector $\hat{\boldsymbol{v}} = \boldsymbol{v}/|\boldsymbol{v}|$, so the maximum deformation of the normal modes becomes $\boldsymbol{u}_{\max} = \hat{\boldsymbol{v}}$.

Interestingly, at $t_{\max}$ the kinetic energy is zero because the velocity $\dot{\boldsymbol{u}} = \hat{\boldsymbol{v}}\omega\cos(\omega t)$ is zero. Additionally, since the system is closed, the energy is constant. Thus, at $t_{\max}$ the total energy of the structure is the elastic energy at the maximum deformation $\boldsymbol{u}_{\max}$, following

$$E_{\text{tot}} = \frac{1}{2}\boldsymbol{u}_{\max}^T \boldsymbol{K}\boldsymbol{u}_{\max}. \tag{A.9}$$

We then can calculate the three different components of the elastic energy, the hinge folding energy, the face stretching energy, and the face bending energy with

$$\begin{aligned} E_{\text{hinge}} &= \frac{1}{2}\boldsymbol{u}_{\max}^T \boldsymbol{K}_{\text{hinge}}\boldsymbol{u}_{\max} \\ E_{\text{stretch}} &= \frac{1}{2}\boldsymbol{u}_{\max}^T \boldsymbol{K}_{\text{stretch}}\boldsymbol{u}_{\max} \\ E_{\text{bend}} &= \frac{1}{2}\boldsymbol{u}_{\max}^T \boldsymbol{K}_{\text{bend}}\boldsymbol{u}_{\max}, \end{aligned} \tag{A.10}$$

respectively.

A.4. Constraining deformation

There are two types of deformation that we constrain, face stretching and face bending. The face bending constraint is defined by Eq. 2.23, while the face stretching constraint follows Eq. 2.27. These set of equations can be rewritten in a matrix form so that

$$\boldsymbol{C}\boldsymbol{u} = 0, \tag{A.11}$$

where each row of $\boldsymbol{C}$ represents one constraint equation. We then switch from the Cartesian coordinates $\boldsymbol{u}$ to the generalized coordinates $\boldsymbol{q}$ with a transformation matrix $\boldsymbol{T}$ following

$$\boldsymbol{q} = \boldsymbol{T}\boldsymbol{u}. \tag{A.12}$$

We use the generalize coordinates to define the Euler-Lagranege equation (Eq. A.5), its solution (Eq. A.6) and the corresponding eigenvalue problem (Eq. A.7). After, it is straightforward to transform the generalized coordinates to the Cartesian coordinates in order to obtain the deformation of the structure.

A.5. Additional Results

A

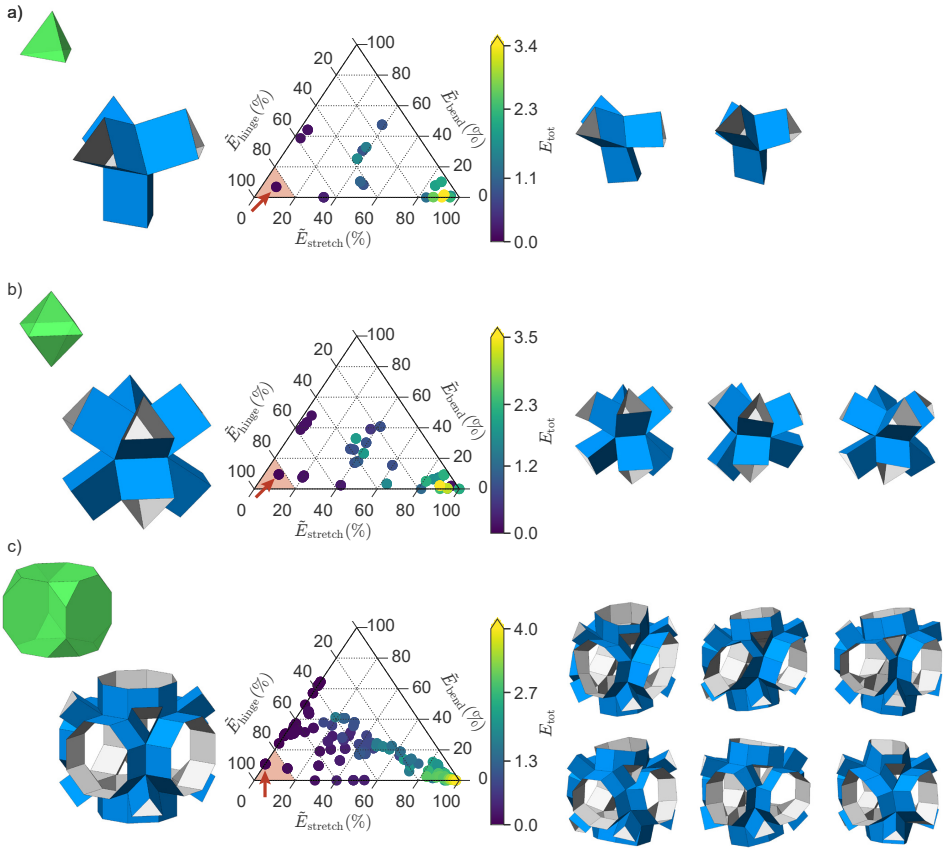

Figure A.1 | Polyhedron and corresponding prismatic structure, energy distribution of the normal modes according to the elastic origami model in the stiffness regime where $k_{\text{h}} = 10^{-4}$, $k_{\text{b}} = 10^{-2}$, and $k_{\text{s}} = 10^{0}$, and deformation of pseudo soft modes for the structures based on a) a tetrahedron, b) a octahedron, and c) a truncated cube. The location of the modes is indicated in by an arrow, and the colored area represents the hinge corner.

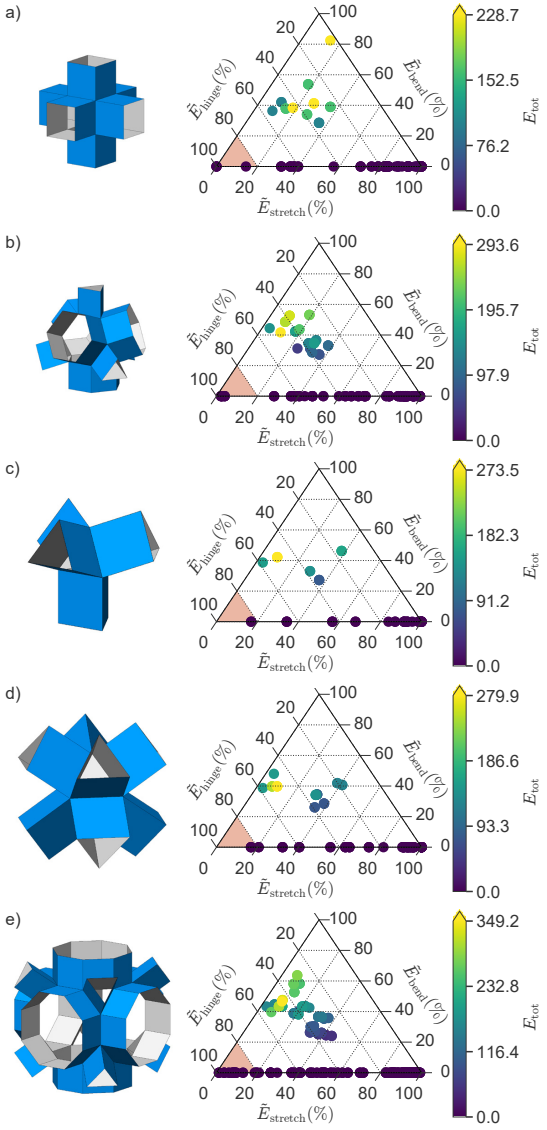

Figure A.2 | Prismatic structure and energy distribution of the normal modes according to the elastic origami model in the stiffness regime where $k_h = 10^{-4}$, $k_s = 10^{-2}$, and $k_b = 10^{0}$ for the structures based on a) a cube, b) a truncated tetrahedron, c) a tetrahedron, d) a octahedron, and e) a truncated cube.

A

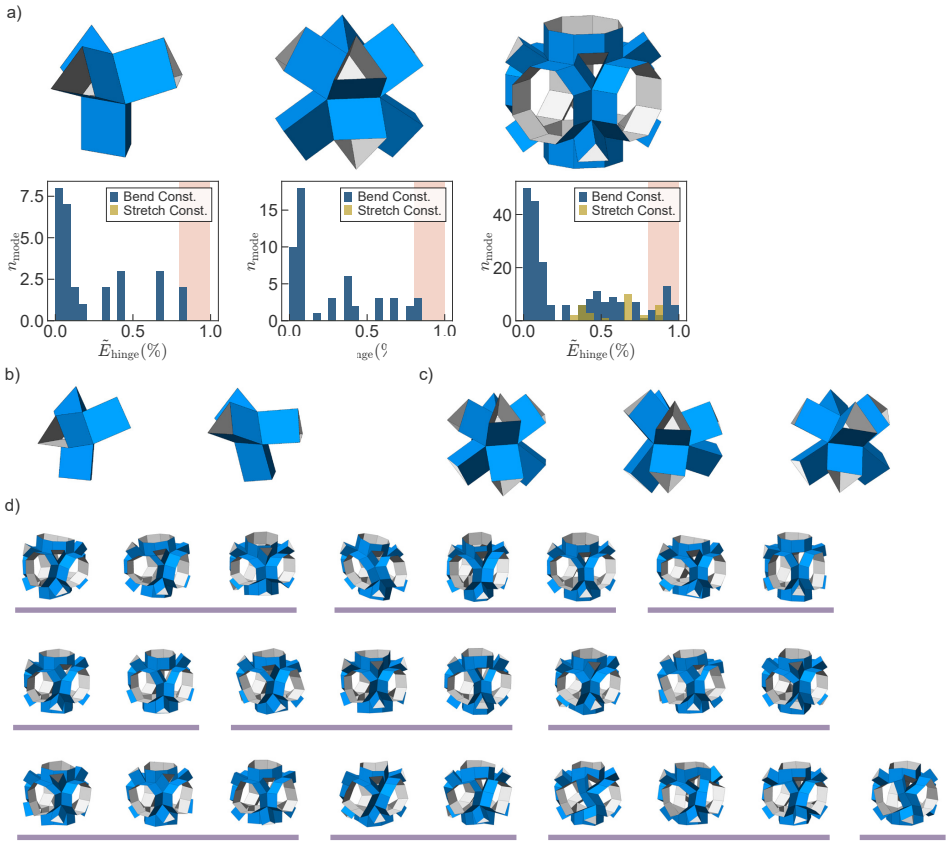

Figure A.3 | a) Energy distribution of the normal modes assuming the reduced models, bend constraint model and stretch constraint model, for structures based on a tetrahedron, a octahedron and a truncated cube. The colored area shows where the pseud-hinge modes are located. b), c) and d) Deformation of the pseudo soft modes of these structures, respectively. Modes that have the same energy are underlined.

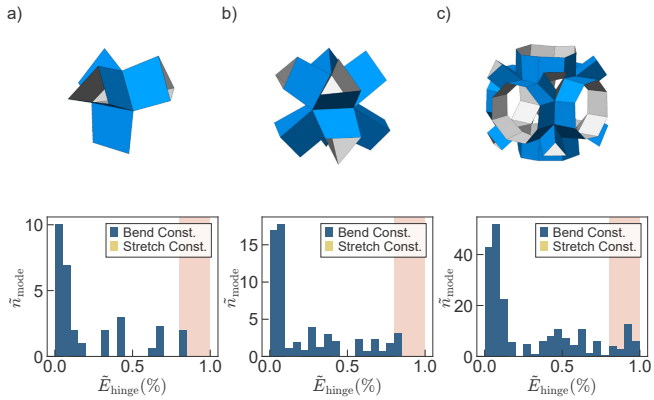

Figure A.4 | Perturbation of the nodes and energy distribution according to the reduced models of structures with imperfections based on a) a tetrahedron, b) octahedron and c) truncated cube. Note that the perturbation is 5× magnified to be able to see it, and that the energy distributions of the modes without imperfections are shown in Fig. A.3

B

Appendix: Exploring multistability in prismatic metamaterials through local actuation

B.1. Normalization of Energy

To compare the results between prismatic structures based on different polyhedra, we normalize the elastic energy. The elastic energy of any structure is given by Eq. 2.1. Note that the constraints Eq. 2.24 and Eq. 2.25 limit the deformation of the fold angles θ_i and the edge length l_i, respectively, and therefore we can define a total maximum energy when all the fold angles and edge lengths are at their maximum, respectively $\theta_i^{\max}$ and $l_i^{\max}$. The maximum hinge energy is then equal to

$$E_{\text{hinge}}^{\max}(\boldsymbol{\theta}) = \sum_{i=1}^{H} \frac{1}{2} k_{\text{h}} (\theta_i^{\max} - \Omega_i)^2 = \frac{1}{2} k_{\text{h}} (\boldsymbol{\theta}^{\max} - \boldsymbol{\Omega}) \cdot (\boldsymbol{\theta}^{\max} - \boldsymbol{\Omega}). \tag{B.1}$$

Similarly, the maximum energy as a result of in-plane face deformation equals

$$E_{\text{stretch}}^{\max} = \sum_{i=1}^{S_E+S_D} \frac{1}{2} k_{\text{s}} (l_i^{\max} - L_i)^2 = \frac{1}{2} k_{\text{s}} (\boldsymbol{l}^{\max} - \boldsymbol{L}) \cdot (\boldsymbol{l}^{\max} - \boldsymbol{L}). \tag{B.2}$$

We then define the total normalized elastic energy $\tilde{E}_{\text{elastic}}$ according to

$$\tilde{E}_{\text{elastic}} = \frac{E_{\text{elastic}}}{E_{\text{elastic}}^{\max}} = \frac{E_{\text{elastic}}}{E_{\text{hinge}}^{\max} + E_{\text{stretch}}^{\max}}, \tag{B.3}$$

and the individual components of the elastic energy are given by

$$\tilde{E}_{\text{hinge}} = \frac{E_{\text{hinge}}}{E_{\text{hinge}}^{\max}} \tag{B.4}$$

$$\tilde{E}_{\text{stretch}} = \frac{E_{\text{stretch}}}{E_{\text{stretch}}^{\max}}. \tag{B.5}$$

B.2. Compression test

To verify the numerical model we performed an experimental compression test on a prismatic structure based on a cuboctahedron. Here, we describe the simulation of the compression test that we used as a comparison. In our simulations, we use a stiffness ratio of $\kappa = 10^{-4}$. We select two opposite faces on the structure, and apply constraints to the vertices that mimic the clamping in experiments. To do so, we only allow deformation of the vertices along the compression axis. We then create two additional edges (S_{comp}) parallel to the loading axis, and use them to connect both clamped faces. We use these edges to compress the structure by stepwise reducing their length and penalizing the energy according to

$$E_{\text{load}} = \sum_{i=1}^{S_{\text{comp}}} \frac{1}{2} k_{\text{p}} (l_i - L_i)^2, \tag{B.6}$$

where k_{p} is the stiffness of the edges used to compressed the structure. We assign a stiffness that is much larger than the edge stretching stiffness and the hinge stiffness

($k_p \gg k_s, k_h$), so that effectively we are performing a displacement controlled compression.

In the simulation, we compress the structure in 1000 steps (n_{comp}), after which we stepwise remove the loading in the same number of steps. For each increment we allow the structure to relax with the specified constraints, while using previously mentioned optimization tool with the 'Active-set' algorithm.

To obtain the reaction force, F, during loading, we take the derivative of the elastic energy with respect to the displacement along the loading axis (z-axis), and find

$$F = \frac{dE}{dz} = \sum_{i=1}^{n_{comp}-1} \frac{E_{i+1} - E_i}{z_{i+1} - z_i}, \tag{B.7}$$

where we iterate through all the steps of the simulation to obtain the numerical gradient. Furthermore, we normalize the force by the weighted average of the stiffness defined by

$$\tilde{k} = \frac{k_s(S_E + S_D) + k_h H}{S_E + S_D + H}, \tag{B.8}$$

where S_E, S_D and H are the total number of edges, diagonals and hinges, respectively.

B.3. Force-displacement with different stiffness

With the normalize force we can compare the behaviour when we change the stiffness of the structure. In Fig B.1 we plot the same compression test with equal constraints, but different hinge stiffness k_h equivalent to different κ. As we can see we can increase κ at least one order of magnitude and the behaviour of the structure remains the same. Only by increasing it by two orders of magnitude the behaviour changes. This means that we are on the limit where the hinge stiffness k_h does not play a role on the energy of the deformation and therefore stretched faces becomes the main deformation.

B.4. Stable States clustering

In order to obtain the stable states that are unique under rotational or mirror symmetry, we consider the angles of all the hinges in the prismatic structure n_{tot} in the final stable configuration, and place them in a n_{tot}-dimensional array, $\boldsymbol{\theta}_{stable}$. We then separate the internal and external angles into two different groups. For each group we arrange the angles in order of increasing value. By doing so, we remove the spacial position of the hinges and obtain only the values of the angles in a specific order, thus considering all rotational and mirror symmetries. Next, we compare the ordered $\boldsymbol{\theta}_{stable}$ arrays of all the stable state to cluster the ones that are similar to each other. For this we use a hierarchical clustering with centroid linkage [127] and a euclidean distance metric to shape the clusters. The maximum distance inside a cluster is of 1.5 rad. Therefore, we consider configurations with an average error of $\frac{1}{\sqrt{n_{tot}}}$ rad in every angle to be the same configuration. This error is up to 13.5 deg for the smallest structure, the one based on a tetrahedron, and 7.8 deg for the one based on a truncated tetrahedron.

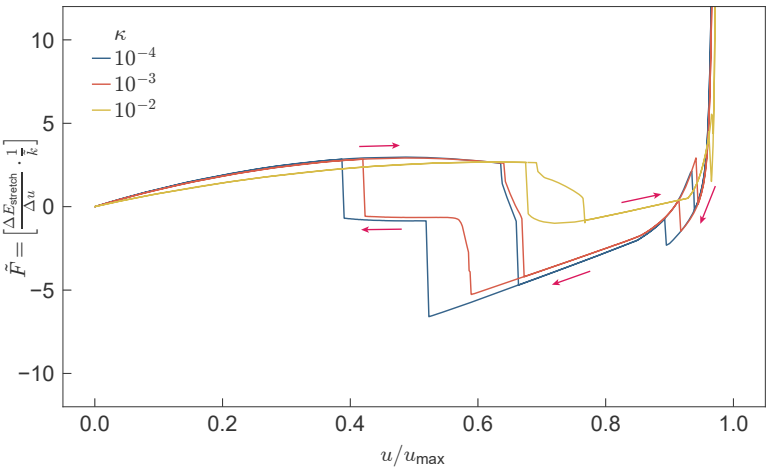

Figure B.1 | Normalized force-displacement response obtained from simulated compression tests for a prismatic structure based on a cuboctahedron, using different ratios between hinge stiffness and face stiffness. The behavior of the simulations is qualitatively similar for $\kappa = 10^{-3}$ and $\kappa = 10^{-4}$, both showing two instabilities when compressing the structure and three when returning to the initial configuration. Although not shown here, similar results are obtained for $\kappa < 10^{-4}$. However, when $\kappa = 10^{-2}$, the response changes, and only two instabilities occur during unloading. Furthermore, the minimum force increases, reducing the stability of the stable state observed for $\tilde{F} < 0$.

B.5. Hinge selection reduction

The prismatic structures studied here are highly symmetric, resulting from the underlying uniform polyhedra used as templates. Therefore, we developed a method to exploit these symmetries in order to reduce the search space to find stable states. Note that to determine unique selections of actuated hinges we consider only the edges of the internal polyhedron. In this section we will start from the polyhedron, and create a directed graph that represents the edges and their connectivity. Next, we determine the minimum distance matrix from the graph, from which we extract all principal sub-matrices that represent the hinge selections. In the remaining part of this section we explain our method in more detail, and as an example, apply it to a prismatic structure based on a triangular prism.

B.5.1. Directed graph

To determine symmetric hinge selections for the actuation of the prismatic structure, we start by constructing a graph of the internal polyhedron. Fig. B.2a shows an example of the graph belonging to a triangular prism, in which we have mapped the edges of the polyhedron to nodes in the graph. We then designate a type to each node in the graph, depending on the faces of the polyhedron that are connected to the corresponding edge, e.g., for the triangular prism there are two types: *a)* triangle-square (denoted in red) and *b)* square-square (denoted in purple).

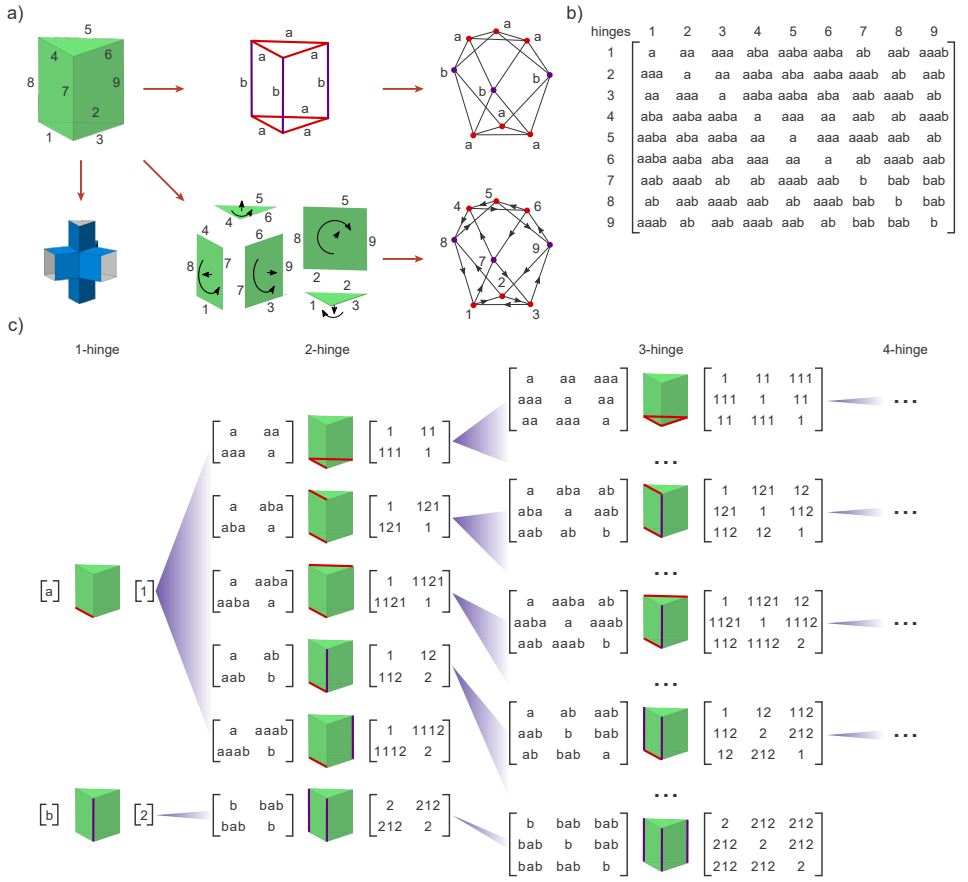

Figure B.2 | Reduction of the hinge selection by exploiting the symmetries of a prismatic structures considering only the internal hinges. a) Starting from the triangular prism that forms the basis for a prismatic structure,we number the edges and give them types depending on the connected faces. We assign a node to each edge with the same type and connect these nodes depending on their common vertices in the polyhedron to construct a graph. Additionally, to assign directions to the connections in the graph, we apply the right-hand rule to its normal. b) We determine the minimum distance between nodes. Note that instead of using the distance, we denote the path by the type of the nodes that are encountered when traveling along the path. c) We extract all principal sub-matrices that represent the hinge selections. We replace the node type by a numerical number in order to obtain the eigenvalues of the sub-matrices. In this step, symmetric hinge selections are removed by removing those that have sub-matrices with the same eigenvalues as already selected hinge combinations.

Next, we create directed connections between nodes in the graph. For this, we consider all the faces of the polyhedron, and define an outward-pointing normal such that we can follow edges of each face using the right-hand-rule. For each pair of consecutive edges a connection is created between nodes in the graph, where the direction points from the first to the second node. For example, in Fig. B.2a, the edges numbered 8, 1, 7 and 4 form a face and are consecutive according to the described method, therefore directional connections from $8 \rightarrow 1$, $1 \rightarrow 7$, $7 \rightarrow 4$ and $4 \rightarrow 8$ are created.

B.5.2. Shortest distance matrix

Once the graph is created, we compute the shortest directed distance between the nodes. We use this distance to compare all the node selections, regardless of their original location on the prismatic structure. Symmetric node selections are characterized by similar paths traveled on the graph. To compute the shortest distance matrix we first made a depth search algorithm that enumerates all the possible paths between two nodes. Note that instead of using the length of the path in the matrix, which is typically done in graph theory, we use an array of the node types passed along that path (Fig. B.2c). In order to differentiate between equal length paths, we assign a numerical value to each one depending on the types of nodes and select the smallest number for consistency.

For example, for the triangular prism the function enumerates the paths between node 1 and 3. A few of the possible paths are $1 \rightarrow 7 \rightarrow 3$, $1 \rightarrow 2 \rightarrow 3$ and $1 \rightarrow 2 \rightarrow 8 \rightarrow 5 \rightarrow 4 \rightarrow 6 \rightarrow 7 \rightarrow 3$, indicated by the node type array *(aba)*, *(aaa)* and *(aabaaaba)*, respectively. We then assign the value 1 to the node type *a* and 2 to node type *b*. Two of the paths have the same length, but the assigned number representing the paths is different. We select path *(aaa)* that has the lowest value, 111. Therefore, the path on the shortest distance matrix, at entry (1,3) in Fig. B.2c, is *(aaa)* representing the path from node 1 through node 2 to node 3.

B.5.3. Hinge selection for actuation

From the shortest distance matrix we can compute the unique hinge selections after assigning values to the paths, by considering the eigenvalues of all the principal submatrices. We start by considering actuating one hinge, and after finding all unique hinge selections, increase the number of actuated hinges by one until the total number of hinges has been reached.

First, we select one node. Since the distance between a node and itself is given by just the node type, we select one of each type. In case of the triangular prism we select nodes 1 and 7 with types *(a)* and *(b)*, respectively (Fig. B.2c). Next, we choose a second node expanding the previous selection of one node. We go through all the remaining nodes extracting the principal sub-matrices. These sub-matrices contain the information of the node types and the distance between nodes, and therefore their eigenvalues are unique to the node selection. Considering all the sub-matrices, we choose hinge selections that have different eigenvalues and remove duplication.

We repeat this strategy until all unique hinge selections have been found (Fig. B.2c). Note that we only need to consider hinge selections that contain up to half the number of nodes, given that we can simply consider the hinge selections to be reversed, i.e., replacing actuated hinges with non-actuated hinges and vice versa). For example, to choose eight nodes for a triangular prism, we inverse the one-node thus selecting nodes 2-9 and 1-6,8,9 which are the inverse of node 1 and 7, respectively.

B.6. Additional Results

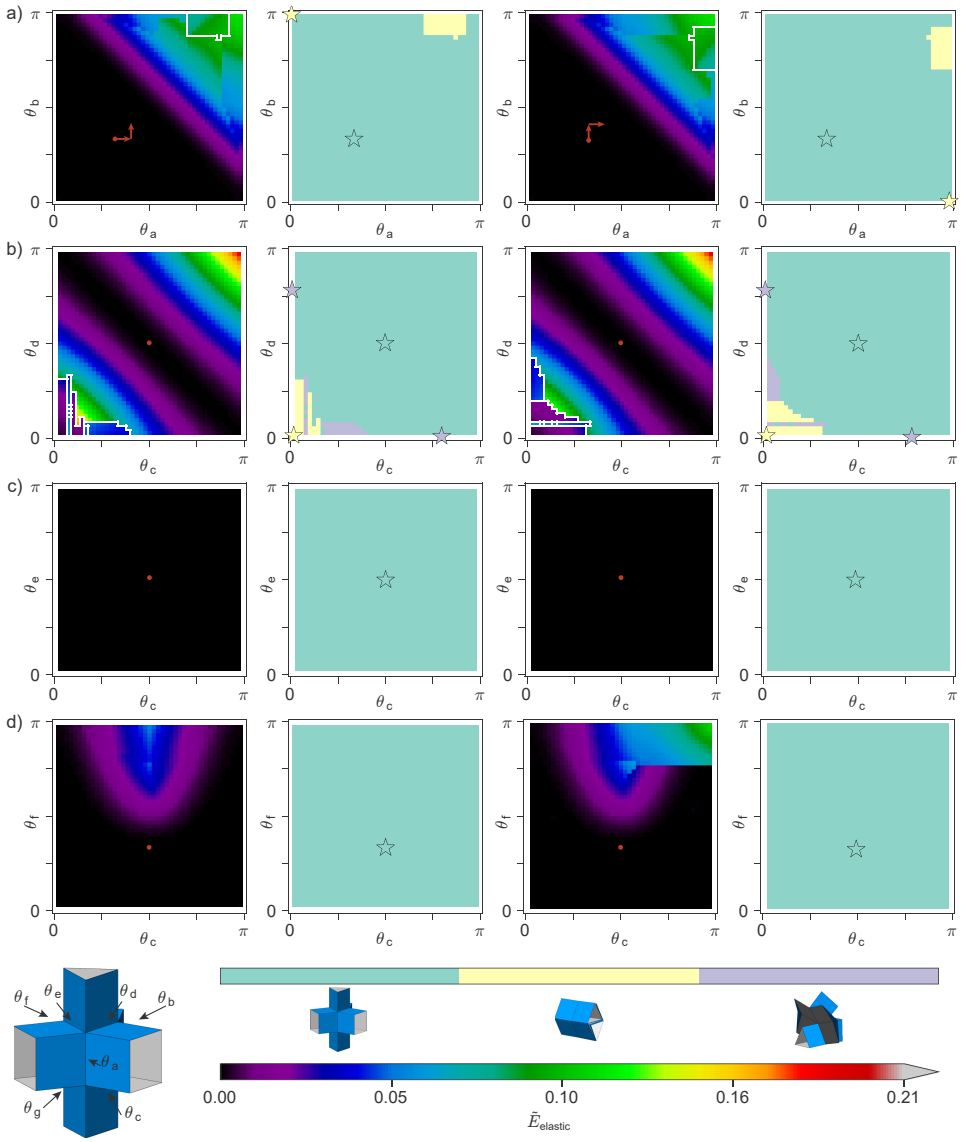

Figure B.3 | Projected energy landscapes and state diagrams for a prismatic structures based on a triangular prism. Here, we fold the structures in two steps by applying a torque to two hinges in sequence. Different projections of the energy landscape are obtained by loading the structure along a) θ_b and θ_a, b) θ_d and θ_c, c) θ_e and θ_c, d) θ_f and θ_c, e) θ_a and θ_c, and f) θ_g and θ_c. We record the elastic energy of the final state, and repeat this process for all possible combination of the fold angle values. The results are then presented as a 2D projection of the energy landscape. To show the dependency of the loading path on the final configuration, we also show the results obtained when changing the order of loading. Moreover, we relax the prismatic structure from the folded configurations to reach the local minima and obtain a state diagram. The star symbols indicate the values of the fold angles of these minima, where points in the plot relax to a star symbol with the same color.

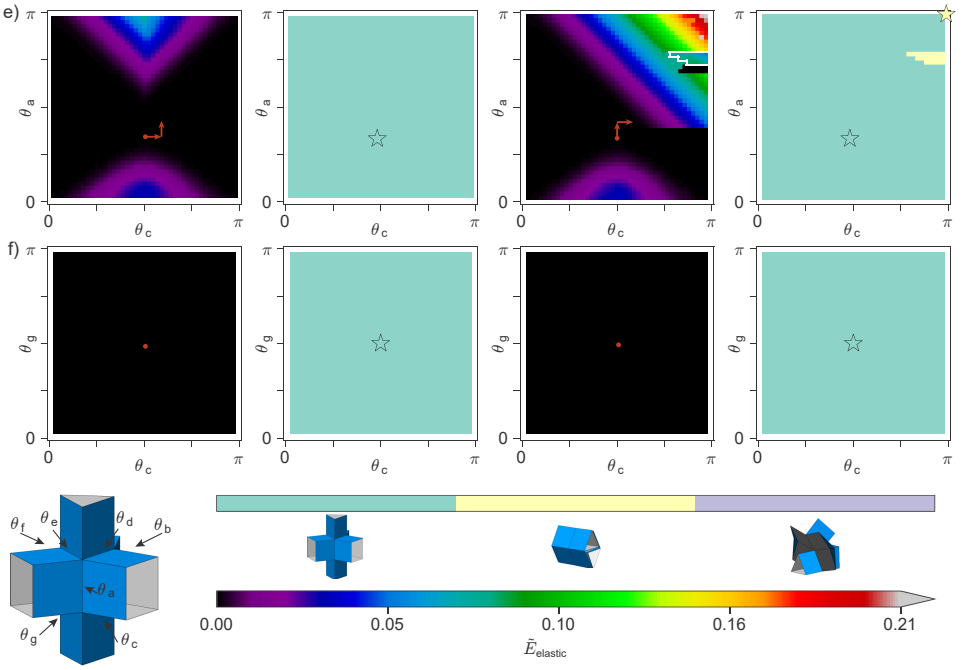

Figure B.3 | (continued) Projected energy landscapes and state diagrams for a prismatic structures based on a triangular prism. Here, we fold the structures in two steps by applying a torque to two hinges in sequence. Different projections of the energy landscape are obtained by loading the structure along a) θ_b and θ_a, b) θ_d and θ_c, c) θ_e and θ_c, d) θ_f and θ_c, e) θ_a and θ_c, and f) θ_g and θ_c. We record the elastic energy of the final state, and repeat this process for all possible combination of the fold angle values. The results are then presented as a 2D projection of the energy landscape. To show the dependency of the loading path on the final configuration, we also show the results obtained when changing the order of loading. Moreover, we relax the prismatic structure from the folded configurations to reach the local minima and obtain a state diagram. The star symbols indicate the values of the fold angles of these minima, where points in the plot relax to a star symbol with the same color.

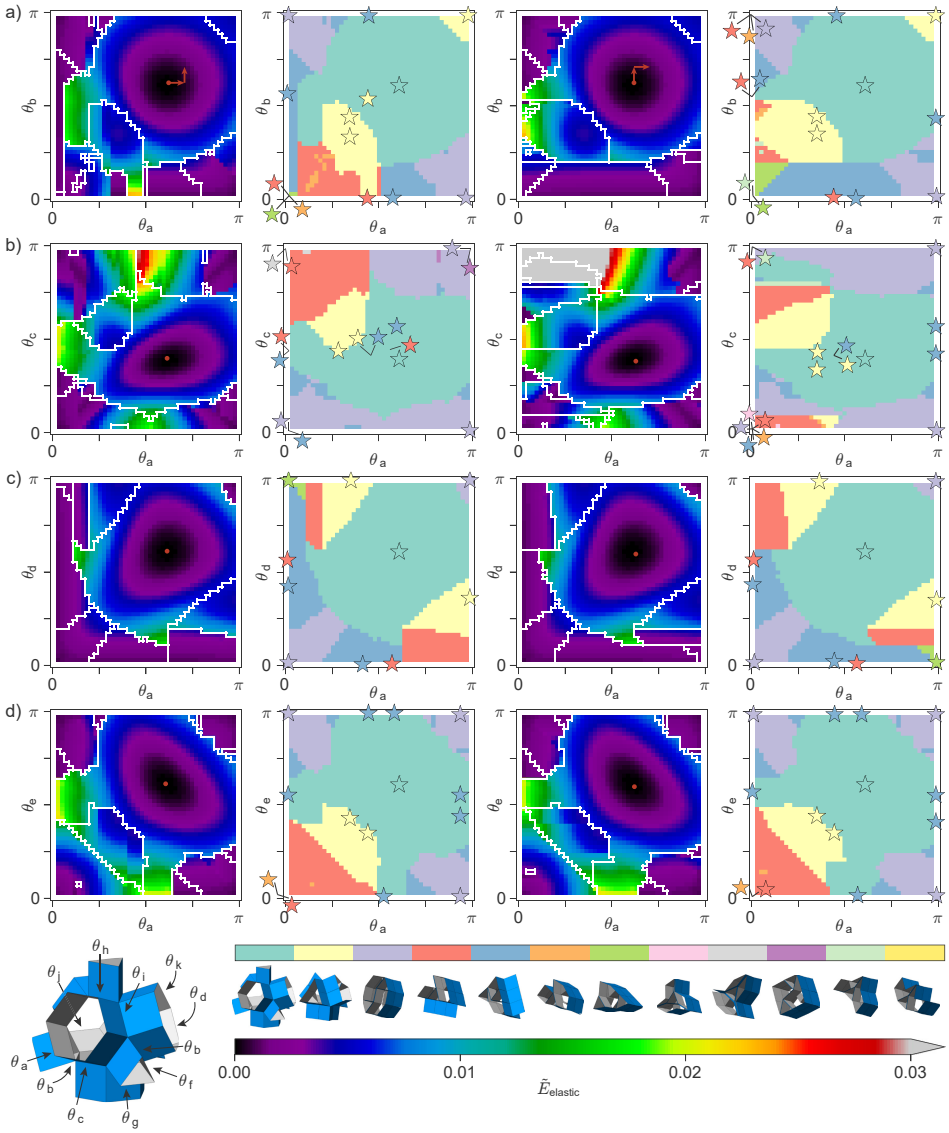

Figure B.4 | Projected energy landscapes and state diagrams for a prismatic structures based on a truncated tetrahedron. Here, we fold the structures in two steps by applying a torque to two hinges in sequence. Different projections of the energy landscape are obtained by loading the structure along a) θ_b and θ_a, b) θ_c and θ_a, c) θ_d and θ_a, d) θ_e and θ_a, e) θ_f and θ_a, f) θ_g and θ_a, g) θ_h and θ_a, h) θ_i and θ_a, i) θ_j and θ_a, j) θ_f and θ_c, and k) θ_k and θ_c. We record the elastic energy of the final state, and repeat this process for all possible combination of the fold angle values. The results are then presented as a 2D projection of the energy landscape. To show the dependency of the loading path on the final configuration, we also show the results obtained when changing the order of loading. Moreover, we relax the prismatic structure from the folded configurations to reach the local minima and obtain a state diagram. The star symbols indicate the values of the fold angles of these minima, where points in the plot relax to a star symbol with the same color.

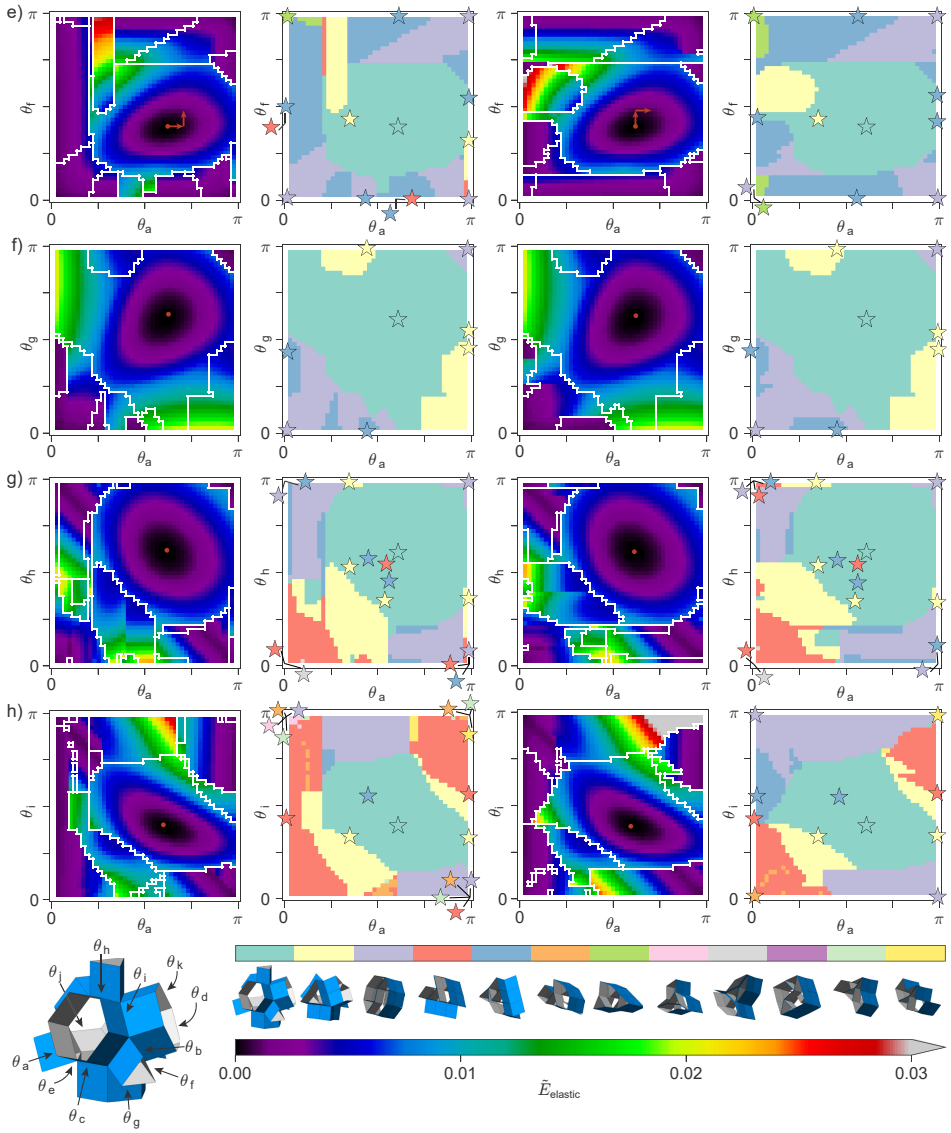

Figure B.4 | (continued) Projected energy landscapes and state diagrams for a prismatic structures based on a truncated tetrahedron. Here, we fold the structures in two steps by applying a torque to two hinges in sequence. Different projections of the energy landscape are obtained by loading the structure along a) θ_b and θ_a, b) θ_c and θ_a, c) θ_d and θ_a, d) θ_e and θ_a, e) θ_f and θ_a, f) θ_g and θ_a, g) θ_h and θ_a, h) θ_i and θ_a, i) θ_j and θ_a, j) θ_f and θ_c, and k) θ_k and θ_c. We record the elastic energy of the final state, and repeat this process for all possible combination of the fold angle values. The results are then presented as a 2D projection of the energy landscape. To show the dependency of the loading path on the final configuration, we also show the results obtained when changing the order of loading. Moreover, we relax the prismatic structure from the folded configurations to reach the local minima and obtain a state diagram. The star symbols indicate the values of the fold angles of these minima, where points in the plot relax to a star symbol with the same color.

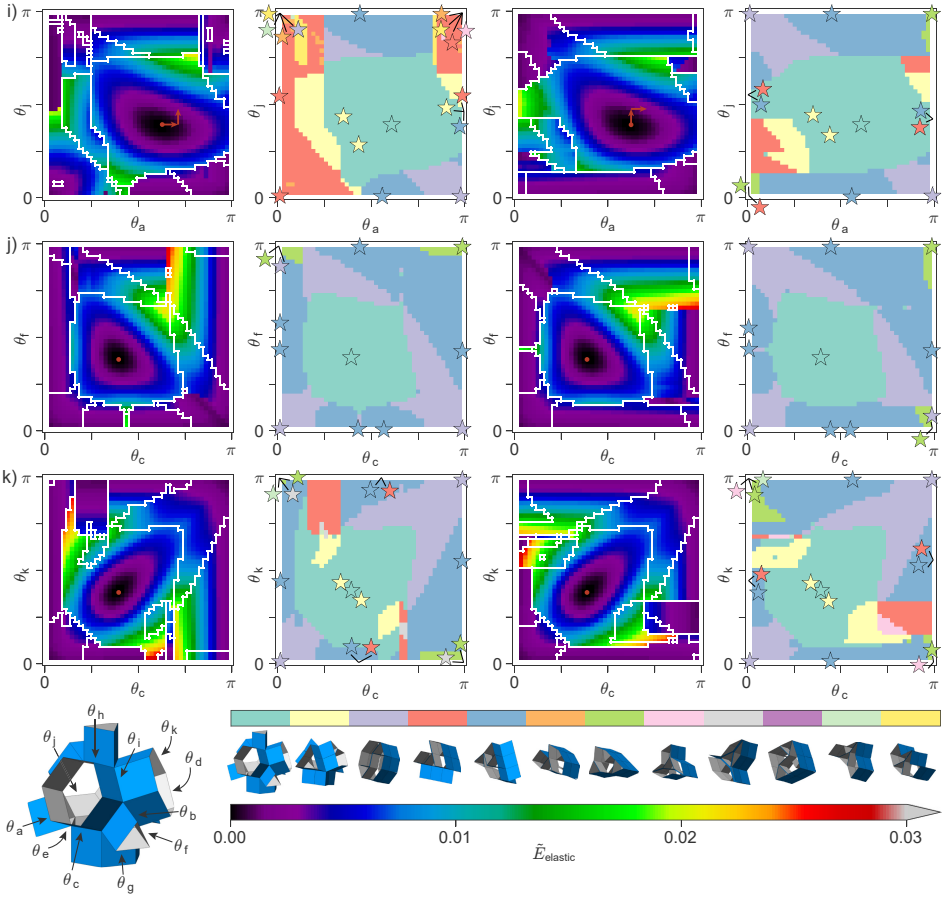

Figure B.4 | (continued) Projected energy landscapes and state diagrams for a prismatic structures based on a truncated tetrahedron. Here, we fold the structures in two steps by applying a torque to two hinges in sequence. Different projections of the energy landscape are obtained by loading the structure along a) θ_b and θ_a, b) θ_c and θ_a, c) θ_d and θ_a, d) θ_e and θ_a, e) θ_f and θ_a, f) θ_g and θ_a, g) θ_h and θ_a, h) θ_i and θ_a, i) θ_j and θ_a, j) θ_f and θ_c, and k) θ_k and θ_c. We record the elastic energy of the final state, and repeat this process for all possible combination of the fold angle values. The results are then presented as a 2D projection of the energy landscape. To show the dependency of the loading path on the final configuration, we also show the results obtained when changing the order of loading.Moreover, we relax the prismatic structure from the folded configurations to reach the local minima and obtain a state diagram. The star symbols indicate the values of the fold angles of these minima, where points in the plot relax to a star symbol with the same color.

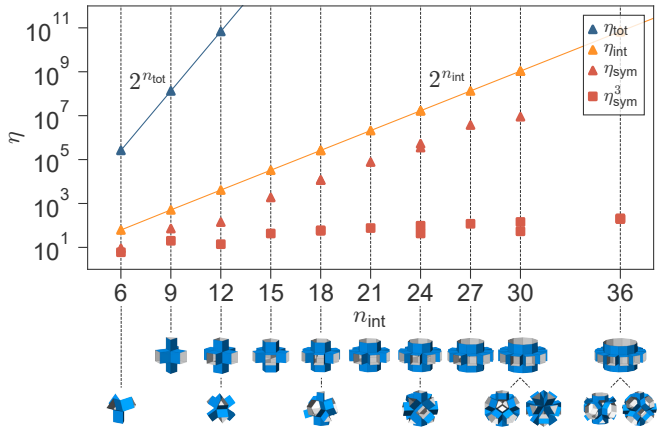

Figure B.5 | Total number of possible hinge combinations for various prismatic structures. Starting from considering both internal and external hinges (blue triangles), the amount of combinations can be reduced by only considering the internal hinges (yellow triangles). Further reductions can be made by using our custom algorithm based on directed graphs to remove symmetric combinations (red triangles), and by only considering combinations up to three hinges (red squares).

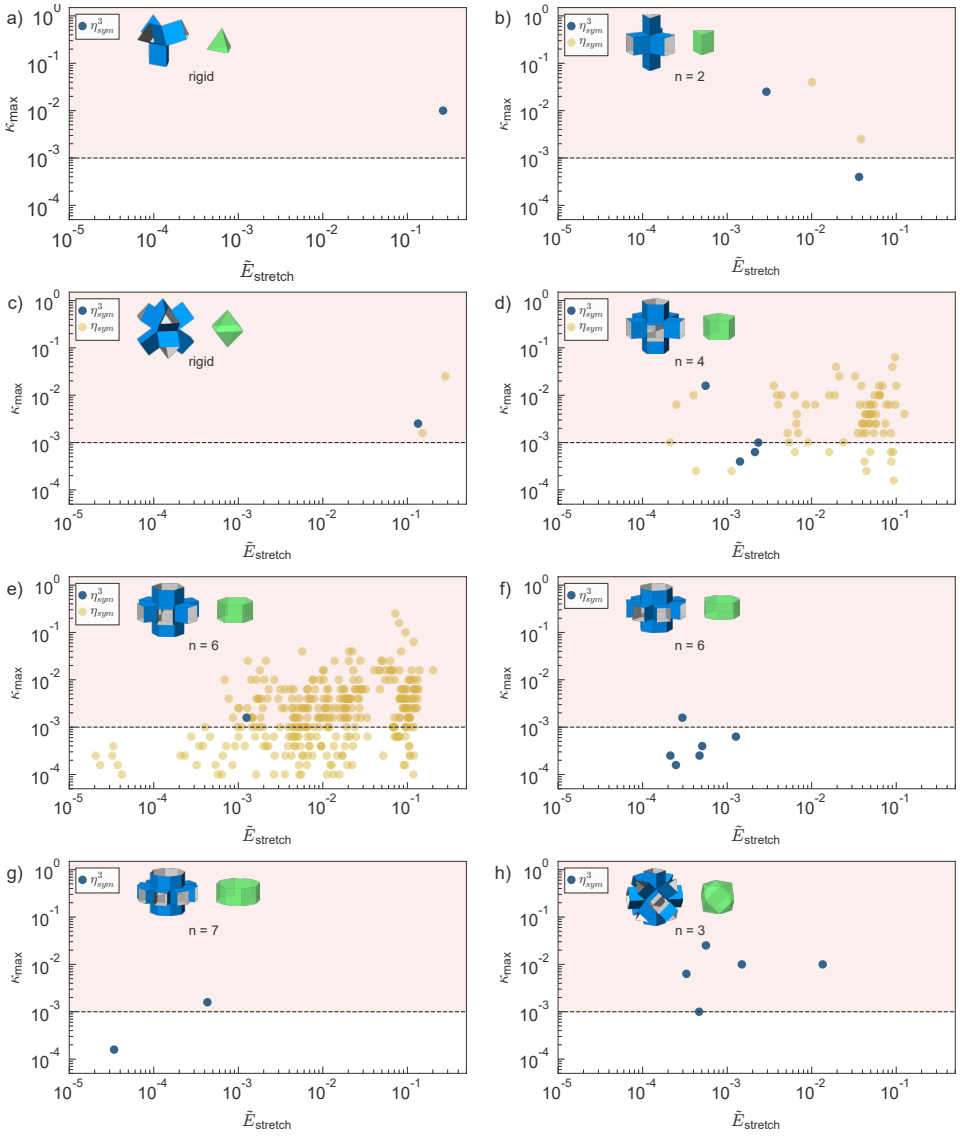

Figure B.6 | Normalized stretch energy ($\tilde{E}_{\text{stretch}}$) and maximum stiffness ratio (κ_{max}) for the obtained unique stable states found with our numerical algorithm for multiple prismatic structures. Additionally we mention the amount of degrees of freedom (n) for each structure or if it is rigid, adapted from [54]. For prismatic structures based on a a) tetrahedron, b) triangular prism, c) octahedron, d) pentagonal prism, and e) hexagonal prism, we considered all unique hinge combinations to find stable states, while for prismatic structures based on a f) heptagonal prism g) octagonal prism, h) cuboctahedron, i) nonagonal prism, j) decagonal prism, k) dodecahedron, l) dodecagonal prism, m) truncated cube, n) truncated octahedron, o) rhombicuboctahedron, and p) truncated cuboctahedron, we considered combinations up to a maximum of three hinges.

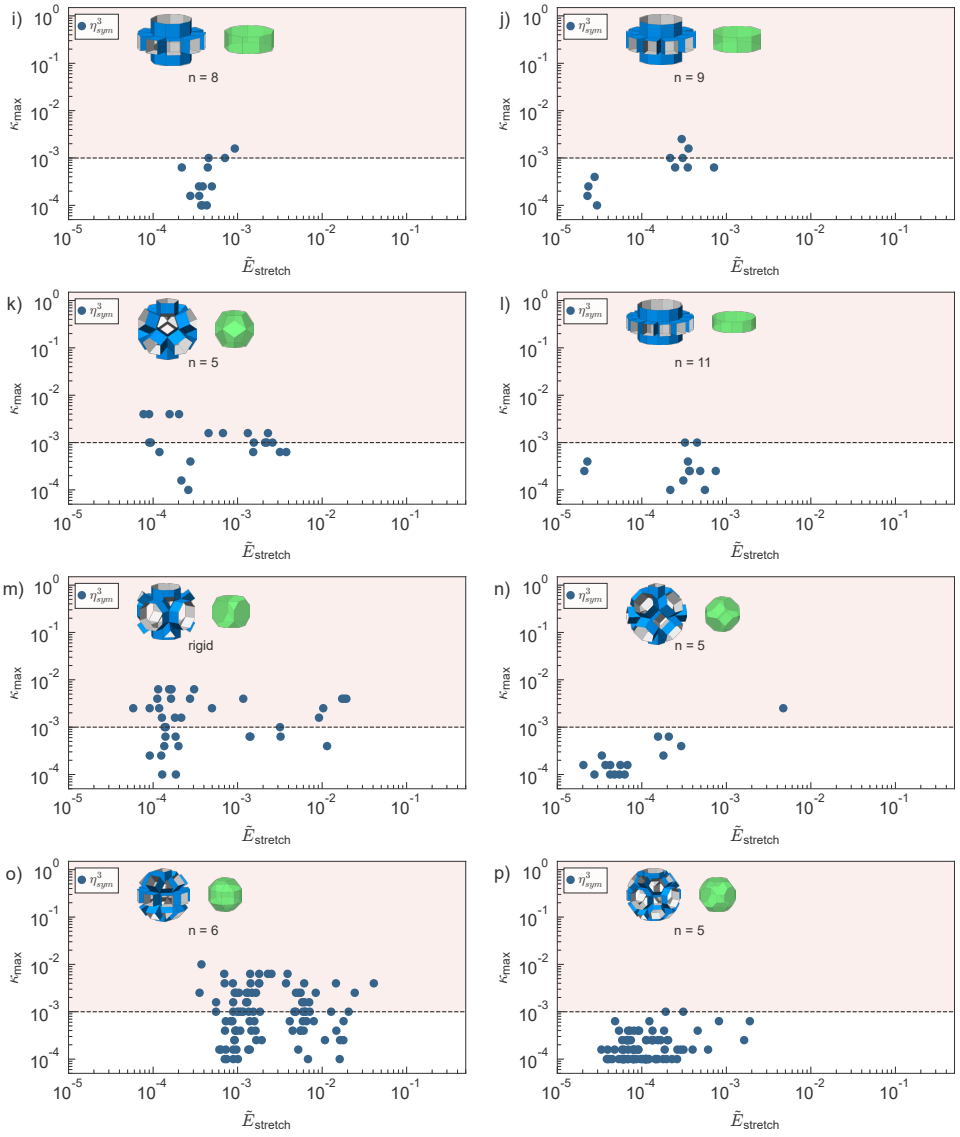

Figure B.6 | (continued) Normalized stretch energy ($\tilde{E}_{\text{stretch}}$) and maximum stiffness ratio (κ_{max}) for the obtained unique stable states found with our numerical algorithm for multiple prismatic structures. Additionally we mention the amount of degrees of freedom (n) for each structure or if it is rigid, adapted from [54]. For prismatic structures based on a a) tetrahedron, b) triangular prism, c) octahedron, d) pentagonal prism, and e) hexagonal prism, we considered all unique hinge combinations to find stable states, while for prismatic structures based on a f) heptagonal prism g) octagonal prism, h) cuboctahedron, i) nonagonal prism, j) decagonal prism, k) dodecahedron, l) dodecagonal prism, m) truncated cube, n) truncated octahedron, o) rhombicuboctahedron, and p) truncated cuboctahedron, we considered combinations up to a maximum of three hinges.

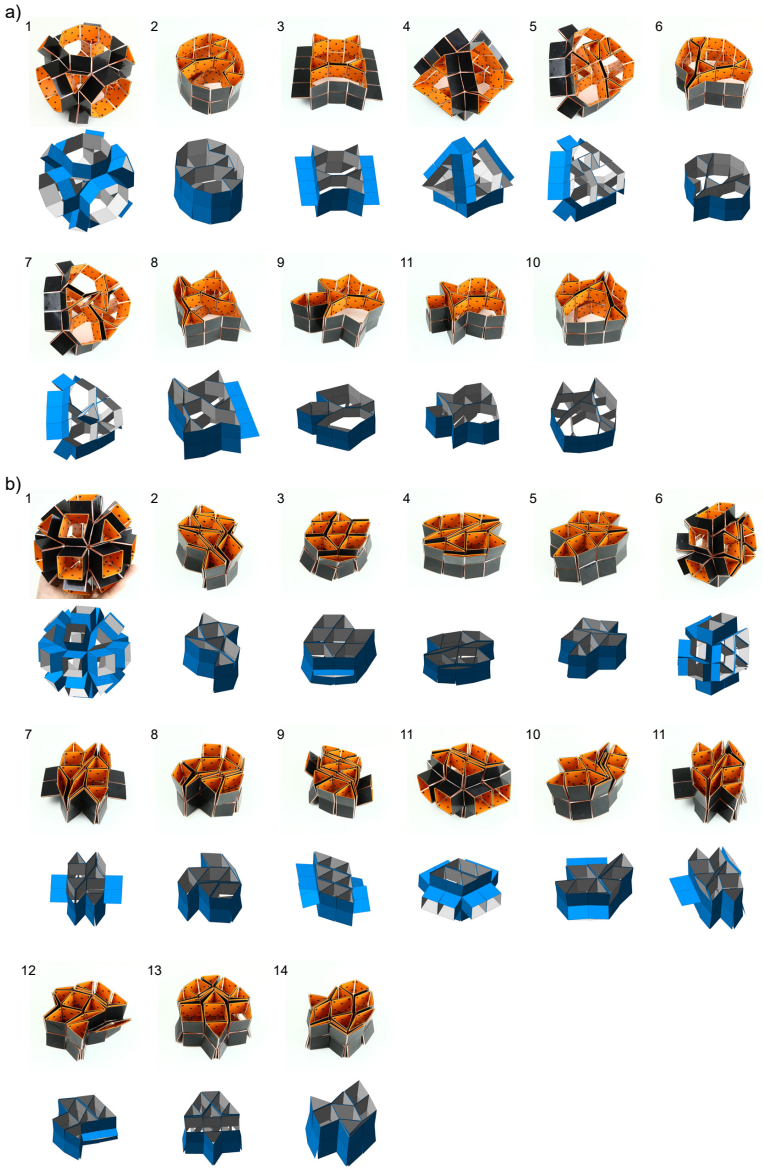

Figure B.7 | Comparison of selected stable states found with our numerical algorithm (Fig. B.6) and experiments for two prismatic structures based on a) a truncated cube and b) a rhombicuboctahedron.

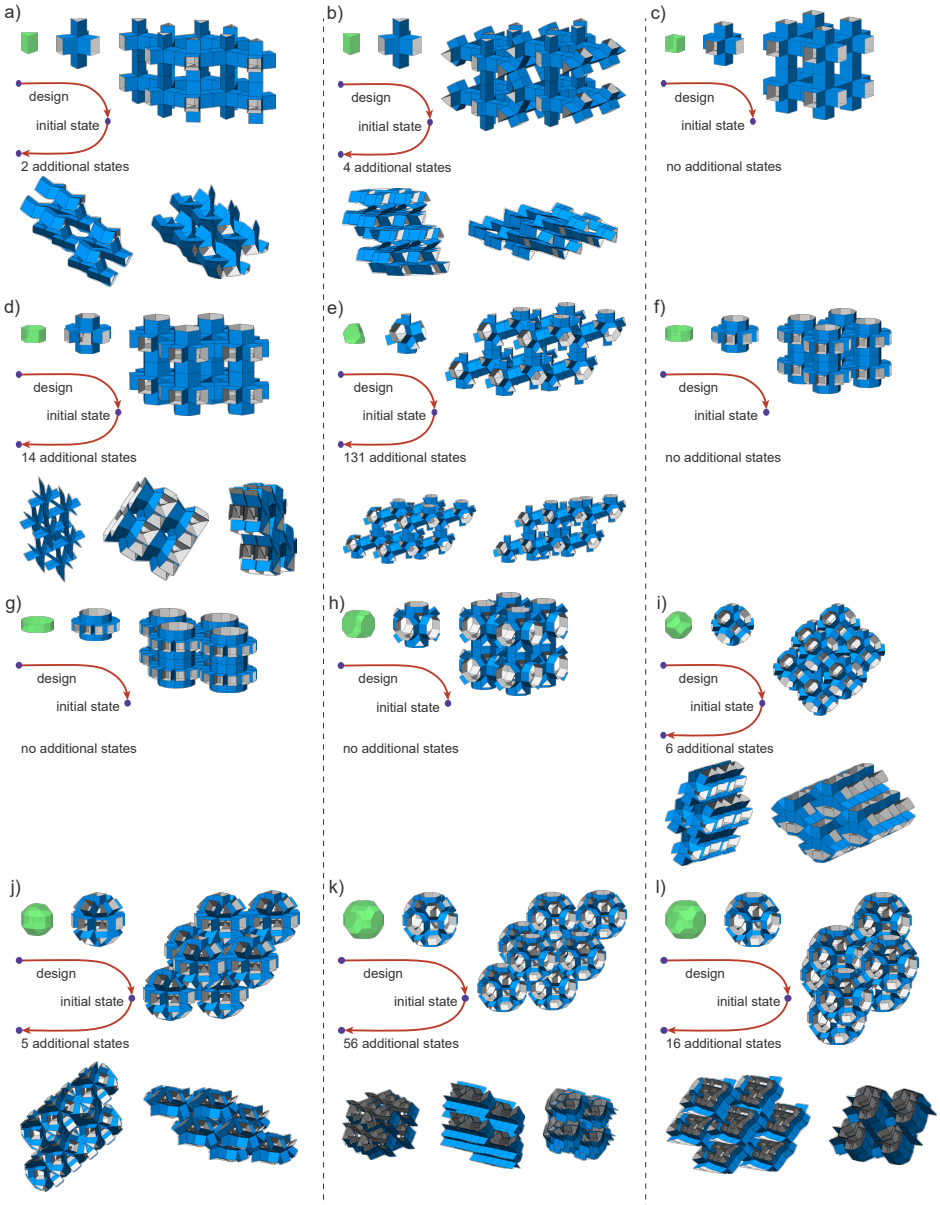

Figure B.8 | Mechanical metamaterials based on cubic arrays of prismatic structures and their unique stable states found with our numerical algorithm. These metamaterials are assembled from prismatic structures based on a) and b) triangular prisms, c) cubes, d) hexagonal prisms, e) truncated tetrahedrons, f) octagonal prisms, g) dodecagonal prisms, h) truncated cubes, i) truncated octahedrons, j) rhombicuboctahedrons, and k) and l) truncated cuboctahedrons. For most of the metamaterials a selection of the obtained stable states are shown.

C

Appendix: From rigid to amorphous folding behavior in origami with bistable hinges

Based on: Iniguez-Rabago, A., Overvelde, J.T.B., *From rigid to amorphous folding behavior in origami-inspired metamaterials with bistable hinges.* PRL. (In review)

C.1. Experiments

C.1.1. Prototype fabrication

To fabricate bistable hinge prototypes, we assembled each face from two 3D-printed (PLA, Ultimaker 3) lego-like building blocks of size 37 × 37 × 0.5mm (Fig. C.1a). Between these blocks, we clamped both flexible hinges and pre-tensioned springs, that are laser cut from a silicon rubber sheet (Fig. C.1a). We fabricated the hinges using silicon sheets of 0.5 mm thickness, with width (defined as distance between faces) equal to 4 mm. Moreover, for the spring we varied the thickness t_{spr} as well as the rest length l_{spr} to change the bistable behavior. Note that due to the combination between finite hinge size and the compression applied by the pre-tensioned springs, the hinges can have additional rotation that leads to an out-of-plane displacement (Fig. C.1b), that we do not account for in our numerical model.

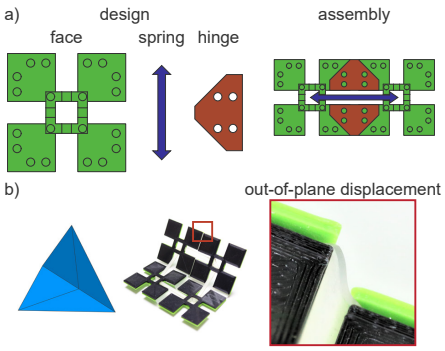

Figure C.1 | a) Used components to build a bistable hinge (face, spring and hinge) and a schematic of the assembly. b) Additional deformation arising from the interplay between the soft hinge and the spring. It can favor certain deformations that are not accounted for in our numerical model.

C.1.2. Torque measurement

We used a torsional testing machine (Instron MT1-E1) to obtain the angle versus moment response of the hinges. We applied a cyclic rotation, starting from the flat state ($\theta = 0$) (Fig. C.2a) and moving to $\theta_{max} \approx 0.6\pi$ (Fig. C.2b). Then we rotated the hinge to $-\theta_{max}$ to obtain the torque response (Fig. C.2c), after which we moved it back to the flat state to start the cycle again (Fig. C.2d). We repeated this cycle seven times for 14 hinges with different spring parameters. The average of the last five cycles are shown in Fig. C.3 for all the tested hinge parameters, where the thickness of the curve represents the standard deviation.

C.1.3. Double-well energy fit

To fit our experimentally measured response of the bistable hinges to the model described by Eq. 5.1, we first need to obtain a angle versus moment relation. For this we

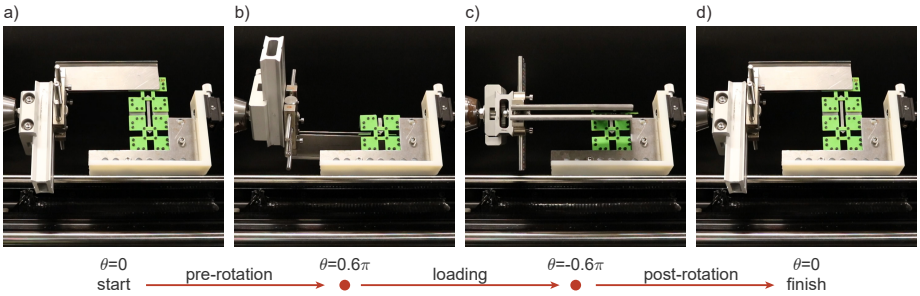

Figure C.2 | Experimental setup to measure the behavior of our bistable hinges. a) The hinge was placed flat on the torsional test machine ($\theta = 0$). b) We then performed a pre-rotation to place the hinge with an angle $\theta = 0.6\pi$, before we c) started to load the hinge to obtain the torque angle relation. d) After reaching $\theta = -0.6\pi$ we stopped and performed an additional post-rotation to go back to the initial position ($\theta = 0$).

use

$$T = \frac{dE_{\mathrm{h}}}{d\theta} = \frac{4k_{\mathrm{h}}}{\Theta^4}\theta(\theta^2 - \Theta^2) + c, \tag{C.1}$$

where T is the torque, E_h is the hinge energy. In this model the fitting parameters are given by c (a momentum adjustment parameter), k_{h} and Θ. The fitting is done using a non-linear least squares regression on the average torque respond measured for each angle, implemented in *Python* by the *curv_fit* function of the *scipy* package. Furthermore, the function returns the estimated covariance matrix of the parameters. By taking the square root of the diagonals of this matrix, we obtain the standard deviation error of each fitted parameter.

C.2. Clustering algorithm to identify stable states

In order to identify the stable states of a single vertex, we use the hinge angles of the four hinges (converged results from the elastic energy minimization Fig. C.4a) as input for a two step clustering process. First, the angles are pre-processed to avoid misidentification of symmetric states by rotating or mirroring the vertex. The four angles are then clustered using a *Density-Based Spatial Clustering of Applications with Noise* (DBSCAN) [128] algorithm that can identify non-uniform clusters. We use a maximum distance of 0.1 rad and a minimum number of five points to make a cluster. We do this first step for all different parameters that we scan (κ and Θ). For each cluster we extract the mean value of the angles (sub-states) and delete the non clustered points (outliers), as these represent less than 1% of all simulations per parameter selection as shown in Fig. C.4b.

All the identified stable states lie on 12 different axes in a 4D space spanned by the hinge angles of the four hinges. These axes correspond to the value and sign of the hinge angles and represent the different orientations that the stable state can have. We found that *(i)* the Fold state lies on top of the main branches of the rigid origami model $(x, 0, x, 0)$ and $(0, x, 0, x)$ where the value of x depends on Θ. All the *(ii)* Dome and *(iii)* Saddle stable states lie on (x, x, x, x) and $(x, -x, x, -x)$, respectively. *(iv)* The Miura-ori stable

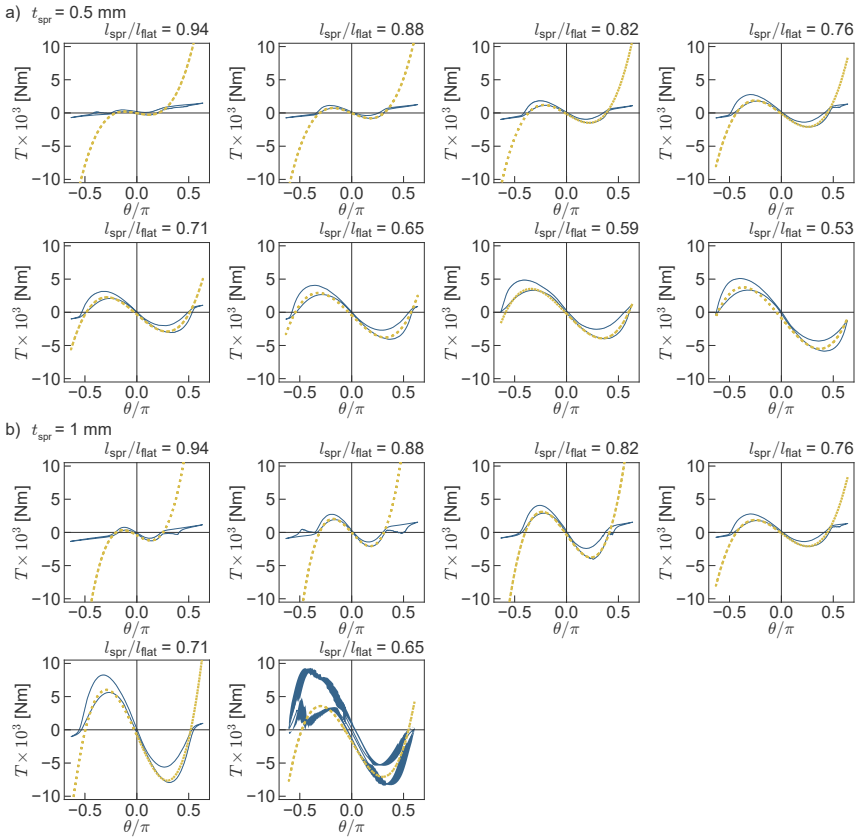

Figure C.3 | Average torque T angle θ response obtained in experiments by cyclic loading (showing the average of the last five out of seven cycles, with standard deviation as the thickness of the line) of a hinge with a) $t_{spr} = 0.5\,\text{mm}$ and b) $t_{spr} = 1\,\text{mm}$. The fitting of the model where we used $T = dE_h/d\theta$ is indicated as the dotted line.

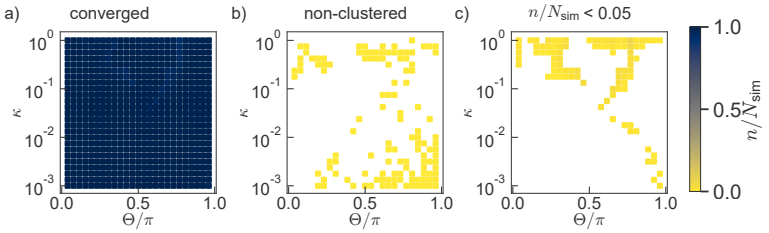

Figure C.4 | Convergence of simulations and occurrence of stable states for a 4-vertex. Number of simulations (n/N_{sim}) from a total of $N_{sim} = 1000$ simulations for each parameter selection of κ and Θ that a) converge, b) are outliers from the clustering algorithm and c) occur in less than $n/N_{sim} < 0.05$.

state can be found on six axes (π,x,π,x), (x,π,x,π), $(x,x,x,-x)$, $(x,x,-x,x)$, $(x,-x,x,x)$ and $(-x,x,x,x)$, where the first two branches are the sub-branches of the rigid origami model.

For the second step of the clustering algorithm, we exploit the classification of the four different stable states. We determine the distance of each vertex (a 4D point whose dimensions are the angles of its hinges) to each of the axes, and mark the stable state with the closest axis. For the single vertex we show only the clusters with at least 5% of the simulations (Fig. C.4c). This identifies the final stable state.

C

C.3. Crystal characterization

C.3.1. Identifying crystals and crystal defects

We use the four stable states of the 4-vertex found with the clustering algorithm to characterize metamaterials, and to obtain their corresponding state matrix ($n \times n$) as shown by the example in Fig. C.5a. In this matrix, each entry represents the stable state of the corresponding vertex, where we also consider the orientation of this state in the material. Here, the Dome state (represented by 0) and the Saddle state (1) have one possible orientation, the Miura-ori has four possible orientations (2,3,4,5) and the Fold state has two orientations (6,7).

Next, to identify the patterns and potential defects, we obtain every 2×2 submatrix from the state matrix. We rotate and transpose these submatrices to order the entries. We represent each template by a letter (a for mcDS, b for DSt, c for MDinter, d for mcAM, etc.) to create a crystal matrix of size $(n-1)\times(n-1)$. From this crystal matrix we can determine if defects exists in the material, in order to differentiate between monocrystalline and polycrystalline materials.

C.3.2. Determining the crystal size

Finally, we want to determine the average crystal size. In order to do so, we remove all entries that represent defects from the crystal matrix, marking crystals by T and defects by F. To the resulting matrix we apply the same DBSCAN algorithm as before, with minimum

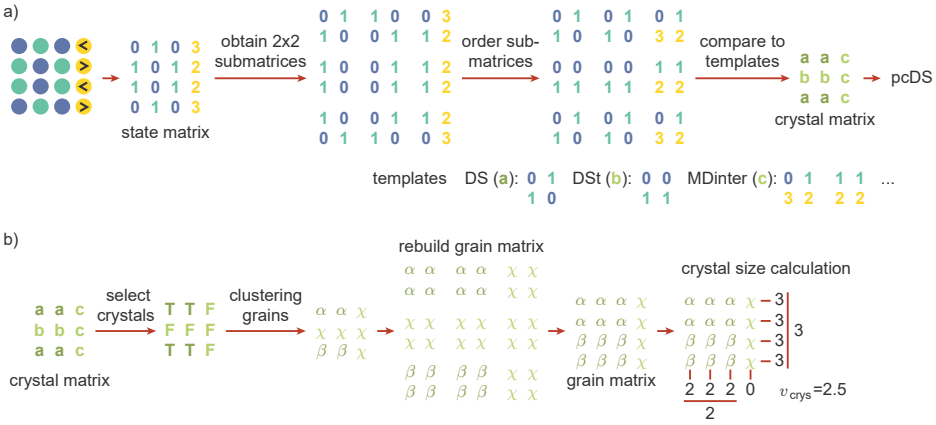

Figure C.5 | Method of identifying defects and calculating crystal sizes, illustrated with an example. a) Steps used to identifying the defects and crystal types applied to a 4×4 material. b) Steps used to determine the crystal size for the same 4×4 material.

C

cluster size equal to one and a maximum distance equal to one. This clustering algorithm gives us the different grains that the material has with a grain identifier symbol, where defects are indicated by χ and the other symbols represent unique crystal clusters. As such, this step transforms the crystal matrix by changing the entry of the crystal type to the corresponding grain identifier.

Next, we build a grain matrix of size $n \times n$ from the transformed crystal matrix, by assigning a 2×2 matrix to each entry, and overlapping these matrices to form the grain matrix. Each entry of this matrix represents a vertex and its symbol a grain identifier. For each two overlapping matrices we choose only entries that identify a grain $(\alpha, \beta, \gamma, \ldots)$ and since there is always a crystal defect (χ) between grains, the overlap only removes defects. Finally, for each row and each column of the grain matrix we count the grain identifiers using a intercept method [129]. We take the average number that an identifier appears for each row and each column, and average this value for the rows and columns separately. The average linear crystal size is then found by averaging the average crystal size for the columns and rows. An example of the whole process is shown in Fig. C.5b.

C.4. Additional Results

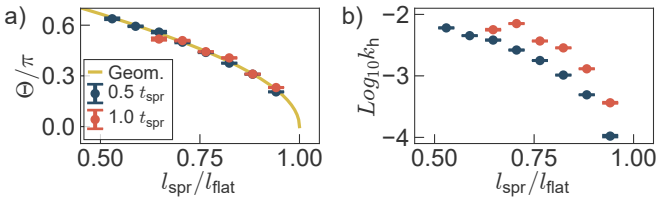

Figure C.6 | Fit of the a) rest angle Θ and the b) energy barrier k_h for different l_{spr} and t_{spr}, where the errorbars are determined from the diagonals of the covariance matrix. The line indicates a purely geometrical relation between the hinge parameters and the spring length.

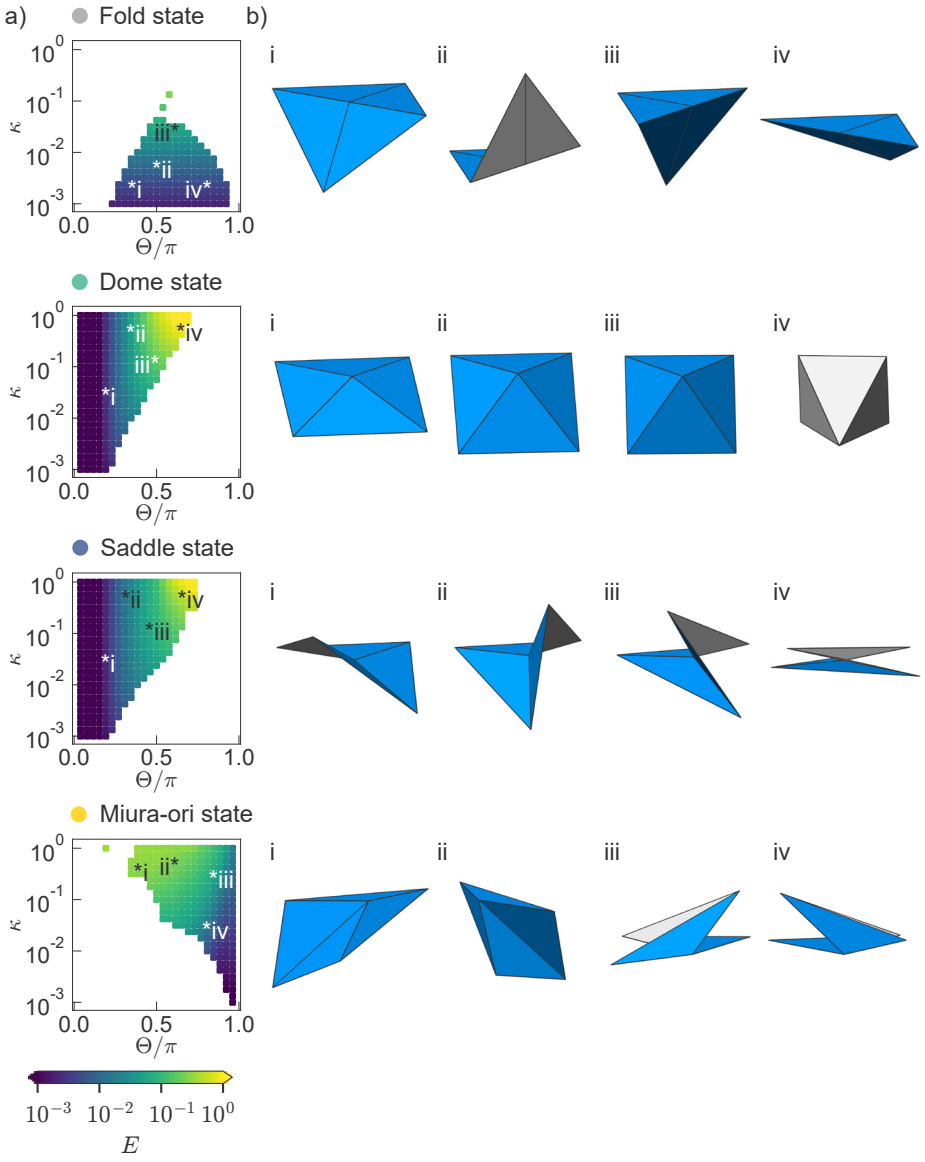

Figure C.7 | a) Elastic energy of a single vertex for the four different stable states against the two control parameters Θ and κ. b) Additional deformed states of the vertices showing the four stable states for different parameters marked in a).

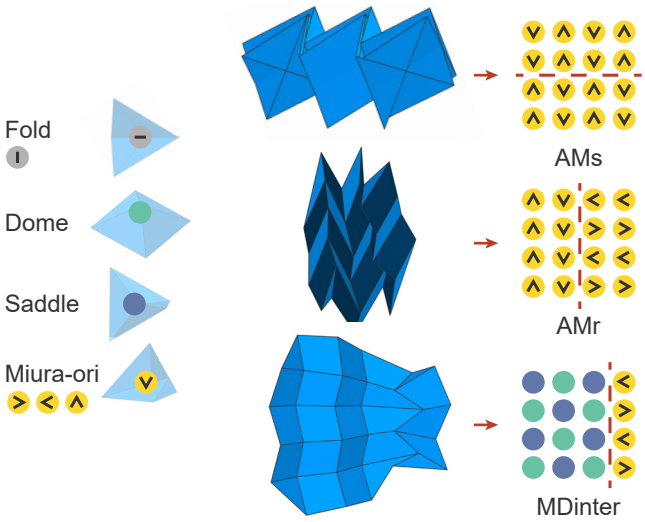

Figure C.8 | Additional metamaterials showing the different crystal defects with their state matrix representation, that we obtain from the simulations of a 4×4 material with parameters $\kappa = 10^{-1.5}$ and $\Theta = 0.25\pi$ or 0.75π. Note that the AMs defect results in non-adjacent face crossing, not accounted for in our model.

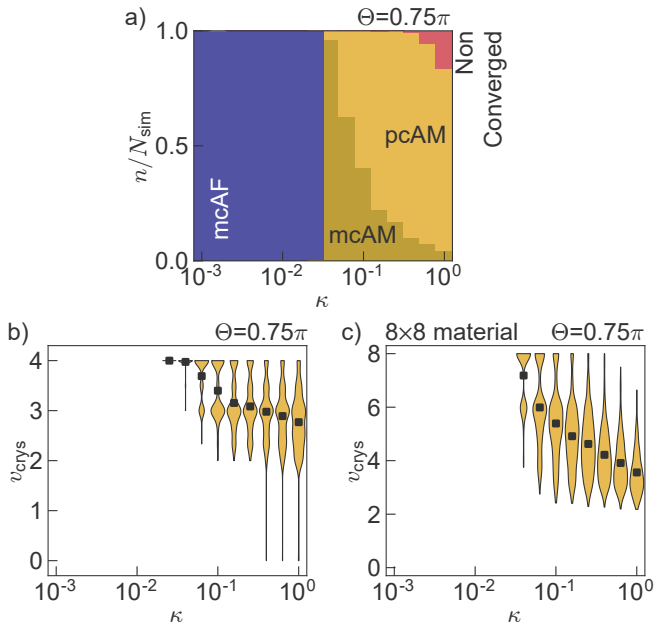

Figure C.9 | a) Percentage of simulations (n/N_{sim}) for which the stable state is either monocrystaline or polycrystaline, indicated for each crystal type with $\Theta = 0.75\pi$. Distribution of crystal size (υ_{crys}) against κ for b) a 4×4 and c) a 8×8 material. The black dots represent the mean of the distribution.

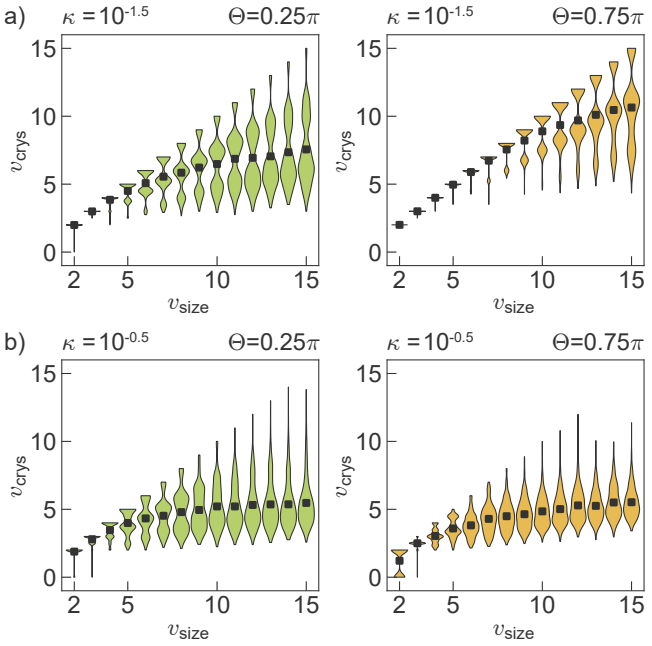

Figure C.10 | Average crystal size (υ_{crys}) for metamaterials with size $\upsilon_{\text{size}} \times \upsilon_{\text{size}}$ with parameters a) $\kappa = 10^{-1.5}$ and b) $\kappa = 10^{-0.5}$, and $\Theta = 0.25\pi$ or $\Theta = 0.75\pi$. The black dots represent the mean of the distribution.

D

Appendix: Supplemental movies

In this appendix you can find the description of all the supplemental movies of this thesis. To watch these movies you can access the following link bit.ly/SupMovies or scan this QR-code that redirects to a folder containing all the movies.

Figure D.1 | QR-code that redirects the reader to a folder containing all the supplemental movies

Movie 1.1: Experimental demonstration of mode deformation of a Sarrus linkage metamaterial. According to the rigid origami model, this metamaterial deforms only along the compression mode, nevertheless in experiments we see that deformation along a second mode, the bend mode, is also possible.

Movie 1.2: Numerical simulations of the mode deformation of a Sarrus linkage metamaterial. By controlling a set of angles we can deform this metamaterial along the compression and bend mode.

Movie 3.1: Soft and pseudo soft modes of prismatic structures. Deformation of the soft and pseudo soft modes for the structures based on a cube and a truncated tetrahedron. These modes are obtained follow a thin sheet origami approximation, i.e., $k_h \ll k_b \ll k_s$.

Movie 3.2: Interacting modes of a structure based on a square. Deformation of interacting modes which energy distribution depends on the stiffness regime for regime I ($k_h \ll k_b \ll k_s$) and III ($k_h \ll k_s \ll k_b$).

Movie 3.3: Soft and pseudo soft modes in reduced models. Deformation of the soft modes for a structure based on a cube in both models, stretch constraint model and bend constraint model. Deformation of the pseudo soft modes for a structure based on a truncated tetrahedron in the bend constraint model.

Movie 4.1: Experimental and numerical compression test. We perform a comparison between an experimental and numerical compression test applied to a prismatic structure based on a cuboctahedron. The simplified model used in simulations shows good qualitative agreement with experiments performed on a prototype made from 3D printed faces (PLA) connected by flexible hinges (Mylar).

Movie 4.2: Projected energy landscape and state diagram. We select three folding sequences and project them on the energy landscape of a prismatic structure based on a triangular prism. To obtain each folding sequence we fold two hinges consecutively, after which we let the structure relax to a stable state. By repeating this approach, we find a state diagram of the stable states that can be achieved.

Movie 4.3: Stable States of prismatic structures. We verify the stable states found

for the prismatic structures based on a truncated tetrahedron and a cube. While many of the stable states of the prismatic structure based on a truncated tetrahedron can be achieved using a prototype with Mylar hinges, some states are not stable and relax to other configurations. Furthermore, for the prismatic structure based on a cube most of the stable states can only be achieved when replacing the Mylar hinges with more stretchable silicon hinges.

Movie 4.4: Multistable metamaterials. We show the results of our numerical method applied to multistable metamaterials that are based on cubic tessellations of prismatic structures based on a cuboctahedron and a rhombicuboctahedron. The simulation of the metamaterials behavior was performed by applying periodic boundary conditions to the individual building block in addition to the local actuation patterns that previously resulted in stable configurations for the unit cell.

Movie 4.5: Varying the multistable behavior in a metamaterial. We control the multistability of a metamaterial based on a cuboctahedron by adjusting κ. In experiments, this can be achieved by changing the hinge thickness. When we build our prototypes with Mylar hinges with a thickness of 50 ţm, the metamaterial exhibits multiple stable states. However, when building the material with 125 ţm thick Mylar hinges it is no longer multistable.

Movie 4.6: Pneumatic actuation of a prismatic structure. We apply pneumatic actuation to a prismatic structure based on a truncated tetrahedron. We use pneumatic pouches to actuate two hinges of the structure individually, and are able to deform the structure into four stable states.

Movie 5.1: Experiments on a single vertex and a 4×4 metamaterial. We manually flatten the structures by forcing it down on a surface, after which we quickly release them to allow the structures to relax to their stable state. We performed these experiments on vertices and metamaterials with low ($\Theta = 0.3\pi$) and high ($\Theta = 0.6\pi$) rest angle. The single vertex relaxes to the Fold state and the Miura-ori state for low and high Θ, respectively. The metamaterial with low Θ relaxes only to the mcAF crystal, while the metamaterial with high Θ has a probability to fold in either one of the mcAM, AMt, AMr, AMs or MFinter states.

Bibliography

[1] N. Robinson, *The Origami Bible: A Practical Guide to the Art of Paper Folding*. Collins & Brown, 2004.

[2] M. Friedman, *A history of folding in mathematics: mathematizing the margins*, vol. 59. Birkhäuser, 2018.

[3] A. Gönenç Sorguç, I. Hagiwara, and S. Arslan Selçuk, "Origamics in Architecture: A Medium of Inquiry or Design in Architecture," *Metu Journal of the Faculty of Architecture*, vol. 26, no. 2, pp. 235–247, 2009.

[4] P. M. Reis, F. L. Jiménez, and J. Marthelot, "Transforming architectures inspired by origami," oct 2015.

[5] I. Meissner and E. Möller, *Frei Otto: A Life of Research, Construction and Inspiration*. Edition Detail, 2015.

[6] N. Heidari Matin and A. Eydgahi, "Technologies used in responsive facade systems: a comparative study," *Intelligent Buildings International*, 2019.

[7] J. J. Park, P. Won, and S. H. Ko, "A Review on Hierarchical Origami and Kirigami Structure for Engineering Applications," jan 2019.

[8] J. Rogers, Y. Huang, O. G. Schmidt, and D. H. Gracias, "Origami MEMS and NEMS," *MRS Bulletin*, vol. 41, pp. 123–129, feb 2016.

[9] E. A. Peraza-Hernandez, D. J. Hartl, R. J. Malak, and D. C. Lagoudas, "Origami-inspired active structures: A synthesis and review," *Smart Materials and Structures*, vol. 23, no. 9, 2014.

[10] S. Felton, M. Tolley, E. Demaine, D. Rus, and R. Wood, "A method for building self-folding machines," *Science*, vol. 345, pp. 644–646, aug 2014.

[11] H. Suzuki and R. J. Wood, "Origami-inspired miniature manipulator for teleoperated microsurgery," *Nature Machine Intelligence*, vol. 2, pp. 437–446, aug 2020.

[12] P. Wang, T. A. Meyer, V. Pan, P. K. Dutta, and Y. Ke, "The Beauty and Utility of DNA Origami," mar 2017.

[13] J. Sun, C. Liu, and B. Bhushan, "A review of beetle hindwings: Structure, mechanical properties, mechanism and bioinspiration," jun 2019.

[14] J. A. Faber, A. F. Arrieta, and A. R. Studart, "Bioinspired spring origami," *Science*, vol. 359, no. 6382, pp. 1386–1391, 2018.

[15] K. Saito, S. Nomura, S. Yamamoto, R. Niyama, and Y. Okabe, "Investigation of hindwing folding in ladybird beetles by artificial elytron transplantation and microcomputed tomography," *Proceedings of the National Academy of Sciences of the United States of America*, vol. 114, pp. 5624–5628, may 2017.

[16] S. Hernández-Ainsa, N. A. Bell, V. V. Thacker, K. Göpfrich, K. Misiunas, M. E. Fuentes-Perez, F. Moreno-Herrero, and U. F. Keyser, "DNA origami nanopores for controlling DNA translocation," *ACS Nano*, vol. 7, pp. 6024–6030, jul 2013.

[17] E. M. Arkin, M. A. Bender, E. D. Demaine, M. L. Demaine, J. S. Mitchell, S. Sethia, and S. S. Skiena, "When can you fold a map?," *Computational Geometry: Theory and Applications*, vol. 29, pp. 23–46, sep 2004.

[18] W. Wu and Z. You, "A solution for folding rigid tall shopping bags," in *Proceedings of the Royal Society A: Mathematical, Physical and Engineering Sciences*, vol. 467, pp. 2561–2574, sep 2011.

[19] Z. Lin, L. S. Novelino, H. Wei, N. A. Alderete, G. H. Paulino, H. D. Espinosa, and S. Krishnaswamy, "Folding at the Microscale: Enabling Multifunctional 3D Origami-Architected Metamaterials," *Small*, vol. 16, p. 2002229, sep 2020.

[20] K. Liu and G. H. Paulino, "Nonlinear mechanics of non-rigid origami: An efficient computational approach," *Proceedings of the Royal Society A: Mathematical, Physical and Engineering Sciences*, vol. 473, oct 2017.

[21] S. Waitukaitis, P. Dieleman, and M. Van Hecke, "Non-Euclidean origami," *Physical Review E*, vol. 102, sep 2020.

[22] S. R. Woodruff and E. T. Filipov, "A bar and hinge model formulation for structural analysis of curved-crease origami," *International Journal of Solids and Structures*, vol. 204-205, pp. 114–127, nov 2020.

[23] V. Brunck, F. Lechenault, A. Reid, and M. Adda-Bedia, "Elastic theory of origami-based metamaterials," *Physical Review E*, vol. 93, no. 3, 2016.

[24] L. H. Dudte, E. Vouga, T. Tachi, and L. Mahadevan, "Programming curvature using origamiătessellations," *Nature Materials*, vol. 15, pp. 583–588, may 2016.

[25] B. H. Hanna, J. M. Lund, R. J. Lang, S. P. Magleby, and L. L. Howell, "Waterbomb base: A symmetric single-vertex bistable origami mechanism," *Smart Materials and Structures*, vol. 23, p. 094009, sep 2014.

[26] J. L. Silverberg, J. H. Na, A. A. Evans, B. Liu, T. C. Hull, C. D. Santangelo, R. J. Lang, R. C. Hayward, and I. Cohen, "Origami structures with a critical transition to bistability arising from hidden degrees of freedom," *Nature Materials*, vol. 14, no. 4, pp. 389–393, 2015.

[27] B. Liu, J. Silverberg, A. Evans, C. Santangelo, R. Lang, T. Hull, and I. Cohen, "Topological kinematics of origami metamaterials," *Nature Physics*, vol. 14, 08 2018.

[28] F. Lechenault and M. Adda-Bedia, "Generic Bistability in Creased Conical Surfaces," *Physical Review Letters*, vol. 115, p. 235501, dec 2015.

[29] E. T. Filipov and M. Redoutey, "Mechanical characteristics of the bistable origami hypar," *Extreme Mechanics Letters*, vol. 25, pp. 16–26, nov 2018.

[30] B. G. G. Chen and C. D. Santangelo, "Branches of Triangulated Origami Near the Unfolded State," *Physical Review X*, vol. 8, jun 2018.

[31] K. Kasahara and T. Takahama, *Origami for the Connoisseur*. Japan Pubns, 1998.

[32] T. Kawasaki, "On the relation between mountain-creases and valley-creases of a flat origami," in *Proceedings of the First International Meeting of Origami Science and Technology, 1991*, 1991.

[33] L. Zimmermann, K. Shea, and T. Stanković, "Conditions for Rigid and Flat Foldability of Degree-n Vertices in Origami," *Journal of Mechanisms and Robotics*, vol. 12, feb 2020.

[34] H. Akitaya, E. D. Demaine, T. Horiyama, T. C. Hull, J. S. Ku, and T. Tachi, "Rigid Foldability is NP-Hard," *Journal of Computational Geometry*, vol. 11, pp. 93–124, dec 2018.

[35] H. Feng, R. Peng, S. Zang, J. Ma, and Y. Chen, "Rigid foldability and mountain-valley crease assignments of square-twist origami pattern," *Mechanism and Machine Theory*, vol. 152, p. 103947, oct 2020.

[36] S. J. Callens and A. A. Zadpoor, "From flat sheets to curved geometries: Origami and kirigami approaches," *Materials Today*, vol. 21, no. 3, pp. 241–264, 2018.

[37] A. Gray, E. Abbena, and S. Salamon, *Modern Differential Geometry of Curves and Surfaces with Mathematica, Third Edition (Studies in Advanced Mathematics)*. Chapman and Hall/CRC, 2006.

[38] T. Tachi, "Freeform Rigid-Foldable Structure using Bidirectionally Flat-Foldable Planar Quadrilateral Mesh," in *Advances in Architectural Geometry 2010*, pp. 87–102, Springer Vienna, 2010.

[39] T. Tachi, "3D Origami Design Based on Tucking Molecules," in *Origami 4*, pp. 271–284, A K Peters/CRC Press, apr 2011.

[40] T. Tachi, "Origamizing polyhedral surfaces," *IEEE Transactions on Visualization and Computer Graphics*, vol. 16, pp. 298–311, mar 2010.

[41] M. Schenk and S. D. Guest, "Geometry of Miura-folded metamaterials," *Proceedings of the National Academy of Sciences of the United States of America*, vol. 110, pp. 3276–3281, feb 2013.

[42] P. Dieleman, N. Vasmel, S. Waitukaitis, and M. van Hecke, "Jigsaw puzzle design of pluripotent origami," *Nature Physics*, vol. 16, no. 1, pp. 63–68, 2020.

[43] J. E. Koehler, "Folding a strip of stamps," *Journal of Combinatorial Theory*, vol. 5, pp. 135–152, sep 1968.

[44] Z. Y. Wei, Z. V. Guo, L. Dudte, H. Y. Liang, and L. Mahadevan, "Geometric mechanics of periodic pleated origami," *Physical Review Letters*, vol. 110, p. 215501, may 2013.

[45] K. Miura, "Method of packaging and deployment of large membranes in space," *The Institute of Space and Astronautical Science Report*, vol. 618, p. 1, 1985.

[46] M. Stern, M. B. Pinson, and A. Murugan, "The complexity of folding self-folding origami," *Physical Review X*, vol. 7, p. 041070, dec 2017.

[47] M. B. Pinson, M. Stern, A. Carruthers Ferrero, T. A. Witten, E. Chen, and A. Murugan, "Self-folding origami at any energy scale," *Nature Communications*, vol. 8, p. 15477, aug 2017.

[48] T. Tachi and T. C. Hull, "Self-Foldability of Rigid Origami," *Journal of Mechanisms and Robotics*, vol. 9, 03 2017. 021008.

[49] C. D. Santangelo, "Extreme Mechanics: Self-Folding Origami," *Annual Review of Condensed Matter Physics*, vol. 8, pp. 165–183, mar 2017.

[50] J. L. Silverberg, A. A. Evans, L. McLeod, R. C. Hayward, T. Hull, C. D. Santangelo, and I. Cohen, "Using origami design principles to fold reprogrammable mechanical metamaterials," *Science*, vol. 345, pp. 647–650, aug 2014.

[51] S. Waitukaitis, R. Menaut, B. G. G. Chen, and M. Van Hecke, "Origami multistability: From single vertices to metasheets," *Physical Review Letters*, vol. 114, p. 055503, feb 2015.

[52] A. Iniguez-Rabago, Y. Li, and J. T. Overvelde, "Exploring multistability in prismatic metamaterials through local actuation," *Nature Communications*, vol. 10, no. 1, pp. 1–10, 2019.

[53] X. Zhou, S. Zang, and Z. You, "Origami mechanical metamaterials based on the Miura-derivative fold patterns," *Proceedings of the Royal Society A: Mathematical, Physical and Engineering Sciences*, vol. 472, p. 20160361, jul 2016.

[54] J. T. Overvelde, J. C. Weaver, C. Hoberman, and K. Bertoldi, "Rational design of reconfigurable prismatic architected materials," *Nature*, vol. 541, pp. 347–352, jan 2017.

[55] J. T. Overvelde, T. A. De Jong, Y. Shevchenko, S. A. Becerra, G. M. Whitesides, J. C. Weaver, C. Hoberman, and K. Bertoldi, "A three-dimensional actuated origami-inspired transformable metamaterial with multiple degrees of freedom," *Nature Communications*, vol. 7, p. 10929, mar 2016.

[56] E. T. Filipov, T. Tachi, and G. H. Paulino, "Origami tubes assembled into stiff, yet reconfigurable structures and metamaterials," *Proceedings of the National Academy of Sciences*, vol. 112, pp. 12321–12326, oct 2015.

[57] E. T. Filipov, G. H. Paulino, and T. Tachi, "Deployable Sandwich Surfaces with High Out-of-Plane Stiffness," *Journal of Structural Engineering*, vol. 145, p. 04018244, feb 2019.

[58] S. Kamrava, D. Mousanezhad, H. Ebrahimi, R. Ghosh, and A. Vaziri, "Origami-based cellular metamaterial with auxetic, bistable, and self-locking properties," *Scientific Reports*, vol. 7, p. 46046, apr 2017.

[59] J. Zhang, D. Karagiozova, Z. You, Y. Chen, and G. Lu, "Quasi-static large deformation compressive behaviour of origami-based metamaterials," *International Journal of Mechanical Sciences*, vol. 153-154, pp. 194–207, apr 2019.

[60] Z. Wang, L. Jing, K. Yao, Y. Yang, B. Zheng, C. M. Soukoulis, H. Chen, and Y. Liu, "Origami-Based Reconfigurable Metamaterials for Tunable Chirality," *Advanced Materials*, vol. 29, p. 1700412, jul 2017.

[61] Y. Yang and Z. You, "Geometry of transformable metamaterials inspired by modular origami," *Journal of Mechanisms and Robotics*, vol. 10, no. 2, 2018.

[62] Y. Yang and Z. You, "A Modular Origami-inspired Mechanical Metamaterial," *Origami*, vol. 7, p. 995, 2018.

[63] J. T. B. Overvelde and K. Bertoldi, "Relating pore shape to the non-linear response of periodic elastomeric structures," *Journal of the Mechanics and Physics of Solids*, vol. 64, pp. 351–366, mar 2014.

[64] Z. Zhai, Y. Wang, and H. Jiang, "Origami-inspired, on-demand deployable and collapsible mechanical metamaterials with tunable stiffness," *Proceedings of the National Academy of Sciences of the United States of America*, vol. 115, no. 9, pp. 2032–2037, 2018.

[65] H. Feng, J. Ma, Y. Chen, and Z. You, "Twist of Tubular Mechanical Metamaterials Based on Waterbomb Origami," *Scientific Reports*, vol. 8, pp. 1–13, dec 2018.

[66] A. L. Wickeler and H. E. Naguib, "Novel origami-inspired metamaterials: Design, mechanical testing and finite element modelling," *Materials and Design*, vol. 186, p. 108242, jan 2020.

[67] C. Coulais, D. Sounas, and A. Alù, "Static non-reciprocity in mechanical metamaterials," *Nature*, vol. 542, pp. 461–464, feb 2017.

[68] E. Shamonina and L. Solymar, "Metamaterials: How the subject started," *Metamaterials*, vol. 1, no. 1, pp. 12–18, 2007.

[69] K. Bertoldi, V. Vitelli, J. Christensen, and M. Van Hecke, "Flexible mechanical metamaterials," *Nature Reviews Materials*, vol. 2, no. 17066, pp. 1–11, 2017.

[70] T. Bückmann, M. Kadic, R. Schittny, and M. Wegener, "Mechanical cloak design by direct lattice transformation," *Proceedings of the National Academy of Sciences*, vol. 112, pp. 4930–4934, apr 2015.

[71] K. Liu, T. Tachi, and G. H. Paulino, "Invariant and smooth limit of discrete geometry folded from bistable origami leading to multistable metasurfaces," *Nature Communications*, vol. 10, pp. 1–10, dec 2019.

[72] C. Coulais, C. Kettenis, and M. Van Hecke, "A characteristic length scale causes anomalous size effects and boundary programmability in mechanical metamaterials," *Nature Physics*, vol. 14, pp. 40–44, sep 2018.

[73] P. S. Sreetharan, J. P. Whitney, M. D. Strauss, and R. J. Wood, "Monolithic fabrication of millimeter-scale machines," *Journal of Micromechanics and Microengineering*, vol. 22, p. 055027, may 2012.

[74] J. Qu, M. Kadic, A. Naber, and M. Wegener, "Micro-Structured Two-Component 3D Metamaterials with Negative Thermal-Expansion Coefficient from Positive Constituents," *Scientific Reports*, vol. 7, pp. 1–8, jan 2017.

[75] T. Frenzel, M. Kadic, and M. Wegener, "Three-dimensional mechanical metamaterials with a twist," *Science*, vol. 358, pp. 1072–1074, nov 2017.

[76] J. R. Greer and V. S. Deshpande, "Three-dimensional architected materials and structures: Design, fabrication, and mechanical behavior," *MRS Bulletin*, vol. 44, pp. 750–757, oct 2019.

[77] S. Waitukaitis and M. Van Hecke, "Origami building blocks: Generic and special four-vertices," *Physical Review E*, vol. 93, p. 023003, feb 2016.

[78] M. Schenk and S. D. Guest, "Origami folding: A structural engineering approach," in *Origami 5: Fifth International Meeting of Origami Science, Mathematics, and Education*, pp. 291–303, A K Peters/CRC Press, 2016.

[79] K. Liu, L. S. Novelino, P. Gardoni, and G. H. Paulino, "Big influence of small random imperfections in origami-based metamaterials: Influence of Imperfections in Origami," *Proceedings of the Royal Society A: Mathematical, Physical and Engineering Sciences*, vol. 476, p. 20200236, sep 2020.

[80] X. Ning, X. Wang, Y. Zhang, X. Yu, D. Choi, N. Zheng, D. S. Kim, Y. Huang, Y. Zhang, and J. A. Rogers, "Assembly of advanced materials into 3d functional structures by methods inspired by origami and kirigami: A review," *Advanced Materials Interfaces*, vol. 5, no. 13, p. 1800284, 2018.

[81] A. Pagano, B. Leung, B. Chien, T. Yan, A. Wissa, and S. Tawfick, "Multi-stable origami structure for crawling locomotion," in *ASME Conference on Smart Materials, Adaptive Structures and Intelligent Systems*, p. V002T06A005, ASME, sep 2016.

[82] T. Tachi and T. C. Hull, "Self-foldability of rigid origami," *Journal of Mechanisms and Robotics*, vol. 9, apr 2017.

[83] E. Baranger, P. A. Guidault, and C. Cluzel, "Numerical modeling of the geometrical defects of an origami-like sandwich core," *Composite Structures*, vol. 93, pp. 2504–2510, sep 2011.

[84] C. Jianguo, D. Xiaowei, Z. Yuting, F. Jian, and Z. Ya, "Folding behavior of a foldable prismatic mast with Kresling origami pattern," *Journal of Mechanisms and Robotics*, vol. 8, jun 2016.

[85] B. Wang and C. Zhou, "The imperfection-sensitivity of origami crash boxes," *International Journal of Mechanical Sciences*, vol. 121, pp. 58–66, feb 2017.

[86] Y. Hu and H. Liang, "Folding simulation of rigid origami with Lagrange multiplier method," *International Journal of Solids and Structures*, vol. 202, pp. 552–561, oct 2020.

[87] G. Oliveri and J. T. Overvelde, "Inverse design of mechanical metamaterials that undergo buckling," *Advanced Functional Materials*, vol. 30, no. 12, p. 1909033, 2020.

[88] L. Novotny, "Strong coupling, energy splitting, and level crossings: A classical perspective," *American Journal of Physics*, vol. 78, no. 11, pp. 1199–1202, 2010.

[89] S. Satpathy, A. Roy, and A. Mohapatra, "Fano interference in classical oscillators," *European Journal of Physics*, vol. 33, pp. 863–871, may 2012.

[90] X. Yu, H. Fang, F. Cui, L. Cheng, and Z. Lu, "Origami-inspired foldable sound barrier designs," *Journal of Sound and Vibration*, vol. 442, pp. 514–526, mar 2019.

[91] C. Xu, B. M. Gallant, P. U. Wunderlich, T. Lohmann, and J. R. Greer, "Three-Dimensional Au Microlattices as Positive Electrodes for Li-O2 Batteries," *ACS Nano*, vol. 9, pp. 5876–5883, jun 2015.

[92] H. Yasuda and J. Yang, "Reentrant origami-based metamaterials with negative Poisson's ratio and bistability," *Physical Review Letters*, vol. 114, p. 185502, may 2015.

[93] J. T. B. Overvelde, S. Shan, and K. Bertoldi, "Compaction through buckling in 2D periodic, soft and porous structures: Effect of pore shape," *Advanced Materials*, vol. 24, pp. 2337–2342, may 2012.

[94] B. Florijn, C. Coulais, M. Van Hecke, F. B, C. C, van Hecke M, B. Florijn, C. Coulais, M. Van Hecke, F. B, C. C, van Hecke M, B. Florijn, C. Coulais, and M. Van Hecke, "Programmable mechanical metamaterials," *Physical Review Letters*, vol. 113, p. 175503, oct 2014.

[95] D. Yang, L. Jin, R. V. Martinez, K. Bertoldi, G. M. Whitesides, and Z. Suo, "Phase-transforming and switchable metamaterials," *Extreme Mechanics Letters*, vol. 6, pp. 1–9, mar 2016.

[96] S. H. Kang, S. Shan, W. L. Noorduin, M. Khan, J. Aizenberg, and K. Bertoldi, "Buckling-induced reversible symmetry breaking and amplification of chirality using supported cellular structures," *Advanced Materials*, vol. 25, pp. 3380–3385, jun 2013.

[97] H. Fang, K. W. Wang, and S. Li, "Asymmetric energy barrier and mechanical diode effect from folding multi-stable stacked-origami," *Extreme Mechanics Letters*, vol. 17, pp. 7–15, nov 2017.

[98] A. Rafsanjani and D. Pasini, "Bistable auxetic mechanical metamaterials inspired by ancient geometric motifs," *Extreme Mechanics Letters*, vol. 9, pp. 291–296, 2016.

[99] S. Shan, S. H. Kang, J. R. Raney, P. Wang, L. Fang, F. Candido, J. A. Lewis, and K. Bertoldi, "Multistable Architected Materials for Trapping Elastic Strain Energy," *Advanced Materials*, vol. 27, pp. 4296–4301, aug 2015.

[100] B. Haghpanah, L. Salari-Sharif, P. Pourrajab, J. Hopkins, L. Valdevit, B. Haghpanah, L. Salari-Sharif, P. Pourrajab, L. Valdevit, and J. Hopkins, "Multistable Shape-Reconfi gurable Architected Materials," *Advanced Materials*, vol. 28, pp. 7915–7920, sep 2016.

[101] S. Li, H. Fang, and K. W. Wang, "Recoverable and programmable collapse from folding pressurized origami cellular solids," *Phys. Rev. Lett.*, vol. 117, p. 114301, Sep 2016.

[102] K. Saito, A. Tsukahara, and Y. Okabe, "New Deployable Structures Based on an Elastic Origami Model," *Journal of Mechanical Design*, vol. 137, p. 021402, feb 2015.

[103] S. Daynes, R. S. Trask, and P. M. Weaver, "Bio-inspired structural bistability employing elastomeric origami for morphing applications," *Smart Materials and Structures*, vol. 23, p. 125011, dec 2014.

[104] B. Grünbaum, "Uniform tilings of 3-space," *Geombinatorics*, vol. 4, no. 2, pp. 49–56, 1994.

[105] T. Tachi, "Simulation of rigid origami," *Origami*, vol. 4, pp. 175–187, 2009.

[106] S. Even and G. Even, *Graph Algorithms, second edition*, vol. 9780521517. Cambridge: Cambridge University Press, 2011.

[107] X. Shang, L. Liu, A. Rafsanjani, and D. Pasini, "Durable bistable auxetics made of rigid solids," *Journal of Materials Research*, vol. 33, no. 3, p. 300308, 2018.

[108] A. Vyatskikh, S. Delalande, A. Kudo, X. Zhang, C. M. Portela, and J. R. Greer, "Additive manufacturing of 3D nano-architected metals," *Nature Communications*, vol. 9, p. 593, dec 2018.

[109] C. Ling, A. Cernicchi, M. D. Gilchrist, and P. Cardiff, "Mechanical behaviour of additively-manufactured polymeric octet-truss lattice structures under quasi-static and dynamic compressive loading," *Materials & Design*, vol. 162, pp. 106–118, jan 2019.

[110] S. Li, H. Fang, S. Sadeghi, P. Bhovad, and K. W. Wang, "Architected Origami Materials: How Folding Creates Sophisticated Mechanical Properties," *Advanced Materials*, vol. 31, p. 1805282, feb 2019.

[111] L. J. F. Sujan and D., "Origami Theory and Its Applications: A Literature Review," *World Academy of Science, Engineering and Technology*, vol. 7, pp. 229–233, sep 2013.

[112] M. Johnson, Y. Chen, S. Hovet, S. Xu, B. Wood, H. Ren, J. Tokuda, and Z. T. H. Tse, "Fabricating biomedical origami: a state-of-the-art review," nov 2017.

[113] K. Kuribayashi, K. Tsuchiya, Z. You, D. Tomus, M. Umemoto, T. Ito, and M. Sasaki, "Self-deployable origami stent grafts as a biomedical application of Ni-rich TiNi shape memory alloy foil," *Materials Science and Engineering A*, vol. 419, pp. 131–137, mar 2006.

[114] Y. Liu, J. Park, R. J. Lang, A. Emami-Neyestanak, S. Pellegrino, M. S. Humayun, and Y. C. Tai, "Parylene origami structure for introcular implantation," in *2013 Transducers and Eurosensors XXVII: The 17th International Conference on Solid-State Sensors, Actuators and Microsystems, TRANSDUCERS and EUROSENSORS 2013*, pp. 1549–1552, IEEE, jun 2013.

[115] J. T. Bruton, T. G. Nelson, T. K. Zimmerman, J. D. Fernelius, S. P. Magleby, and L. L. Howell, "Packing and deploying Soft Origami to and from cylindrical volumes with application to automotive airbags," *Royal Society Open Science*, vol. 3, no. 9, 2016.

[116] Z. Abel, J. Cantarella, E. D. Demaine, D. Eppstein, T. C. Hull, J. S. Ku, R. J. Lang, and T. Tachi, "Rigid Origami Vertices: Conditions and Forcing Sets," *JoCG*, vol. 7, pp. 171–184, jul 2015.

[117] T. C. Hull, "The combinatorics of flat folds: A survey," in *Origami*, pp. 29–38, AK Peters, jul 2002.

[118] *Integrated Origami-String System*, vol. Volume 5B: 43rd Mechanisms and Robotics Conference of *International Design Engineering Technical Conferences and Computers and Information in Engineering Conference*, 08 2019. V05BT07A033.

[119] A. Kelly and K. M. Knowles, *Crystallography and Crystal Defects: Second Edition*. Chichester, UK: John Wiley & Sons, Ltd, jan 2012.

[120] K. Bertoldi, M. C. Boyce, S. Deschanel, S. M. Prange, and T. Mullin, "Mechanics of deformation-triggered pattern transformations and superelastic behavior in periodic elastomeric structures," *Journal of the Mechanics and Physics of Solids*, vol. 56, no. 8, pp. 2642–2668, 2008.

[121] J. Ou, M. Skouras, N. Vlavianos, F. Heibeck, C. Y. Cheng, J. Peters, and H. Ishii, "AeroMorph - Heat-sealing inflatable shape-change materials for interaction design," *UIST 2016 - Proceedings of the 29th Annual Symposium on User Interface Software and Technology*, pp. 121–132, 2016.

[122] Z. L. Wu, M. Moshe, J. Greener, H. Therien-Aubin, Z. Nie, E. Sharon, and E. Kumacheva, "Three-dimensional shape transformations of hydrogel sheets induced by small-scale modulation of internal stresses.," *Nature communications*, vol. 4, p. 1586, 2013.

[123] J. H. Na, A. A. Evans, J. Bae, M. C. Chiappelli, C. D. Santangelo, R. J. Lang, T. C. Hull, and R. C. Hayward, "Programming reversibly self-folding origami with micropatterned photo-crosslinkable polymer trilayers," *Advanced Materials*, vol. 27, pp. 79–85, oct 2015.

[124] M. F. Reynolds, K. L. McGill, M. A. Wang, H. Gao, F. Mujid, K. Kang, J. Park, M. Z. Miskin, I. Cohen, and P. L. McEuen, "Capillary Origami with Atomically Thin Membranes," *Nano Letters*, vol. 19, pp. 6221–6226, sep 2019.

[125] M. Z. Miskin, K. J. Dorsey, B. Bircan, Y. Han, D. A. Muller, P. L. McEuen, and I. Cohen, "Graphene-based bimorphs for micron-sized, tautonomous origami machines," *Proceedings of the National Academy of Sciences of the United States of America*, vol. 115, pp. 466–470, jan 2018.

[126] J. G. Kim, J. E. Park, S. Won, J. Jeon, and J. J. Wie, "Contactless manipulation of soft robots," *Materials*, vol. 12, no. 19, 2019.

[127] D. Müllner, "Modern hierarchical, agglomerative clustering algorithms," *CoRR*, sep 2011.

[128] M. Ester, H.-P. Kriegel, J. Sander, and X. Xu, "A Density-Based Algorithm for Discovering Clusters in Large Spatial Databases with Noise," in *Proceedings of the 2nd International Conference on Knowledge Discovery and Data Mining*, pp. 226–231, 1996.

[129] W. Callister and D. Rethwisch, *Materials Science and Engineering*. Wiley, 2014.

Summary

Origami is known as a technique that is used to transform a flat sheet of paper into any shape by folding it repeatedly. Originally it was used in Japan as religious decorations, and in Germany as a tool to develop consciousness of forms and figures in children. Recently, it has gained popularity in many fields such as in architecture to build responsive facades and in engineering as inspiration to create a microsurgery system.

Traditionally, scientists have described origami using a rigid model. In this model, origami deforms only at the hinges, whereas the faces are completely rigid. Due to its simplicity this model has been widely used by scientists. Nonetheless, this model has some limitations, since it assumes that deformations take place only at the hinges, which is not always met in real life. Currently, scientists study origami using an elastic model. Elastic origami allows for the deformation of not only the hinges but also the faces. As a result, it allows new behaviors that are not possible with the rigid model, since the origami pattern can undergo additional deformations through new folding pathways. These new behaviors are important since they can be used in new generations of origami-inspired structures and devices.

However, the flexibility of elastic origami comes at a cost. Since origami behavior cannot longer be described by just the hinges, but also by the deformation of the faces, it is nearly impossible to describe it analytically. This results in three problems that I will address in this thesis. First, the additional deformation of the faces adds many parameters to the origami model that complicates the full scan of the origami behavior. *Is it possible to simplify the model in order to study complex origami designs based on real life experiments?* Second, the folding behavior of elastic origami is highly non-linear, making it difficult to map all the possible folding behaviors. *Can we find a way to systematically characterize the deformation space in the elastic origami model?* Third, any force gets dissipated by the elasticity preventing global uniform deformation. *How can we obtain well-defined folding behavior in the elastic origami model?*

I use origami-inspired metamaterials as case studies to resolve these questions. By taking origami designs as building blocks, they can be tessellated to fill space in order to build so-called mechanical metamaterials, i.e., materials that get their properties from their internal structure rather than their chemistry. These metamaterials can be made to exhibit internal mechanism that alter shape and with that functionality. Nevertheless, the same approach can be used for any other origami pattern. These solutions shed light on the complex behavior of origami and gives specific guidelines to control it.

In order to address the problems of elastic origami, in this thesis, together with my collaborators, I first introduce an elastic origami model based on a bar-and-hinge model. We use this model to explore the folding behavior of origami metamaterials. In chapter 2 we describe the elastic energy of the elastic origami model that derives from three types of deformations, hinge bending, face stretching and face bending. We also present the

constraints that ensure that the structure behaves as close as possible to real life, such as maximum face strain and adjacent self-contact.

In chapter 3, we use 3D prismatic building blocks based on polyhedra to study the kinematics of elastic origami in order to find new deformation pathways. Based on the linearized elastic and kinetic energy, we are able to obtain and separate the normal modes of the structures that define the folding direction of the origami structure. We notice the appearance of so-called soft and pseudo soft modes that resemble the branches of the rigid origami model defined by a minimum face deformation. Then, we constrain the elastic origami model to obtain a classification of the normal modes that spans through all stiffness regimes and show that constraining face bending simplifies the model still capturing the folding behavior of the origami structures. As a result, by removing the face bending energy, we simplify the model and define a single parameter that allows us to move between rigid and elastic origami.

In chapter 4, we apply an energy minimization method to search new deformation states of the 3D prismatic origami metamaterials in a fully nonlinear framework. By using local actuation to deform the materials we are able to explore and visualize their complex mechanical behavior showing the existence of multistability. This multistability arises from the unit cell's geometry. Surprisingly, we find that some of these materials have over 400 mechanically stable configurations. These prismatic materials could lead to the next generation of multifunctional metamaterials that can be applied as e.g., reconfigurable acoustic wave guides, microelectronic mechanical systems, and energy storage devices.

Last, in chapter 5, we study the folding behavior of non-linear origami sheets to obtain the limitations on the deformation of elastic origami. Typically, non-linearity arises from the geometry of the origami pattern, but here we use a simple 2D design called a 4-vertex, where we implement the non-linearity with bistable hinges. By performing small perturbation on the structures and then minimizing their energy, we observe that these metamaterials undergo a transition from rigid origami to elastic origami when varying the non-linear stiffness. Furthermore, by drawing a similitude to atomic crystals, we find an additional transition from elastic origami to amorphous material, fundamentally changing the way the structure behaves. This shines light into a characteristic length that affects the area of influence of a given force and helps to define actuation strategies to ensure well-defined folding behavior of these origami materials.

About the author

The author of this thesis was born on May 08, 1990, in Mexico City, Mexico. He completed compulsory education in a Swiss school in Mexico. During this period, he developed his interest on science and research while acquiring an international and open mind. He then enrolled in the Iberoamerican University, Mexico, to study his bachelors in physics engineering. During his bachelor, his interests in nanotechnology and quantum physics led him to the Nanoscience and Nanotechnology Laboratory, where he worked for 3.5 years. This work opened the door to two international internships, one in the University of Manchester, UK, and the other in the Pennsylvania State University, USA. These internships were important experiences for him since he got to know how research is done at bigger universities, collaborated with people of different cultures and learnt how to be independent.

After he graduated with honors from his bachelors degree, he started a new adventure. He received a full scholarship to study a masters degree in applied physics at the Delft University of Technology, the Netherlands. This was a big step for him since he had to leave his family and friends in Mexico to pursue his dreams. Based on his interests and future plans, he followed the Quantum Nanoscience track together with the Casimir pre-PhD program. After he finished all the classes, he worked on his thesis in the Experimental Physics department on optomechanical detection of superconducting nanowires. During this period, he spent most of his time in the cleanroom fabricating the nanowires. Even though he enjoyed learning the peculiarities and technicalities of the nanofabrication and quantum world, he understood that collaborations between different fields result in a fruitful research. So, he started to look for something different to do for his internship. In a conference, he was introduced to world of mechanical metamaterials that immediately ignited his interest. His internship was on developing a recipe to make hydrogels for metamaterials at AMOLF, the Netherlands, where, little did he know, he spent the next 4 years of his life.

After a break of six months in Mexico, he returned to the Netherlands to start his PhD under the supervision of Dr.ir. Bas Overvelde. Four years thereafter, the author presents this thesis as the culmination of his PhD. This thesis is not only the research done at AMOLF or the many conferences where the author presented his work, but also the effort, frustration and enjoyment of being a scientist. For now, he will leave academia in the search for new adventures and looks forward to whatever life brings to him.

List of Publications

- McClintock*, H.D., Doshi*, N., **Iniguez-Rabago*, A.**, Weaver, J.C., Jayaram, K., Wood, R.J., Overvelde, J.T.B., *A fabrication strategy for re-configurable materials at the millimeter-scale*. Adv. Funct. Mater. (* contributed equally) (In Press)
(Introduction)

- **Iniguez-Rabago, A.**, Li, Y. and Overvelde, J.T.B., *Exploring multistability in prismatic metamaterials through local actuation*. Nat. Commun. 10, 5577 (2019).
(Chapter 2 and 4)

- **Iniguez-Rabago, A.**, and Overvelde, J.T.B., *Elastic folding behavior of prismatic structures*. (In preparation)
(Chapter 3)

- **Iniguez-Rabago, A.**, Overvelde, J.T.B., *From rigid to amorphous folding behavior in origami-inspired metamaterials with bistable hinges*. PRL. (In review)
(Chapter 5)

Acknowledgements

You have in your hands the tears and sweat of 4 years of my life. This journey has not been easy, but in the end, I look back and appreciate the work that I have done. Of course, this work would not have been possible without the support of the people around me. This section is for you!

Before everything, I want to thank my supervisor Dr.ir. Johannes T.B. Overvelde aka Bas. You believed in me since the beginning. We had a good connection and worked very good together. You taught me a lot in these last four years, not only about science and metamaterials, but also about life. Your enthusiasm over science and your critical point of view full of new ideas to research fueled my research forward. Thank you!

I also want to thank Dr. Giorgio Oliveri. Mbare, everything started on the first day I met you. You were interviewing me for the PhD position, but instead of asking me questions, you only told me: I cannot wait to have you here! We enjoyed so much, especially the conferences and the trips after or before them. You were a perfect colleague, giving support when it was needed and cheering up the achievements. For being the backbone of my PhD I want to thank you!

Next in turn is Luuk. Meneer van Laake, I admire you! I think it takes a strong courage to start a PhD as you did. I cannot understand how you make it look so easy! You started one year after me, but you already knew so much more than me. You were always there with new ideas, making sure all details are prefect and willing to help everyone. You indeed help me a lot. Thank you!

During this time, I supervised students. The goal of course is to teach them how to do science and think critically, but what they do not know is that the teacher also learns from them. Yun, you were my first student and because of you I started my PhD with the right foot. Sami, you started a new project and you achieved amazing results, giving me a big motivation to move forward. Charlie, our project did not go smooth due to external agents, but you taught me how to look for alternative research ideas and how to pronounce 'prisM'. Nastia, with you I learned how to communicate in a better way and search for that big research question. And Simon, you taught me not only about chemistry but also about being independent. All of you contributed to the development of my research and myself, so thank you!

I was lucky to do my PhD in a supporting research group. SoRoMa, although I always opposed to the name, you were amazing! We had amazing outings, coffee breaks, group meetings and cakes. All past and present members have had a very good connection. This definitely helps the research and helped me a lot to discuss ideas. Thank you!

My research was not only me thinking about ideas. These ideas need to come alive, especially in experiments. Here, there are many people who helped me doing this. Niels, as the technician of the group, you helped me a lot in experimental set-ups and 3D printing. Your approach to solving problems amazes me! Hinco and Dion, both of you were always very helpful with different ways to solve problems and with that special technical

eye that made everything work. Jan and Tom, thank you for all the support for the laser cutting. Dimitri, Bob, Andries and Hans, without your guide in the cleanroom I would not have been able to make my ideas come true.

But not everything is about research. Many people have helped me throughout these years in many ways. Here I mention a few, but I am sure that there are many more that I cannot remember, so if we have crossed paths, thank you!

During these four years I was fortunate to stay in the same office and most of that time there was a constant officemate, Giada. You are a lovely person with a huge heart! I love your point of view on life, and I love that we share so many things. Thank you for all the support and for just being you!

Lukas, I met you before I started my PhD and you have always been a close friend. Your enthusiasm for helping others amazes me. I loved the dinners that we had together and your cooking abilities. I also enjoyed every party that you organized or that we went together. Thank you for the amazing moments together!

Being away from your native country is always hard, but fortunately, I found a little Mexico. Roberto and Said, you brought a part of Mexico with you and this always made me teleport myself back. Your comments, gossip and way of speaking made my PhD much more Mexican and I am grateful about it. Andrea, you are an amazing person, your cooking also made me travel back, thank you for nourish my stomach with Mexican delights.

There are many more people that have helped me in one way or another these last four years. Marloes, you are always happy and the way you approach life always turned me in a good mood. Lucie, your creativity and our conversations were very comforting. Jenny, you are a strong woman and your ambition to be at the beach at all times put myself always in a more relaxed mood. Nasim, your pursue of happiness and resilience made me feel strong. Ruslan, your dedication to research and to party made me see that you can have it all. Carolyn, you know what you want and you fight for it, I would like to be like you.

An important time in these last 4 years, was the time I did not spend doing research. Augusto, I know you for a long time and I will never forget our parties. Weiyi, you were my officemate and now you are a true friend. Luis, we lived together for a while and even though now we do not, you keep teaching me a lot. Antonio, once I said you were like a second brother to me, and I am happy you still are. Tomek and Oskar, our conversations and beer drinking are very refreshing and uplifting. There are many more, but these acknowledgements are getting long, so thank you all!

También quiero agradecerle a mi familia. Ustedes son el pilar más grande y sin su apoyo esto no se hubiera podido. A mis papás les agradezco el amor y soporte incondicional por todos estos años. A mi hermano y Daniela, sus consejos y apoyo que me han ayudado a sobrellevar mi estancia fuera de México. A mi tía Alicia, a todos mis tías, tíos, primas y primos, muchas gracias por todo!

Finally, the most important person, Bram. You have been the person who has seen me at the lowest and highest during these last years, and you were always there for me! I cannot put in words how much I appreciate all this support you have given me, so I will just say this: I love you!